

Monitoring and Forecasting Forest Drought Stress to a Changing Climate

by

Amanda M. Schwantes

University Program in Ecology  
Duke University

Date: \_\_\_\_\_

Approved:

\_\_\_\_\_  
Jennifer J. Swenson, Supervisor

\_\_\_\_\_  
Robert B. Jackson

\_\_\_\_\_  
Amilcare Porporato

\_\_\_\_\_  
James S. Clark

Dissertation submitted in partial fulfillment of  
the requirements for the degree of Doctor  
of Philosophy in the University Program in Ecology  
Duke University

2017

ABSTRACT

Monitoring and Forecasting Forest Drought Stress to a Changing Climate

by

Amanda M. Schwantes

University Program in Ecology  
Duke University

Date: \_\_\_\_\_

Approved:

\_\_\_\_\_  
Jennifer J. Swenson, Supervisor

\_\_\_\_\_  
Robert B. Jackson

\_\_\_\_\_  
Amilcare Porporato

\_\_\_\_\_  
James S. Clark

An abstract of a dissertation submitted in partial  
fulfillment of the requirements for the degree  
of Doctor of Philosophy in the University Program in Ecology  
Duke University

2017

Copyright by  
Amanda M. Schwantes  
2017

## **Abstract**

Globally, trees are increasingly dying from extreme droughts and heatwaves, a trend that is expected to increase with climate change. Loss of trees has significant ecological, biophysical, and biogeochemical consequences. In this thesis, I explored how forests will respond to increases in droughts and heatwaves projected under climate change, by studying the impacts of the 2011 drought on the forests and woodlands of Texas. I first developed new methods using remote sensing that improved monitoring of forest disturbances from droughts and heatwaves at regional scales. I then explored multiple modeling approaches, to improve forecasts of forest vulnerability to future droughts and heatwaves.

Drought-induced tree mortality is unique because it often is limited to only subtle and diffuse changes in forest cover. Therefore, I first developed a new approach towards quantifying drought-driven canopy loss in open canopy woodland systems using remotely sensed imagery, across a Landsat scene in central Texas (>30,000 km<sup>2</sup>). I used classifications of 1-m orthophotos to calibrate and validate 30-m Landsat imagery. In scaling up to create regional canopy loss maps, I assembled a Landsat time-series and separated mortality pixels experiencing persistent canopy loss from pixels with only background noise by applying the Landtrendr algorithm. I then estimated percent tree canopy loss within each of these mortality pixels by comparing two models capable of

handling zero-inflated continuous proportions: random forest and a zero-or-one inflated beta (ZOIB) regression model. I found that the ZOIB regression model had the highest accuracy in predicting canopy loss (mean absolute error = 5.16%, root mean square error = 8.01%).

Again using remotely sensed imagery, I developed a second method to quantify canopy loss due to the 2011 drought across the many diverse systems of Texas, from the eastern pine/hardwood forests to the western shrublands. I then used these maps to better understand which ecological systems were most impacted and climatic trends that could explain spatial patterns of canopy loss. Canopy loss observations in ~200 multi-temporal fine-scale orthophotos (1-m) were used to train coarser Landsat imagery (30-m) to create 30-m binary statewide canopy loss maps. I found that canopy loss occurred across all major ecoregions of Texas, with an average loss of 9.5%. The drought had the highest impact in post-oak woodlands, pinyon-juniper shrublands, and Ashe juniper woodlands. Focusing on a 100-km by ~1000-km transect spanning the State's 5-fold east-west precipitation gradient (~1500 to ~300 mm), I compared spatially explicit 2011 climatic anomalies to our canopy loss maps. Much of the canopy loss occurred in areas that passed specific climatic thresholds: warm season anomalies in mean temperature (+1.6 °C) and vapor pressure deficit (VPD, +0.66 kPa), annual percent deviation in precipitation (-38%), and 2011 difference between precipitation and potential evapotranspiration (-1206 mm). Although similarly low precipitation occurred during

the landmark 1950s drought, the VPD and temperature anomalies observed in 2011 were even greater. Furthermore, future climate data under the representative concentration pathway 8.5 trajectory project that average values will surpass the 2011 VPD anomaly during the 2070-2099 period and the temperature anomaly during the 2040-2099 period. Identifying vulnerable ecological systems to drought stress and climate thresholds associated with canopy loss will aid in predicting how forests will respond to a changing climate and how ecological landscapes will change in the near term.

As climate change continues, forest vulnerability to droughts and heatwaves is increasing, but vulnerability varies regionally and locally through landscape position. However, most models used in forecasting forest responses to heat and drought do not incorporate relevant spatial processes. Therefore, thirdly, to improve spatial predictions of tree vulnerability, I employed a non-linear stochastic model of soil moisture dynamics accounting for landscape differences in aspect, topography, and soils. Across a watershed in central Texas I modeled dynamic water stress for a dominant tree species, *Juniperus ashei* and projected future dynamic water stress through the 21st century. Modeled dynamic water stress tracked spatial patterns of drought-impacted area derived using remote sensing. Accuracy in predicting drought-impacted stands increased from 60%, accounting for only soil variability, to 72% when also including lateral redistribution of water and radiation/temperature effects attributable to aspect. Our analysis also suggests dynamic water stress will increase through the 21st century,

with minimal buffering from the landscape. Favorable microsites/refugia may exist across a landscape where trees can persist; however, if future droughts are too severe, the buffering capacity of a heterogenous landscape could be overwhelmed.

Incorporating spatial data will improve projections of future tree water stress and identification of potential resilient refugia.

Lastly, droughts impact tree species unequally and therefore have the potential to alter the species composition of forests. As droughts intensify under climate change, models that can account for both changing environmental conditions as well as joint species-specific responses are needed to forecast shifts in species ranges, composition, abundance, and mortality. Therefore, lastly, I used a Generalized Joint Attribute Model, GJAM, to simultaneously model live and dead basal area by species, across Texas, using Forest Inventory and Analysis plots from 2001-2015 and covariates related to climate, topography and soils. I then projected shifts in species abundance into the 21st century under multiple climate warming scenarios. Model projections show that many of the eastern hardwood species will likely shift eastward throughout the 21st century. Many of the western woodland species are also projected to shift eastward and become increasingly dominant throughout Texas. By modeling species abundance and mortality simultaneously and by using covariates related to climate variability, we can improve projections of forest responses to continuing climate change.

# Contents

Abstract .....	iv
List of Tables .....	xii
List of Figures .....	xiv
Acknowledgements .....	xvii
1. Introduction .....	1
1.1 Why study drought-induced tree mortality? .....	1
1.2 Research objectives .....	5
1.3. Dissertation Outline .....	8
2. Quantifying Drought-Induced Tree Mortality in the Open Canopy Woodlands of Central Texas .....	10
2.1 Introduction .....	10
2.2 Study area .....	14
2.3 Methods .....	15
2.3.1. Creating fine-scale canopy loss maps .....	18
2.3.1.1 Classification of orthophotos .....	18
2.3.1.2 Accuracy assessment of fine-scale canopy loss maps with field surveys ..	19
2.3.2. Creating coarse-scale canopy loss maps: pre-processing steps .....	21
2.3.2.1 Pre-processing of Landsat imagery .....	21
2.3.2.2 Filtering canopy loss from no-change pixels: Landtrendr algorithm .....	22
2.3.2.3. Scaling up to create regional continuous canopy loss maps .....	23
2.3.3 Creating coarse-scale canopy loss maps: variable selection and modeling .....	24

2.3.3.1 Identifying explanatory variables: vegetation indices and auxiliary variables .....	25
2.3.3.2 Modeling approaches: RF vs ZOIB.....	30
2.3.3.3 Accuracy assessments of coarse-scale canopy loss maps.....	34
2.4 Results .....	35
2.4.1 Accuracy assessments of the fine-scale canopy loss maps .....	35
2.4.2. Comparison of accuracy among models .....	35
2.4.3 Canopy loss estimated across the study area .....	43
2.5 Discussion.....	44
3. Measuring canopy loss and climatic thresholds from an extreme drought along a 5-fold precipitation gradient across Texas.....	50
3.1 Introduction.....	50
3.2 Materials and Methods.....	55
3.2.1 Study area.....	55
3.2.2 Creating training and testing data: classification and field validation of 1-m canopy loss maps.....	58
3.2.3 Scaling up to regional estimates using random forests: 30-m binary canopy loss map .....	60
3.2.4. Defining relationships between spatial patterns of canopy loss and climate..	65
3.2.5 Projecting whether 2011 climate anomalies were likely to be crossed in the future.....	67
3.2.6 Identifying ecological systems most impacted by the 2011 drought .....	68
3.3 Results .....	68
3.4 Discussion.....	80

4. Accounting for landscape heterogeneity improves spatial predictions of tree vulnerability to drought.....	89
4.1 Introduction.....	89
4.2 Materials and Methods.....	94
4.2.1 Study area.....	94
4.2.2 Soil water balance model.....	95
4.2.3 Infiltration: rainfall, canopy interception, and lateral water flow .....	96
4.2.4 Losses: evapotranspiration and leakage .....	98
4.2.5 Static and dynamic water stress .....	102
4.2.6 Historical and future projections of water stress .....	103
4.2.7 Accuracy assessments.....	104
4.3 Results .....	106
4.3.1 Comparing modeled water stress to observations of drought-impacted area.....	106
4.3.2 Projecting dynamic water stress through the 21 <sup>st</sup> century.....	114
4.4 Discussion.....	119
4.4.1 Incorporating topography in models of tree water stress .....	119
4.4.2 Limitations.....	121
4.4.3 Modeling future tree water stress .....	122
5. Projecting tree species abundance shifts in response to drought across Texas into the 21st century.....	126
5.1 Introduction.....	126
5.2 Methods .....	129
5.2.1. Plot-level data .....	129

5.2.2 Explanatory covariates .....	130
5.2.3. Joint species distribution modeling .....	132
5.3 Results .....	134
5.4 Discussion.....	145
6. Conclusion .....	151
Appendix A.....	156
Appendix B .....	157
B.1 Canopy loss maps: remotely sensed observations .....	157
B.1.1 Fine-scale canopy loss maps: training and testing data .....	157
B.1.2 Regional coarse-scale 30-m binary canopy loss maps .....	160
B.2. Identifying climatic thresholds that control spatial patterns of canopy loss and determining whether these thresholds are likely to be surpassed in the future and identifying impacted ecological systems .....	166
Appendix C.....	176
C.1 Analytical solutions for static water stress and crossing properties .....	177
C.1.1 Soil moisture probability distribution under steady state conditions .....	177
C.1.2 Analytical solution for static water stress .....	178
C.1.3 Analytical solution for $Tsm$ and $nsm$ .....	179
Appendix D.....	180
References .....	187
Biography .....	206

## List of Tables

Table 1: Summary of vegetation indices considered in the analysis .....	26
Table 2: Covariates considered in modeling: ranges of values in the training dataset compared to the percent of pixels across the study area that fell outside of these ranges. ....	29
Table 3: Vegetation indices selected for each model: zero-inflated modeling approach using RF vs. the ZOIB regression model. ....	37
Table 4: Model comparison (60 m). Models in bold had decreasing error (MAE or RMSE) compared to the base model.....	39
Table 5: Spatially independent error rates for final canopy models comparing RF and ZOIB.....	42
Table 6: Climate data (historical averages and 2011 values) for the six modeling zones.	58
Table 7: Landsat vegetation indices and auxiliary explanatory variables considered in random forests models.....	63
Table 8: Accuracy of random forests models in distinguishing pixels of canopy loss (>25%) from pixels of no (0%) canopy loss.....	70
Table 9 Summary of percent forest cover lost and impacted area by modeling zone .....	73
Table 10: Summary of linear regression coefficients: a comparison of drought-impacted area to model outputs forced with the climate anomalies observed in 2011 .....	111
Table 11: Summary of logistic regression coefficients and outputs of the ROC curve analysis for models of increasing complexity,.....	114
Table 12: Comparison of future water stress projections of dynamic water stress for models with and without landscape heterogeneity.....	119
Table 13: Basal area and percent loss in basal area for the 30 most dominant species in Texas, aggregated across the FIA plots.....	135
Table 14: Projected decreases (in bold) vs increases in basal area from the baseline (current, 2015, post-drought climate) compared to 2060-2099 climate conditions under	

representative concentration pathway, RCP, 4.5 and 8.5 trajectories, for 30 abundant species across Texas.....	143
Table 15: Field site location and number of plots collected at each site.....	159
Table 16: Rules for determining the health status of a tree on the ground.....	160
Table 17: Selected Landsat scenes. Base (B) and fill (F) scenes are both provided for scenes that required filling due to clouds and cloud shadows .....	163
Table 18: Final covariates selected for each model and variable importance measures (mean decrease in accuracy). L5 (Landsat 5) pre-drought 2009 or 2010 images and L8 (Landsat 8) post-drought 2013 or 2014 images.....	165
Table 19: Probability thresholds (T) used to distinguish areas of canopy loss (>25%) from areas of no (0%) canopy loss. The group of Landsat scenes (Path/Row) used to select each threshold is also provided in parentheses.....	166
Table 20: Drought impact on all tree-dominated ecological systems in Texas .....	168
Table 21: Comparison of general circulation models in predicting annual rainfall (mm) from 1980 to 2005, ranked from lowest to highest mean absolute error (MAE) .....	176
Table 22: Common name, genus, species, symbol, and predominate location where the species can be found, East (E) of West(W) or both for the 76 species considered in the model.....	184

## List of Figures

Figure 1: Study area (Landsat scene path 28/row 39) in the Edwards Plateau/ Llano Uplift region of central Texas .....	15
Figure 2: Canopy loss examined across scales .....	17
Figure 3: Percent cover observed in the orthophoto classifications (1 m, spatial resolution) compared to percent cover observed on the ground (21 plots) for percent canopy loss (left) and percent post-drought live cover (right).....	35
Figure 4: Distribution of live canopy and canopy loss across a gradient of pre-drought live canopy, from sparse to closed canopy woodlands, using data from the orthophotos. Error bars represent MAE (km <sup>2</sup> ) for the canopy loss in scaling up to a 60-m grid cell.....	43
Figure 5: Coarse-scale continuous canopy loss (60-m), quantified across the study area (Landsat scene path 28/row 39) in the Llano uplift & Edwards plateau region of central Texas. The insets of the orthophotos are false color composite images (NIR, R, G). .....	44
Figure 6: Modeling zones of Texas characterized as temperate deciduous forest, grassland, and desert biomes .....	57
Figure 7: Field validation: canopy loss and live canopy cover measured using ground transects (2013-2014) compared to canopy loss and live canopy cover observed in the 1-m orthophoto classifications (imagery from 2010 and 2012). .....	69
Figure 8: Drought impacted area (> 25% canopy loss per pixel) across Texas.....	72
Figure 9: Climatic drivers of the spatial patterns of canopy loss across Texas. ....	74
Figure 10: Historical and future projections of climate threshold crossings associated with canopy loss.....	76
Figure 11: Percent of time for which a climate threshold (defined in Figure 9) was surpassed, considering 20 general circulation models (GCMs) over the latter half of the 21st century (2050-2099).....	78
Figure 12: The top 10 ecological systems with the highest relative loss (top) and lowest relative loss (bottom), due to the 2011 drought, as quantified through an overlay of our canopy loss maps with an ecological systems map (Elliott et al., 2014).....	79

Figure 13: Comparison of (a) drought-impacted area, as defined as pixels with > 25% canopy loss acquired from Schwantes et al., (2017), (b) soil depth and (c) soil texture, both acquired from the SSURGO database. ....	95
Figure 14: Comparison of spatially explicit input variables of (a) soil depth, (b) topographic compound index (TCI) and (c) heat load index to (d) 30-m remotely sensed drought-impacted area maps. ....	108
Figure 15: Modeled dynamic water stress decreased with increasing (a) soil depth and no lateral redistribution ( $f = 0$ ) and (b) topographic compound index (TCI, forced with average soil depth and a clay loam soil texture) .....	110
Figure 16: Accuracy in distinguishing drought-impacted stands from homogenous live canopy stands of <i>J. ashei</i> above a certain size threshold (x-axis). ....	113
Figure 17: Comparison of how climate parameters vary with annual precipitation. ....	116
Figure 18: Comparison of how dynamic water stress has changed over the past 30+ years (1980-2016) (Abatzoglou, 2013) and was projected to change in the future 2006-2099, using climate data from two representative concentration pathway trajectories, RCP 4.5 and 8.5 (Abatzoglou & Brown, 2012). ....	117
Figure 19: Sensitivity coefficients ( $f$ ) for covariates where the response matrix included (a) dead and live basal area, Model C (b) only live basal area, Model B and (c) only dead basal area. ....	137
Figure 20: Standardized beta coefficients where the response is on the covariance scale, for each species, including dead and live basal area for two covariates: (a) available water storage and (b) climatic water deficit variability. ....	139
Figure 21: In-sample prediction of (a) total live abundance and (b) percent basal area loss compared to observed values in FIA plots for Model C. ....	140
Figure 22: Percent loss of basal area projected for general circulation model, MIROC5, under two representative concentration pathways 4.5 and 8.5 from 2060-2099. ....	141
Figure 23: Comparison of species-specific abundance (basal area) for two species: water oak, <i>Quercus nigra</i> (top) and redberry juniper, <i>Juniperus pinchottii</i> (bottom). ....	144
Figure 24: Change in forest vs. woodland dominant tree species from current 2015, post-drought climate to future climate projected from 2060-2099 .....	145

Figure 25: Comparison of the effect of increasing aggregation on model error. ....	156
Figure 26: Species-specific beta coefficients for the covariate percent clay .....	180
Figure 27: Species-specific beta coefficients for the covariate percent sand .....	180
Figure 28: Species-specific beta coefficients for the covariate elevation .....	181
Figure 29: Species-specific beta coefficients for the covariate heat load .....	181
Figure 30: Species-specific beta coefficients for the covariate topographic compound index.....	181
Figure 31: Species-specific beta coefficients for the covariate historical climatic water deficit .....	182
Figure 32: Climatic water deficit (Precipitation minus potential evapotranspiration (P- PET)) normal and standard deviation (sd), projected by general circulation model: MIROC5, under representative concentration pathway (RCP) 4.5 and 8.5 scenarios.....	183

## Acknowledgements

Firstly, I would like to thank all my coauthors, advisors, committee members and collaborators; this dissertation would not have been possible without your advice and support. Specifically, I would like to thank my advisor, Jennifer Swenson, for giving me perspective and encouragement whenever I got stuck in the weeds, and for all the scientific and life advice over the years. I would also like to thank my co-advisor, Rob Jackson, for always making time to read my proposals and manuscripts, for helping me improve my scientific writing, and for wandering through the woodlands of Texas devising new plot designs, despite the  $>100^{\circ}$  F summer temps! I'd like to thank Jim Clark for teaching me Bayesian statistics and giving me a new toolkit for ecological modeling in general. Lastly, I'd like to thank Amilcare Porporato, for teaching me ecohydrology and for encouraging me to approach ecological questions more quantitatively with an engineering perspective.

I'd also like to thank Dan Johnson and JC Domec for teaching me plant physiology field techniques and modeling. I'd like to thank Tony Parolari and Norm Pelak for teaching me how to write quantitative models in ecohydrology. And thanks to Raven Bier and Evan Williams for helping me with fieldwork in Texas and for crawling through mesquite and acacia thickets; your devotion to straight transects was wonderful! I'd like to thank Kelly Howell for teaching me how to write IDL code and for all her endless hours classifying orthophotos. Additionally, thanks to Mariano

Gonzalez-Roglich, Danica Schaffer-Smith, Kemen Austin, and Brenna Forester for being the best lab mates ever, for coaching me to speak more slowly during presentations, and for offering great feedback on my first drafts of manuscripts.

I would like to thank my funding sources, which include a NASA Earth and Space Science Fellowship (NNX13AN86H), a James B. Duke Fellowship, a United States Department of Agriculture/National Institute of Food and Agriculture (USDA/NIFA) grant (2012-68002-19795), a Duke Graduate School Fellowship, and a Nicholas School of the Environment Conservation Fellowship.

I'd like to thank Chris Edgar of the Texas A&M Forest Service for providing us access to his field plot data and advice on field sampling. I'd like to thank the Texas Parks and Wildlife Department (Permit No: 2016-0303), Texas Master Naturalists, and National Forest Service for providing access to land for field sampling and for all the wonderful stories, scientific ideas, and insight into Texas's forests and woodlands.

And lastly but not least, I'd like to thank my family and friends for all their support over the last 5 years! And most importantly, my husband, Eugene, thanks for all the encouragement, statistics help, and for making me laugh through the days that seemed impossible.

# 1. Introduction

## 1.1 *Why study drought-induced tree mortality?*

With continuing climate change, the intensity, frequency and duration of droughts and heatwaves is projected to increase. As such, forests are expected to become increasingly vulnerable to drought-induced tree mortality (C. D. Allen, Breshears, & McDowell, 2015). Currently tree mortality due to drought has been observed worldwide (C. D. Allen et al., 2010), including both increases in background mortality rates (van Mantgem et al., 2009) and regional die-offs (Breshears et al., 2005). Due to increases in temperature associated with climate change, droughts are now more likely to occur simultaneously with heatwaves (AghaKouchak, Cheng, Mazdidasni, & Farahmand, 2014). These 'hotter droughts' can lead to greater vulnerability of forests to drought-stress by increasing respiration, and thus the likelihood for carbon starvation, as well as atmospheric water demand, and thus the possibility of hydraulic failure (C. D. Allen et al., 2015).

Drought-induced tree mortality can cause profound ecological, biogeochemical, and biophysical changes to ecosystems. Tree mortality can alter community composition (Mueller et al., 2005), food webs (Carnicer et al., 2011), and phenology (Ivits, Horion, Fensholt, & Cherlet, 2014). Canopy loss can also lead to changes in carbon cycling (Ciais et al., 2005; Michaelian, Hogg, Hall, & Arsenault, 2011), ecohydrology (H. D. Adams et al., 2012), stream flow (Guardiola-Claramonte et al., 2011), and biophysics (Robert B

Jackson et al., 2008; Rotenberg & Yakir, 2010). Forests provide important ecosystem services; however, their fate under a changing climate with increased drought and heatwaves is uncertain.

Developing remote sensing protocols capable of measuring drought-induced tree mortality is essential. Many global vegetation models are rarely validated or calibrated using regional-scale estimates of drought-induced tree mortality, because few such datasets exist (McDowell et al., 2011). Regional observations of tree mortality are needed to calibrate and validate global vegetation models to improve forecasts of forest response to drought under climate change. Remote sensing approaches tailored for detecting drought-induced tree mortality are therefore needed. Drought is different from other stand-replacing disturbances, like fire or pest outbreaks, because some trees may die within a stand, but neighboring trees may remain alive. Disturbances that kill entire stands of trees are easier to quantify using remote sensing compared to disturbances, like drought, that are diffuse (McDowell et al., 2015). Detection techniques must be capable of measuring scattered and subtle canopy cover changes across large areas. Many techniques have been proposed such as spectral mixture analysis (Huang & Anderegg, 2012), and time-series of spectral indices (Meddens, Hicke, Vierling, & Hudak, 2013; Vogelmann, Tolk, & Zhu, 2009), but most of these methods were designed for single ecological systems with a few dominant species.

Empirical relationships between tree mortality and climate can be used to improve forecasts of forest response to a changing climate. Until we have enough data to parameterize global models and full understanding of the mechanisms surrounding tree death, identifying quantitative relationships between climate and tree mortality may improve forecasts of forest responses to climate change (H. D. Adams et al., 2013). Other studies have also linked climate anomalies to tree mortality, including the development of a forest drought-stress index using tree-ring data in the southwest United States (Williams et al., 2013), as well as field-based studies in Australia (Phillips et al., 2010) and Amazonia and Borneo (Mitchell, O'Grady, Hayes, & Pinkard, 2014). Only a few studies have related remotely-sensed observations of canopy loss to climatic anomalies, including precipitation and vapor pressure deficit anomalies in a sub region of New Mexico (Clifford, Royer, Cobb, Breshears, & Ford, 2013) and Climatic Water Deficit anomalies in a sub region of Colorado (Anderegg et al., 2015).

Many mortality algorithms in global vegetation models include climate or heat stress thresholds (McDowell et al., 2015); however, spatial patterns of tree mortality often follow local water stress gradients and depend on soil conditions and landscape position, in addition to climate (Gitlin et al., 2006; Loehle & LeBlanc, 1996; McLaughlin et al., 2017). Although many studies have focused on improving our understanding of the internal physiological mechanisms by which tree death occurs, fewer studies have focused on accounting for spatial variability in soil conditions and topography on tree

mortality (Anderegg et al., 2015; Tague, McDowell, & Allen, 2013; Tai, Mackay, Anderegg, Sperry, & Brooks, 2017). Tree mortality is often associated with spatially variable soil texture and depth (Bowker, Muñoz, Martinez, & Lau, 2012; Peterman & Waring, 2014; Twidwell et al., 2014), surface run-off and lateral redistribution of water (K. J. Beven & Kirkby, 1979; Dunne, Moore, & Taylor, 1975), and differences in radiation due to aspect and slope (McCune & Keon, 2002; I. D. Moore, Grayson, & Ladson, 1991). Landscape diversity, caused by this spatial variation of edaphic factors, creates microsites with cooler, moister conditions that allow trees to persist even under severe drought conditions. However, rarely is landscape diversity considered, even though it is important towards identifying refugia that are locally buffered from climate change.

As forests respond to recent severe drought events, differential tree mortality is already being observed. Some species are more vulnerable to drought-stress than others, which leads to re-organization of tree communities. Typically we use species distribution models (SDMs) to predict changes in species abundance; however, rarely are these models validated against mortality datasets at regional scales. As droughts become more severe, we can use observations of species-specific mortality due to recent severe droughts to validate models. Moreover, typically community level shifts occur during severe droughts/heatwaves (e.g., in pulse events). Climate variability in addition to average climate can control species distributions (Zimmermann et al., 2009); therefore,

by including covariates related to climate variability we can account for species-specific tolerances to extreme climate events.

Texas was selected as the study area, because firstly a record drought and heatwave occurred in 2011 and secondly the state has a large precipitation gradient that spans from humid to semi-arid regions. According to historical Palmer Drought Severity Index (PDSI) data from 1895-2011, the 2011 drought had the lowest PDSI of -7.93 on record (Hoerling et al., 2013). The period from Oct 2010 to Nov 2011, was also the driest 12-month period (Hoerling et al., 2013), with a record high vapor pressure deficit (VPD) (Williams et al., 2014). Over 200 ecological systems dominated by tree species exist across the state. These systems span a 5-fold precipitation gradient that transitions from humid to semi-arid. Therefore, the most arid edges of many species ranges are located in Texas (e.g., the eastern hardwoods). Drought-induced tree mortality is likely to be greatest along these trailing range edges (Jump, Mátyás, & Peñuelas, 2009).

## ***1.2 Research objectives***

Drought-induced tree mortality is a unique disturbance, because drought affects large areas, but the impact is often diffuse or scattered, which causes mixed pixels (e.g. pixels containing both live canopy, canopy loss, and non-tree cover types), and median-zero datasets (e.g., there are often many more homogenous live canopy pixels compared to drought-impacted pixels). I developed two remote sensing approaches capable of accommodating median-zero datasets and mixed pixels. In the first approach for a

woodland system in central Texas, I used a time-series analysis to remove pixels of no-change, to reduce issues with zero inflation. I then also used a zero-or-one inflated beta regression model (Ospina & Ferrari, 2012), which accommodates continuous proportion data, to quantify the proportion of canopy loss per pixel. In the second approach, I used random forest (Breiman, 2001) to create binary canopy loss maps across the diverse ecoregions of Texas. Most remote sensing studies focus on detecting drought-stress in one system with a couple dominant species, whereas as in this dissertation I developed an approach capable of quantifying canopy loss across the diverse systems of Texas, ranging from humid to semi-arid ecosystems. I then used these canopy loss observations to calibrate and validate models, to improve forecasts of forest responses to future droughts.

Firstly, I defined empirical relationships between climate anomalies and canopy loss. I addressed the question: *Is there greater mortality, when a specific climatic threshold is surpassed? And how often are these mortality-thresholds likely to be crossed in the future?* Most studies linking remotely sensed observations of canopy loss to climatic anomalies are for a single ecological system, with a couple dominant species (Anderegg et al., 2015; Clifford et al., 2013), whereas in this study I examined observations of canopy loss across a 5-fold precipitation gradient from humid to semi-arid regions, spanning 200 tree-dominated ecological systems (Elliott et al., 2014).

Secondly, I used a statistical-dynamical model of soil-plant water, that was forced using stochastic precipitation (Laio et al., 2001; Rodriguez-iturbe & Porporato, 2004), and that included both simplified mortality mechanisms (Parolari et al., 2014) and spatially variable input parameters. I addressed the question: *Will landscape heterogeneity create microsites or refugia that are locally buffered from future droughts projected in the 21<sup>st</sup> century?* The approach was unique in that I included plant hydraulics as well as landscape processes related to spatially variable soil conditions, lateral redistribution of water, and heat load affects due to aspect and slope. When projecting future water stress, we can account for potential microsites/refugia by incorporating landscape diversity into models.

Thirdly, I used a generalized joint attribute model, GJAM, (Clark, Nemergut, Seyednasrollah, Turner, & Zhang, 2017) to address the question: *Are we likely to see shifts in species compositions following increases in droughts and heatwaves projected with climate change?* The approach was unique, because unlike traditional SDMs, GJAM is multivariate and accounts for joint species-specific responses as well as the environment. I modeled species-specific live and dead basal area simultaneously, and included covariates related to climate variability, instead of only relying on covariates related to average climate conditions. Moreover, rarely are SDMs validated against regional observations of canopy loss. However, as droughts have already led to differential tree

mortality, I tested whether GJAM could predict drought-induced tree mortality that had recently occurred due to the severe 2011 drought in Texas.

### **1.3. Dissertation Outline**

I developed two remote sensing approaches to quantify canopy loss from the 2011 drought. Firstly in chapter 2, I explored an approach capable of measuring canopy loss in open canopy systems in central Texas. I conducted a time-series analysis to identify areas with persistent canopy loss, and then within these areas, I estimated percent tree canopy loss using a zero-or-one inflated beta regression model. In chapter 3, I explored a new approach capable of quantifying canopy loss across the many diverse ecological systems in Texas, by scaling from field estimates to 1-m orthophotos to 30-m Landsat imagery, using Random Forest.

I then used these canopy loss maps to improve upon modeling efforts and thus future predictions of tree water stress and potential community shifts. In chapter 3, at the regional scale, across Texas, I identified climatic anomalies associated with spatial patterns of canopy loss and forecasted how often these thresholds were likely to be surpassed in the future. In chapter 4, at the watershed scale, I built a quantitative model of soil moisture dynamics across a landscape, while accounting for spatial differences in aspect, topography, and soils. Lastly, in chapter 5, again at the regional scale, I modeled both species-specific live and dead basal area, using GJAM and then projected changes in species abundance through the 21st century.

In summary, I developed two remote sensing approaches capable of measuring drought-induced tree mortality in Texas, one focused on a woodland system, and a second general approach focused on quantifying canopy loss across Texas. I then explored multiple modeling approaches capable of improving our ability to forecast forest water stress given continuing climate change. I explored (1) defining empirical relationships between climate anomalies and canopy loss regionally, (2) employing a non-linear stochastic, ordinary differential equation of soil moisture dynamics to examine water stress locally within a watershed, and (3) using GJAM to forecast how species-specific abundances may change into the 21<sup>st</sup> century.

## **2. Quantifying Drought-Induced Tree Mortality in the Open Canopy Woodlands of Central Texas**

### ***2.1 Introduction***

Tree mortality due to drought is increasing worldwide (C. D. Allen et al., 2010), ranging from small but consistent increases in background mortality rates (van Mantgem et al., 2009) to extensive regional die-offs (Breshears et al., 2005). This increased mortality will likely have large ecological consequences by altering plant community composition, species distributions (Engelbrecht et al., 2007; Mueller et al., 2005; Willson, Manos, & Jackson, 2008) and carbon (Michaelian et al., 2011) and water cycling (Guardiola-Claramonte et al., 2011). Establishing protocols capable of detecting drought-induced tree mortality is therefore essential.

From October 2010 to September 2011, Texas experienced the most severe one-year drought since record-keeping began in 1895 (Hoerling et al., 2013). A recent modeling study suggests that the likelihood of abnormally high summer temperatures has increased in Texas (Rupp et al., 2015). However, it is difficult to quantify changes in the probability of an extreme event, and thus challenging to definitively link the 2011 drought with directional climate change. Nevertheless, general circulation models predict that subtropical dry zones, which include our study area, will become drier as climate change advances (Seager, Naik, & Vecchi, 2010). Additionally, even without decreasing precipitation, warmer temperatures will increase the frequency of droughts, affecting ecosystems faster and more intensely than in recent decades and centuries

(Trenberth et al., 2014), likely leading to increased vulnerability of trees to drought stress (C. D. Allen et al., 2015).

Currently DGVMs (dynamic global vegetation models) are being used to predict how ecosystems will respond to rising CO<sub>2</sub> concentrations. These models include multiple atmosphere-biosphere interactions and feedback effects. However, the mortality algorithms in DGVMs are not typically tested or calibrated with empirical data due to a lack of systematic observations of tree mortality at regional/global scales (McDowell et al., 2011). Therefore, defining methods capable of quantifying tree mortality regionally using remotely sensed data is essential (McDowell et al., 2015), in part because improving the predictive capability of DGVMs could aid in our ability to forecast tree mortality in the face of climate change.

Already, Landsat data have played a pivotal role in our understanding of forest disturbance, being used to observe the Earth surface for 40+ years and having been designed to achieve a balance between spatial and temporal resolutions ideal for detecting forest change at scales relevant to ecology (Cohen & Goward, 2004). Previous studies have used Landsat time-series to quantify tree mortality from disturbance events due to fire (Collins et al., 2009), insects in combination with drought (Clifford et al., 2013; Meddens & Hicke, 2014; Meigs, Kennedy, & Cohen, 2011) and clear-cut logging (Cohen, Fiorella, Gray, Helmer, & Anderson, 1998). However, fewer studies have examined ecosystems where the disturbance's proximate cause is directly from drought.

Drought-induced tree mortality is a unique forest disturbance. It can occur broadly and simultaneously across a landscape, without geographic proximity, and unlike other disturbances such as fire and pests, there is typically no centralized starting location. Detection methods must be capable of quantifying scattered and subtle changes in canopy cover across large regions. Stand-replacing disturbances, such as fire, are easier to detect compared to disturbances that are diffuse and heterogeneous, such as drought (McDowell et al., 2015).

Most forest change detection studies classify an entire pixel as either disturbed or undisturbed (a binary per-pixel classification); however, for drought-induced tree canopy loss most pixels are mixtures of both live and dead canopy. To add to the complexity, our study site is dominated by open canopy woodlands, with an average canopy cover of only ~46% before the drought, as measured in this study. Binary per-pixel classification approaches are often inadequate in detecting subtle changes in land cover, especially in these mixed-cover systems, for instance, where a pixel could have started with only 50% canopy cover and lost 10% during the drought.

Typically, sub-pixel estimates of canopy cover use Spectral Mixture Analysis (SMA). However, our study region is composed of diverse natural systems, and as such the number of endmembers required for SMA would be larger than the spectral resolution of Landsat. Fewer studies have explored alternatives to SMA that are still capable of detecting percent canopy loss within a pixel. Of these studies, continuous tree

canopy loss is usually modeled using linear regressions (Meddens & Hicke, 2014). However, for the modeling of continuous proportions, such as canopy cover loss within a pixel, linear regressions are typically not suitable (Ospina & Ferrari, 2012). Proportions are inherently bounded on the interval from 0 to 1. Therefore, this type of data defies two assumptions of a normal linear regression: (1) the relationship is non-linear and (2) the variance is heteroskedastic, because as the mean approaches the bound, the variance approaches zero (Kieschnick & McCullough, 2003). Linear regressions are especially not suitable if a dataset is zero-inflated. Zero-inflation occurs when a dataset includes an excessive number of zeros, and is common in most remotely sensed mortality datasets, because much of the landscape remains undisturbed. Instead, we propose two approaches that can more adequately handle zero-inflated continuous proportions: (1) a zero-inflated modeling approach using random forest, RF, (Breiman, 2001), as used in Savage, Lawrence, & Squires, (2015), and (2) a zero-or-one inflated beta regression model, ZOIB (Ospina & Ferrari, 2010).

We quantify drought-induced canopy loss by first filtering mortality (canopy loss) pixels from no-change pixels (pixels with no canopy loss) based on a Landsat time-series analysis (2000-2014). Then, using Landsat data from before and after the drought, as well as auxiliary variables, we model continuous canopy loss over a region. We build and validate models using training and testing data from fine-scale orthophoto classifications that span a subset of the study area, and then use these models to predict

canopy loss across the entire region. Our goal was to design a method capable of detecting drought-induced canopy loss in open canopy forests, by (1) filtering canopy loss from non-change pixels beyond simple thresholds, (2) detecting continuous canopy loss within a pixel, and (3) addressing zero-inflation.

## **2.2 Study area**

The study area was located in the Edwards Plateau and Llano Uplift regions of central Texas (Figure 1). The average annual precipitation (1980-2010) was 73 cm (Thornton et al., 2014; Thornton, Running, & White, 1997). Average annual daily mean and max temperatures (1980-2010) were 18.5 and 38.5°C, respectively. In 2011, the region received only 34 cm of rain, coupled with higher mean and maximum temperatures of 19.6 and 41.2 °C, respectively (Thornton et al., 2014).

Dominant tree species in the Edwards Plateau & Llano Uplift region include *Juniperus ashei* (ashe juniper), *Quercus fusiformis* (plateau live oak), *Quercus stellata* (post oak), *Ulmus crassifolia* (cedar elm), and *Prosopis glandulosa* (honey mesquite) (Elliott et al., 2014). Our analysis only included areas that were forested; a binary forest cover mask was created by including all ecological systems from the Texas Ecological Systems Map (Elliott et al., 2014) dominated by tree species. Growth form (shrub vs. tree) was defined using the United States Department of Agriculture (USDA) plants database (USDA NRCS Natural Resources Conservation Service, 2015). We also excluded areas

influenced by fire using data from the Monitoring Trends in Burn Severity project (USDA Forest Service/U.S. Geological Survey, 2014).

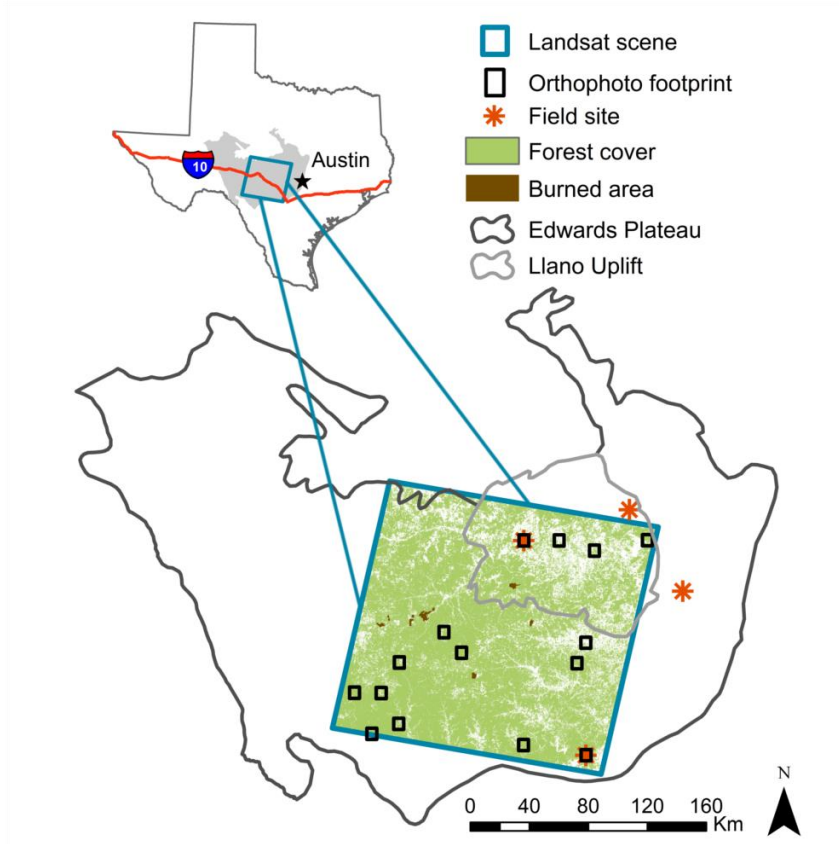


**Figure 1: Study area (Landsat scene path 28/row 39) in the Edwards Plateau/ Llano Uplift region of central Texas**

### **2.3 Methods**

To obtain estimates of tree canopy loss across an area  $> 30,000 \text{ km}^2$  in central Texas, we first created a subsample of fine-scale canopy loss maps based on orthophotos (1-m) from the U.S. National Agriculture Imagery Program (NAIP). A Landsat time-series analysis (2000-2014) was used to filter areas with canopy loss from regions

experiencing no change, using the Landtrendr algorithm. Landtrendr is a time-series change detection algorithm, specifically designed for Landsat data (Kennedy, Yang, & Cohen, 2010). Pixels containing burned areas, non-forest, or no canopy loss were excluded from the analysis. We then built models, relating the fine-scale canopy loss maps to coarse-scale Landsat imagery. These models were used to predict post-drought proportion canopy loss and live canopy across the study area at a 60-m spatial resolution (Figure 2).

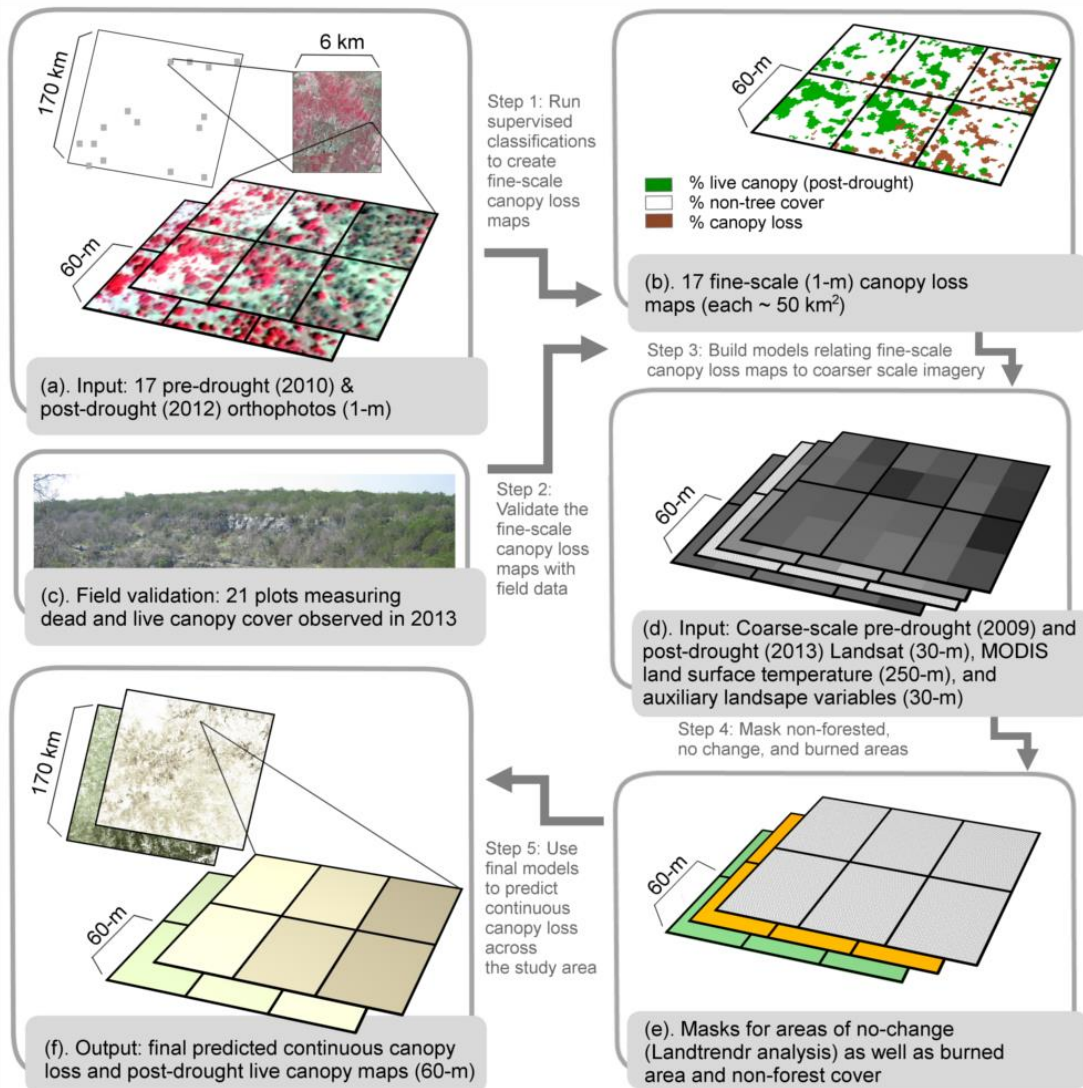


**Figure 2: Canopy loss examined across scales: (a) orthophotos (1 m) are used to create (b) fine-scale canopy loss maps (1 m), which are then validated with (c) ground observations of canopy cover loss. Then models are built relating these fine-scale canopy loss maps to (d) coarser scale Landsat and MODIS imagery. Pixels of (e) non-forest, no-change, or burned area were removed from the study area. Finally these models were used to predict (f) regional coarse-scale continuous live canopy and canopy loss, across the study area, aggregated to a spatial resolution of 60-m.**

## 2.3.1. Creating fine-scale canopy loss maps

### 2.3.1.1 Classification of orthophotos

NAIP digital orthophotos (1 m) were used to create high resolution canopy loss maps to act as training data for coarser scale images. NAIP images (US Department of Agriculture, 2014) for our area contain four bands (red-R, green-G, blue-B, and near infrared-NIR) and are taken during the growing season. These images were already orthorectified to within +/- 6-m to true ground, and tiled using 3.75' x 3.75' quarter quads. Thirteen quarter quads were randomly chosen as training/testing data for this study. Only quarter quads with cloud-free images were included. To match images with field data for validation, four additional quarter quads were selected over areas with access in the field, which is restricted across the study area. Two of these four quarter quads were used exclusively for field validation, because they fell outside of the Landsat scene, but still within the natural systems that were the focus of this study: the Edwards plateau and the Llano uplift (Fig. 1).

The 17 quarter quad NAIP image pairs, one from pre-drought (2010) and one from post-drought (2012), were co-registered (each with 30 manually chosen tie points, 1st or 2nd order polynomial warping transformation, Root Mean Square Error, RMSE <1.0 m, and nearest neighbor resampling). Then normalized difference vegetation index (NDVI) and the original R, G, B, NIR bands, both from before and after the drought, were included in one image stack for each of the 17 quarter quads. A supervised classification was performed on each multi-date stack (10 bands: 2010 - R, G, B, NIR,

NDVI and 2012 - R, G, B, NIR, NDVI) using the maximum likelihood algorithm.

Training data were identified by manually delineating dominant features within each scene as well as features that changed through time from 2010 to 2012. Post-processing of these classifications included grouping these sub-classes into three main classes: (1) live canopy (e.g., live trees, shrubs, barely alive/thinned canopies); (2) canopy loss (e.g., originally live canopy in 2010 and then dead canopy in 2012) and (3) non-tree cover (e.g., agriculture, shadows, water, urban, pasture, bare soil). Isolated groups of three pixels were removed and re-classified using a 3 by 3 majority filter.

#### **2.3.1.2 Accuracy assessment of fine-scale canopy loss maps with field surveys**

Canopy cover loss was measured in the field in four sites across the Edwards Plateau and Llano Uplift region in July 2013, two years after the drought. At each of the 4 sites, 3-6 plots were sampled for a total of 21 plots. Within each site, plot locations were selected using a stratified random sample. For each of the four fine-scale canopy loss maps, three equal area strata were assigned based on tree canopy cover loss (high, medium, & low). Thresholds unique to each image were chosen so that an equal area of the image was assigned to each of the three strata. An equal number of plots were then randomly selected within each stratum. This ensured that the entire range of canopy cover loss was sampled within a site, but that all areas had an equal probability of being selected. If a plot location contained evidence of a disturbance other than drought (i.e.

fire) that could have occurred after the drought (2011) but prior to our field campaign (2013), then a new plot location within the same stratum was selected.

For each 50 x 50-m field plot, we used the line-intercept method to measure canopy cover (to the nearest 0.1 m) along four 25-m transects running from the randomized plot center in each of the four cardinal directions (N, E, S, W). Along each transect the health status of the tree or shrub was also recorded as either dead or alive. We assumed that the canopy death observed along each transect happened during the 2011 drought interval. For example, background mortality rates in east Texas are typically low ~0.7% (G. W. Moore et al., 2016); therefore, very few dead standing trees were present in these plots prior to the drought. Trees, which appeared dead for greater than 3-4 years (e.g. missing bark and medium to large branches), were not counted as dead as a result of the 2011 drought. A perpendicular metal sampling rod was used to estimate the intersection of a tree's canopy with the measuring tape. When trees were taller than the 2.5-m sampling rod, a GRS densitometer (sighting device) was used to estimate canopy cover. Only woody shrubs and trees over 1-m tall were counted. Transect length was corrected for slope, in steep terrain (slope >5°). GPS points were collected at the plot center and later differentially corrected. The proportion of live and dead canopy along each of the four line-transects was averaged, to obtain estimates of the average live canopy and canopy loss for each plot. These ground plot measurements were then compared to the 1-m orthophoto classification corresponding to each site,

where the proportions of post-drought live canopy pixels and canopy loss pixels were estimated within a 25-m radius circular buffer from each plot's center. Four of the seventeen classifications were validated with field data to test the accuracy of the fine-scale (1 m) canopy loss classifications. However, only 15 out of the 17 classifications were used in scaling up to create coarse-scale regional canopy loss maps.

### **2.3.2. Creating coarse-scale canopy loss maps: pre-processing steps**

We acquired Landsat imagery from before and after the drought. Areas of no canopy loss were masked using a Landsat time-series analysis. Then, grids aligned with the 30-m Landsat pixels were placed over the 1-m fine-scale tree canopy loss maps. Proportions of live, canopy loss, and non-tree cover were then extracted for each 30-m grid cell. These percent canopy loss observations were then used to calibrate the Landsat imagery overlying the footprints of the orthophoto classifications.

#### **2.3.2.1 Pre-processing of Landsat imagery**

Pre-drought and post-drought images were selected for dates on July 10, 2009 & July 5, 2013, respectively. We acquired atmospherically corrected images from the Landsat surface reflectance product (Masek et al., 2006). Through visual inspection, 1-m fine-scale canopy loss maps, which showed imperfect registration with the Landsat scenes, were manually co-registered to the Landsat images to achieve a RMSE < 0.5 of a Landsat pixel.

### **2.3.2.2 Filtering canopy loss from no-change pixels: Landtrendr algorithm**

Some parts of our study region experienced no canopy loss; therefore, the dataset was highly zero-inflated, which can limit model performance. To concentrate the analysis only on pixels that actually contained canopy loss, a Landsat time-series analysis was conducted to distinguish pixels with change in canopy cover from pixels with noise resulting from year to year atmospheric effects, geometric mis-registration, and/or shadowing or other illumination differences (Kennedy et al., 2010). Changed vs. unchanged areas have also been delineated in other studies by setting thresholds, using the difference in a vegetation index between two time-periods (Rogan, Franklin, & Roberts, 2002). We chose to use a more rigorous time-series analysis to identify areas undergoing a persistent change in canopy cover.

We selected late-summer Landsat 5, 7 & 8 images (path 28/row 39) from 2000 to 2014. Images with clouds or gaps attributable to scanline errors (Landsat 7) were filled in by other imagery to obtain cloud-free aggregates from 2000 to 2014. By late summer at our study site, herbaceous vegetation has typically senesced, thereby allowing for better differentiation between tree mortality and grass/cropland senescence. We calculated NDVI for each cloud-free image composite of late-summer Landsat imagery from 2000-2014. We then applied the Landtrendr temporal segmentation algorithm to this NDVI time-series. The segmentation fitting protocol is capable of capturing both long-term trends and abrupt events (Kennedy et al., 2010). Following segmentation, we extracted

maps of segments containing the most recent disturbance in the time-series. If the year 2011 or after occurred within that segment, then the pixel was classified as having experienced canopy loss. No-change pixels were considered to have 0% canopy loss, and canopy loss pixels were used in the next steps to create continuous canopy loss maps. Isolated pixels of no-change that were surrounded by canopy loss pixels were removed and reclassified as canopy loss using a 3 by 3 majority filter, applied twice. Across the study area, 44% of the pixels were considered no change.

Typically, Landtrendr is parameterized to achieve a balance of false positives (no-change pixels that were considered change), and false negatives (change pixels that were considered no-change); however, we evaluated several different parameter values and selected the final parameterization that strongly minimized false negatives at the expense of also selecting for more false positives. We did this to ensure that pixels containing canopy loss were not removed as no-change, because drought-induced tree mortality can cause subtle changes in canopy cover. Furthermore, both the zero inflated modeling approach using RF (Savage et al., 2015) and ZOIB regression models are capable of handling some zero-inflation, and thus these false positives were filtered out in subsequent steps.

### **2.3.2.3. Scaling up to create regional continuous canopy loss maps**

Proportional canopy loss, post-drought live canopy, and non-tree cover from the 15 fine scale canopy loss maps were extracted for each 30-m Landsat pixel. The data

were then aggregated to 60-m to minimize the effect of misalignment errors between the orthophotos and Landsat. Data aggregation occurred by taking the mean value of all 30-m pixels within the 60-m grid cell. We decided on an aggregation level of 60-m by testing multiple aggregation levels (Figure 25, appendix A). The 60-m spatial resolution decreased the error rate significantly, while only marginally increasing the spatial resolution of Landsat. Only forested and non-burned pixels with greater than zero canopy loss were considered in the analysis. The proportions of post-drought canopy loss and live canopy within each 60-m grid (75,716 cells total) were then used to calibrate and validate the coarse-scale 60-m aggregated Landsat imagery, within the footprint of the orthophoto classifications.

### **2.3.3 Creating coarse-scale canopy loss maps: variable selection and modeling**

To predict canopy dynamics across a broad area based on the fine-scale maps, we tested the predictive power of two models (RF and ZOIB) by comparing two designs for the training and testing data: (1) where testing and training datasets were close in proximity and (2) where the testing data was spatially independent of the training data. Many studies use either plot data or fine-scale imagery in scaling up to regional estimates; however, often this training/testing data is from only a spatial subset, and yet used to validate the predictive power of the model across an entire region. We explored using spatially independent testing data, which proved to be a more accurate representation of the predictive capability of a model (González-Roglich & Swenson,

2016). We built models relating the canopy loss observed in the orthophoto classifications to the Landsat data and auxiliary explanatory variables within the footprints of the orthophotos, which cover approximately 2.4% of our study area. We then used the final models to create post-drought continuous (1) canopy loss and (2) live canopy maps across the entire >30,000 km<sup>2</sup> study area.

### **2.3.3.1 Identifying explanatory variables: vegetation indices and auxiliary variables**

Ten vegetation and water indices, including tassell cap transformations, were calculated for the pre-drought (2009) and post-drought (2013) Landsat scenes as well as their difference over time (2013-2009) Table 1). The tassell cap transformation compresses the six original Landsat bands to create three orthogonal indices, brightness, greenness, and wetness (Baig, Zhang, Shuai, & Tong, 2014; Crist, 1985).

**Table 1: Summary of vegetation indices considered in the analysis**

Index	Formula	Citation
Normalized Difference Vegetation Index (NDVI)	L5: $(B4-B3)/(B4+B3)$ L8: $(B5-B4)/(B5+B4)$	(Tucker, 1979)
Normalized Difference Water index (NDWI)	L5: $(B4-B5)/(B4+B5)$ L8: $(B5-B6)/(B5+B6)$	(E. H. Wilson & Sader, 2002)
Normalized Burn Ratio (NBR)	L5: $(B4-B7)/(B4+B7)$ L8: $(B5-B7)/(B5+B7)$	(van Wagendonk, Root, & Key, 2004)
Greenness Normalized Difference Vegetation Index (GNDVI)	L5: $(B4-B2)/(B4+B2)$ L8: $(B5-B3)/(B5+B3)$	(Gitelson, Kaufman, & Merzlyak, 1996)
Ratio SWIR/NIR (B5/B4)	L5: $B5/B4$ L8: $B6/B5$	(Vogelmann & Rock, 1988)
Red Green Index (RGI)	L5: $B3/B2$ L8: $B4/B3$	(Coops, Johnson, Wulder, & White, 2006)
Difference Vegetation Index (DVI)	L5: $(B4-B3)$ L8: $(B5-B4)$	(Tucker, 1979)
Tasseled cap brightness (TCB), greenness (TCG), wetness (TCW)	See citations	(Baig et al., 2014; Crist, 1985)

In addition to the Landsat vegetation indices, six other sets of explanatory variables were considered: (1) percent forest cover, (2) location: latitude & longitude in UTM coordinates, (3) land surface temperature from MODIS, (4) elevation, (5) slope & aspect, and (6) magnitude of change from the time-series analysis using Landtrendr. Percent forest cover was obtained from National Land Cover Database (Homer et al., 2015). To calculate land surface temperature (LST), we used the 8-day 1-km daytime LST dataset from the MODIS/Aqua satellite (MYD11A2; collection 5 (Wan, 2008)). Pre-

processing included the following: (1) removal of poor quality data using the QC flags (data with LST error rates greater than 2 K or emissivity errors greater than 0.02 were excluded), (2) aggregation of the 8-day product to warm season averages (May-September), and (3) resampling to the 60-m aggregated Landsat grid. We used the 2011 LST difference from the historical average (calculated from 2002-2010) in our models.

Elevation, slope and aspect were all computed using the National Elevation Dataset, downloaded from the U.S. Geological Survey. Slope ( $\phi$ ) and aspect ( $\theta$ ) were transformed using the following equations, to account for joint effects (e.g. the influence of aspect would be stronger on steeper slopes). The first two terms include both aspect and slope, and take into account the north-south ( $u1$ ) and east-west gradients ( $u2$ ) of aspect. The last term ( $u3$ ) tests for the influence of slope independent of aspect (Clark, 1990).

$$\begin{aligned}
 u1 &= \cos(\theta) \sin(\phi) \\
 u2 &= \sin(\theta) \sin(\phi) \\
 u3 &= \cos(\phi)
 \end{aligned}
 \tag{Equation 2.1}$$

Each segment in the time-series analysis has an associated magnitude of change, which is computed as the difference in NDVI prior to the disturbance and NDVI after. We also used this magnitude of change estimate as an additional explanatory variable in our models. To verify that prediction outside of the training dataset was appropriate, we compared the range of values for each explanatory variable in the training dataset to the proportion of pixels across the whole study area that fell within that range (Table 2). For

each explanatory variable, less than 0.03% of the pixels in the study area fell outside the range used in training the model, except for the covariates, elevation, latitude, and longitude, which were not used for prediction in the final models.

**Table 2: Covariates considered in modeling: ranges of values in the training dataset compared to the percent of pixels across the study area that fell outside of these ranges.**

Variable	Model (A/CL) <sup>1</sup>	Range (training data)	% pixels in study area outside of the range <sup>2</sup>
<b>Vegetation indices 2009</b>			
NDVI	CL	-0.00165 to 0.821	***
NDWI	CL	-0.506 to 0.341	**
NBR		-0.265 to 0.636	**
GNDVI		-0.0331 to 0.779	***
(B5/B4)		0.493 to 3.05	**
RGI	CL	0.766 to 1.45	**
DVI	CL	12.0 to 3642	***
TCB <sup>3</sup>	CL	-5517 to 6585	***
TCG <sup>3</sup>	CL	-1201 to 1715	**
TCW <sup>3</sup>	CL	-2104 to 6917	***
<b>Vegetation indices 2013</b>			
NDVI	CL, A	-0.194 to 0.863	**
NDWI	CL	-0.299 to 0.405	**
NBR	A	-0.264 to 0.689	***
GNDVI		-0.223 to 0.800	***
(B5/B4)		0.424 to 1.86	**
RGI	CL, A	0.632 to 1.58	**
DVI	CL, A	-253 to 3939	***
TCB	CL, A	778 to 14701	***
TCG	CL, A	-467 to 2724	***
TCW	CL, A	-5240 to 298	***
<b>Auxiliary variables</b>			
% tree cover	A	0.250 to 96.0	***
X		360900 to 566070	1.0%
Y		3263100 to 3416220	11%
MODIS LST	CL	2.93 to 11.3	***
Difference			
Elevation		285 to 721	2.0%
U1		-0.545 to 0.674	***
U2		-0.510 to 0.541	**
U3		0.697 to 1.00	***

Time series	CL, A	0 to 626	***
<sup>1</sup> Indicates if the explanatory variable was used to model Canopy Loss (CL) or Alive (A) cover			
<sup>2</sup> Percent of pixels predicted within the study area that fell outside of the range of the explanatory variables used to train the model			
<sup>3</sup> Indicates that the range of the difference (2013-2009) is provided instead of 2009 values			
*** < 0.01 %		** < 0.03 %	

### 2.3.3.2 Modeling approaches: RF vs ZOIB

Two modeling approaches were used to detect canopy loss within each 60-m grid cell: (1) a zero-inflated modeling approach using RF and (2) a ZOIB regression model. For both modeling approaches, the percent canopy loss in a pixel area was modeled separately from percent post-drought live canopy, with percent non-tree cover computed as the remaining cover not already accounted for by either canopy loss or live canopy. Here, percent canopy loss and percent live canopy are the response variables and the explanatory variables considered are the 20 vegetation indices from Landsat (7 pre-drought, 3 difference, and 10 post-drought), as well as the nine other variables described in section 2.3.3.1. Differences between post-drought and pre-drought indices were used for the three tassel cap bands to minimize correlations between the other vegetation indices.

RF is a machine learning algorithm that averages an ensemble of classification and regression trees (Breiman, 2001; Liaw & Wiener, 2002). To define the split at each node in each regression tree, only a randomly chosen subset of variables is used, in order to limit the correlation between the individual regression trees in the ensemble

(Gislason, Benediktsson, & Sveinsson, 2006). RF is a non-parametric model and thus makes no assumptions as to the distributions of the underlying data. Also, RF allows for multicollinearity among variables (Piramuthu, 2008) and tends not to overfit the data (Gislason et al., 2006). Previously, RF has been used to estimate percent urban land cover (Walton, 2008) or forest cover (González-Roglich & Swenson, 2016) within a pixel but only for single date images.

To model canopy loss, we used a two-step modeling approach to better account for zero-inflation (Savage et al., 2015). First we used RF in classification mode, ensemble of classification trees, to classify pixels into two binary classes (1) absence or (2) presence of canopy loss. We then estimated the proportion of canopy loss for all pixels having some canopy loss, using RF in regression mode, ensemble of regression trees. To predict proportion post-drought live cover within a pixel, we used a one-step RF model, as an ensemble of regression trees, because there were few zeros in the post-drought live canopy dataset.

We did not find that RF was sensitive to parameterization, and therefore we selected a third of the total variables in the model to define each split. We also ran every model with 501 regression trees. For variable selection with the RF model, we first ran a full model, including all 29 explanatory variables, (Table 2), to obtain variable importance estimates. Several variable pairs were redundant ( $|r| > 0.95$ ). To create a

more parsimonious model, for each of the redundant pairs, one variable was removed, while preferentially keeping variables considered most important by the RF model.

The second model tested was a ZOIB regression, which is a mixture of two models: a beta distribution, which models the continuous proportions (0,1) and a degenerate distribution, which models the discrete probability mass at zero or one (Ospina & Ferrari, 2010). When both zeros and ones are present, they are modeled with a Bernoulli distribution (Ospina & Ferrari, 2012). This type of model for example, has been used to predict the percent of an area infected by mountain pine-beetle damage, using climate, slope, and elevation as explanatory variables at coarse scales (Kaufeld, Heaton, & Sain, 2014). To our knowledge, however, it has had limited use in mapping applications, such as to create continuous tree canopy loss maps using remotely sensed data.

We used Generalized Additive Models for Location, Scale and Shape (GAMLSS), (Rigby & Stasinopoulos, 2005) where the distribution for the response variable is a zero-or-one inflated beta distribution for modeling live canopy cover or a zero-inflated beta distribution for modeling canopy loss. As an example for how canopy loss was modeled, the zero-inflated beta distribution has a probability density function as follows (Ospina & Ferrari, 2012):

$$bi(y|\alpha, \mu, \phi) = \begin{cases} \alpha, & \text{if } y=0 \\ (1 - \alpha)f(y|\mu, \phi), & \text{if } 0 < y < 1 \end{cases} \quad \text{Equation 2.2}$$

where  $f(y|\mu,\phi)$  is equal to the density function for the beta distribution,  $\alpha$  is the probability of obtaining zero canopy loss,  $\mu$  is the distribution mean (e.g. the proportion of canopy loss, given that canopy loss is greater than zero), and  $\phi$  is a precision parameter (Ospina & Ferrari, 2012). Under the GAMLSS framework, all the parameters of the zero-inflated beta distribution (e.g.  $\alpha$ ,  $\mu$ ,  $\phi$ ) are modeled as additive functions of the covariates (e.g. post-drought and pre-drought Landsat vegetation indices). There is no ecological reason why certain vegetation indices would be less relevant in predicting the probability of zero canopy loss vs. the proportion of canopy loss if loss occurs. We therefore used the same covariates when modeling  $\alpha$  and  $\mu$ . Furthermore, the output predictions for these models are for each distribution parameter; as such we obtained two predictive maps of  $\alpha$  and  $\mu$ . To create the final canopy loss maps, we assumed that if the probability of obtaining zero canopy loss ( $\alpha$ ) was greater than 1/3, then the pixel had zero canopy loss; otherwise the pixel took the value of the distribution mean ( $\mu$ ) (e.g. the proportion of canopy loss within a pixel). We selected a probability of 1/3, because it led to the most accurate prediction of zeros in our training dataset.

For variable selection with the ZOIB regression model, a jackknifing approach was used, where (1) each explanatory variable was run in a separate model (e.g. covariate equal to one) and (2) the full model was run without that explanatory variable (e.g. total covariates minus one). These two metrics allow one to compare variable

importance and variable redundancy, respectively. Variables were then ordered based on their AIC, Akaike information criterion. Again for pairs of variables which were redundant ( $|r| > 0.95$ ), the variable with the least negative AIC scores based on these two metrics was excluded.

### **2.3.3.3 Accuracy assessments of coarse-scale canopy loss maps**

Model accuracy of the coarse-scale canopy loss maps was computed using two independent testing approaches. The first approach created a testing dataset that was spatially proximate to the training dataset. More specifically 33% of each orthophoto was used as testing data and 66% as training data. The second approach created testing data that was spatially independent of the training dataset. Using leave-one-out cross validation, the model was run 15 times, and for each run a single orthophoto was withheld and used as testing data, while the remaining 14 orthophotos were used as training data. After 15 model runs, each orthophoto had acted as testing data. Model accuracy was computed by averaging the Mean Absolute Error (MAE) and Root Mean Square Error (RMSE) across all 15 runs. These two accuracy assessment approaches for the spatially proximate and spatially independent testing datasets compute model performance both within and out-of-sample, respectively.

## 2.4 Results

### 2.4.1 Accuracy assessments of the fine-scale canopy loss maps

Classifications of NAIP orthophotos were highly correlated with our ground transects for both canopy loss ( $R^2 = 0.90$ , RMSE = 5.4%) and post-drought live canopy cover ( $R^2 = 0.87$ , RMSE = 11%), (Figure 3). As such, these 1-m fine-scale canopy loss maps and live canopy cover maps were used exclusively to calibrate and validate Landsat imagery, when creating regional coarse-scale canopy loss maps.

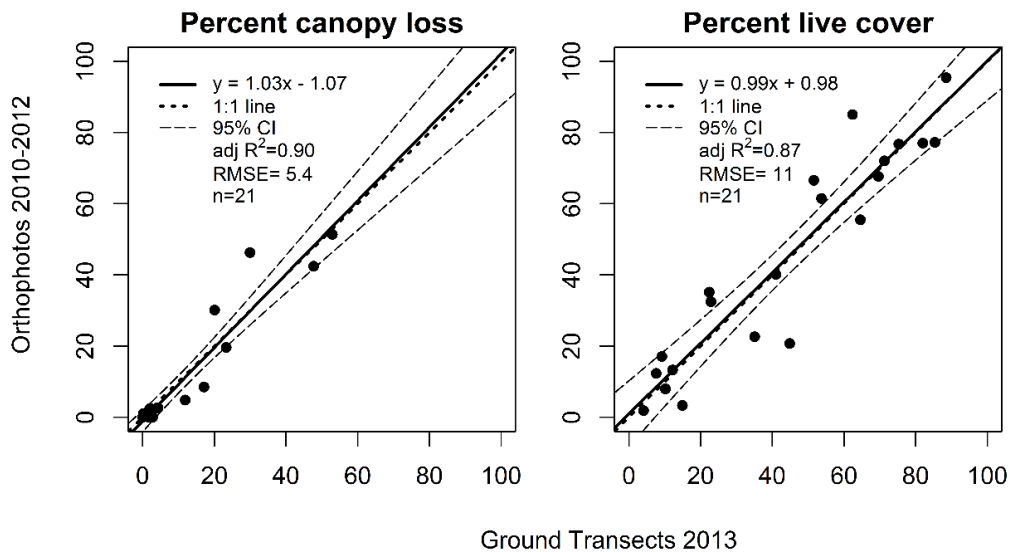


**Figure 3: Percent cover observed in the orthophoto classifications (1 m, spatial resolution) compared to percent cover observed on the ground (21 plots) for percent canopy loss (left) and percent post-drought live cover (right).**

### 2.4.2. Comparison of accuracy among models

The vegetation indices most significant in each model were dependent on the response variables canopy loss and post-drought live canopy (Table 3). In general, for

predicting canopy loss for either model, DVI and the tasseled cap bands were highly significant. For predicting post-drought live canopy NDVI, NBR, and the tasseled cap bands were most significant.

**Table 3: Vegetation indices selected for each model: zero-inflated modeling approach using RF vs. the ZOIB regression model.**

		Random Forest		Zero-inflated beta regression	
	Absence vs. presence of canopy loss	Proportion of canopy loss	Proportion of post-drought live canopy	Probability of zero canopy loss ( $\alpha$ ); proportion canopy loss ( $\mu$ )	Probability of zero; probability of one; proportion post-drought live canopy
	Selected Vegetation Indices (ordered by variable importance)	DVI (13)	RGI (13)	NDVI (13)	DVI (13)
TCG (13)		TCG (13)	NBR (13)	TCG (13)	NBR (13)
RGI (13)		DVI (13)	TCG (13)	TCG (13-09)	TCW (13)
TCB (13)		TCB (13)	TCB (13)	NDWI (13)	TCG (13)
GNDVI (13)		NDWI (13)	TCW (13)	TCW (13-09)	RGI (13)
(B5/B4) (13)		GNDVI (13)	RGI (13)	NDVI (13)	TCB (13)
TCG (13-09)		TCW (13)	DVI (13)	TCB (13-09)	DVI (13)
GNDVI (09)		TCG (13-09)		DVI (09)	
TCW (13)		NDWI (09)		RGI (13)	
TCW (13-09)		GNDVI (09)		TCB (13)	
DVI (09)		TCW (13-09)		TCW (13)	
(B5/B4) (09)		DVI (09)		RGI (09)	
RGI (09)		TCB (13-09)		NDVI (09)	
TCB (13-09)		RGI (09)		NDWI (09)	

13-09 = Difference between 2013 and 2009

The base model, which included only Landsat vegetation indices, was then compared to independent models, each containing one of the six sets of auxiliary variables (Table 4), for both RF and ZOIB. Error rates using the spatially proximate testing dataset were always lower compared to error rates of the spatially independent testing dataset for both RF and ZOIB. Furthermore, the percent difference between the spatially proximate and spatially independent MAE rates in predicting canopy loss were much higher for RF (45%) compared to ZOIB (14%). For predicting canopy loss, when using spatially proximate testing data, RF has the higher accuracy, whereas when using spatially independent data, ZOIB has the higher accuracy. We argue that using spatially independent testing data is the only way to understand how well the model predicts canopy loss outside of where the model was parameterized, and thus ZOIB was selected to predict out-of-sample results.

**Table 4: Model comparison (60 m). Models in bold had decreasing error (MAE or RMSE) compared to the base model. These auxiliary data in bold and variables from the base model were then used in the final models to predict percent canopy loss and post-drought live canopy cover.**

Cover Type	Random forest						Zero-inflated beta regression model					
	Spatially proximate			Spatially independent			Spatially proximate			Spatially independent		
	MAE	RMSE	EV*	MAE	RMSE	EV*	MAE	RMSE	AIC	MAE	RMSE	AIC
<i>Base model: Landsat spectral indices</i>												
CL	3.96	6.10	58.2	5.73	8.66	60.0	4.67	7.16	-118781	5.31	8.09	-167594
A	10.7	13.9	67.3	12.3	15.7	67.7	11.6	14.8	-55189	12.4	15.7	-77586
N	10.5	13.6		12.3	15.5		11.1	14.2		11.7	14.9	
<i>Landsat indices, % forest cover</i>												
CL	3.93	6.06	59.0	<b>5.65</b>	<b>8.55</b>	<b>60.5</b>	4.65	7.14	-119002	5.31	8.12	-167924
A	10.5	13.6	68.7	<b>12.2</b>	<b>15.6</b>	<b>69.1</b>	11.5	14.7	-55889	<b>12.3</b>	<b>15.6</b>	<b>-78508</b>
N	10.2	13.3		11.9	15.1		10.9	14.1		11.5	14.8	
<i>Landsat indices, latitude &amp; longitude</i>												
CL	2.93	4.75	74.1	6.18	9.45	75.2	4.60	7.18	-120188	5.46	8.5	-169776
A	8.77	11.6	77.1	11.7	14.8	77.6	11.4	14.6	-57562	12.3	15.7	-80934
N	8.71	11.5		11.9	15.0		10.7	13.9		11.5	14.8	
<i>Landsat indices, MODIS Land Surface Temperature (LST) difference</i>												
CL	3.59	5.60	64.5	5.76	8.77	66.4	4.57	7.11	-119739	<b>5.25</b>	<b>8.12</b>	<b>-169044</b>
A	9.93	13.0	71.3	12.5	15.8	71.9	11.6	14.8	-55295	12.4	15.7	-77780
N	9.79	12.8		12.2	15.5		11.0	14.2		11.7	14.9	
<i>Landsat indices, elevation</i>												
CL	3.59	5.62	64.1	6.31	9.61	66.0	4.67	7.16	-118970	5.45	8.3	-167897
A	9.81	12.8	72.4	12.8	16.0	72.9	11.6	14.8	-55913	12.5	15.9	-78648
N	9.68	12.6		12.3	15.5		11.1	14.2		11.9	15.2	
<i>Landsat indices, slope &amp; aspect</i>												
CL	3.90	5.98	60.0	5.84	8.76	61.9	4.66	7.15	-119219	5.34	8.13	-168298
A	10.2	13.2	70.1	<b>12.3</b>	<b>15.6</b>	<b>70.8</b>	11.4	14.5	-57157	12.4	15.7	-80438
N	9.97	13.0		12.1	15.2		10.8	13.9		11.7	14.9	
<i>Landsat indices, magnitude of change according to Landtrends</i>												
CL	4.07	6.08	59.6	<b>5.68</b>	<b>8.57</b>	<b>61.1</b>	4.61	7.09	-119620	<b>5.27</b>	<b>8.06</b>	<b>-168660</b>
A	10.6	13.7	68.0	<b>12.2</b>	<b>15.6</b>	<b>68.4</b>	11.5	14.7	-55899	<b>12.3</b>	<b>15.6</b>	<b>-78631</b>
N	10.4	13.5		12.2	15.4		11.1	14.2		11.8	15.0	

MAE – Mean absolute error; RMSE – Root mean square error

EV – Percent variance explained for the regression model, predicting proportion canopy loss

AIC – Akaike Information Criterion

CL – Canopy Loss; A – alive; N – Non-tree

Moreover, remotely sensed derived variables (e.g. Landsat vegetation indices, percent forest cover, MODIS LST, and the magnitude of change associated with the time-series analysis) in general were more likely to improve or maintain model accuracy for both the spatially proximate and spatially independent testing datasets. In contrast, including space and landscape variables (e.g. latitude, longitude, elevation, slope, and aspect), typically decreased the error rate associated with the spatially proximate dataset but increased the error rate when validated with spatially independent testing data. However, this only occurred for models predicting canopy loss. For predicting proportion live canopy in the RF model, including latitude and longitude decreased the MAE and RMSE compared to the base model, when validated with spatially independent testing data. Furthermore, including slope and aspect slightly decreased the RMSE, and maintained the same MAE.

Final models were selected using only those explanatory variables that decreased either the MAE or RMSE, according to the spatially independent testing dataset (Table 5). Although including latitude and longitude decreased MAE for live canopy, the ranges of these variables in the training dataset were not adequately represented across the entire study area (Table 2), and therefore they were not included as covariates in the final model. The ZOIB final model had the lower error rate in predicting canopy loss (MAE = 5.16%) compared to the zero-inflated modelling approach using RF (MAE = 5.60%). Also, the ZOIB final model was capable of predicting a greater proportion of

true zeros and the full range of canopy loss, compared to the RF model. Conversely, the RF model had a slightly lower but similar error rate in predicting percent live canopy cover (MAE = 12.1%) compared to the ZOIB model (MAE =12.3%). The focus of this study was to model proportion canopy loss, and as such we elected to use the ZOIB model to predict both canopy loss and post-drought live canopy cover. We also compared speed and memory requirements of both models in predicting canopy loss using variables from the base model. The ZOIB regression model was ~20 times faster than the RF model, and required ~5 times less memory.

**Table 5: Spatially independent error rates for final canopy models comparing RF and ZOIB**

<b>Model: explanatory variables</b>	<b>Cover type</b>	<b>Observed average value, range</b>	<b>Predicted average value, range</b>	<b>Predicted # of zeros/ observed<sup>1</sup></b>	<b>MAE</b>	<b>RMSE</b>	<b>ME</b>
<i>Zero-inflated beta regression</i>							
Landsat indices; land surface temperature; magnitude of change	Canopy loss	(5.96%, 0-87.6%)	(5.83%, 0-91.9%)	4583/ 14582	5.16%	8.01%	+0.14%
Landsat indices; % forest cover; magnitude of change	Alive	(41.9%, 0-100%)	(41.9%, 0-100%)	-	12.3%	15.5%	- 0.083%
<i>Random forest</i>							
Landsat indices; % forest cover; magnitude of change	Canopy loss	(5.96%, 0-87.6%)	(6.23%, 0-44.5%)	1929 /14582	5.60%	8.48%	-0.26%
Landsat indices; % forest cover; slope & aspect; magnitude of change	Alive	(41.9%, 0-100%)	(41.9%, 3.48%- 98.4%)	-	12.1%	15.3%	- 0.070%

ME = mean error

<sup>1</sup>The proportion of zeros in the dataset is 19%.

We also examined the distribution of post-drought live canopy and canopy loss across a canopy density gradient (pre-drought), using data from the spatially independent testing dataset. Areas with either sparse canopy or closed canopy had less canopy loss compared to intermediate-cover areas (Figure 4).

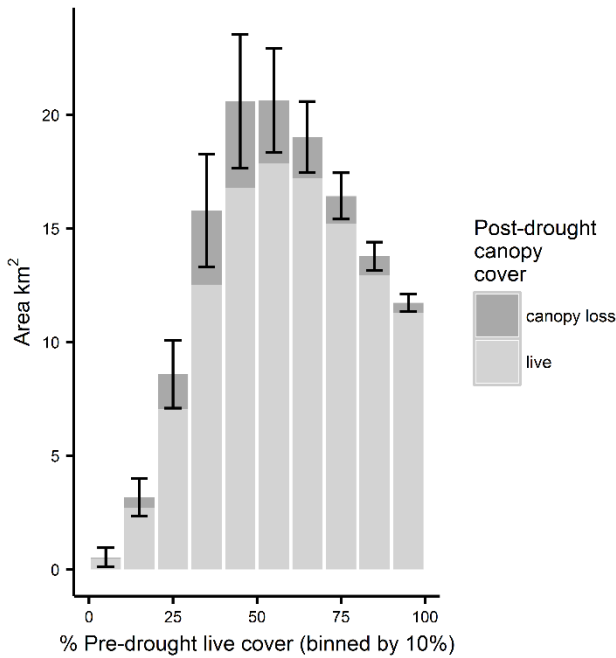


**Figure 4: Distribution of live canopy and canopy loss across a gradient of pre-drought live canopy, from sparse to closed canopy woodlands, using data from the orthophotos. Error bars represent MAE (km<sup>2</sup>) for the canopy loss in scaling up to a 60-m grid cell.**

### 2.4.3 Canopy loss estimated across the study area

The ZOIB regression model was used to predict post-drought live canopy cover and canopy loss using all 15 orthophotos as training data (Fig. 5). We observed an average of 4.7% canopy cover loss across all forested pixels, which is equivalent to 1,124

km<sup>2</sup> of canopy loss in our central Texas study region of ~10,850 km<sup>2</sup> of pre-drought canopy cover. Given that each pixel is not fully forested, this represents 10% loss of forested area. Predicted forest cover loss ranged from 0 to 100%.

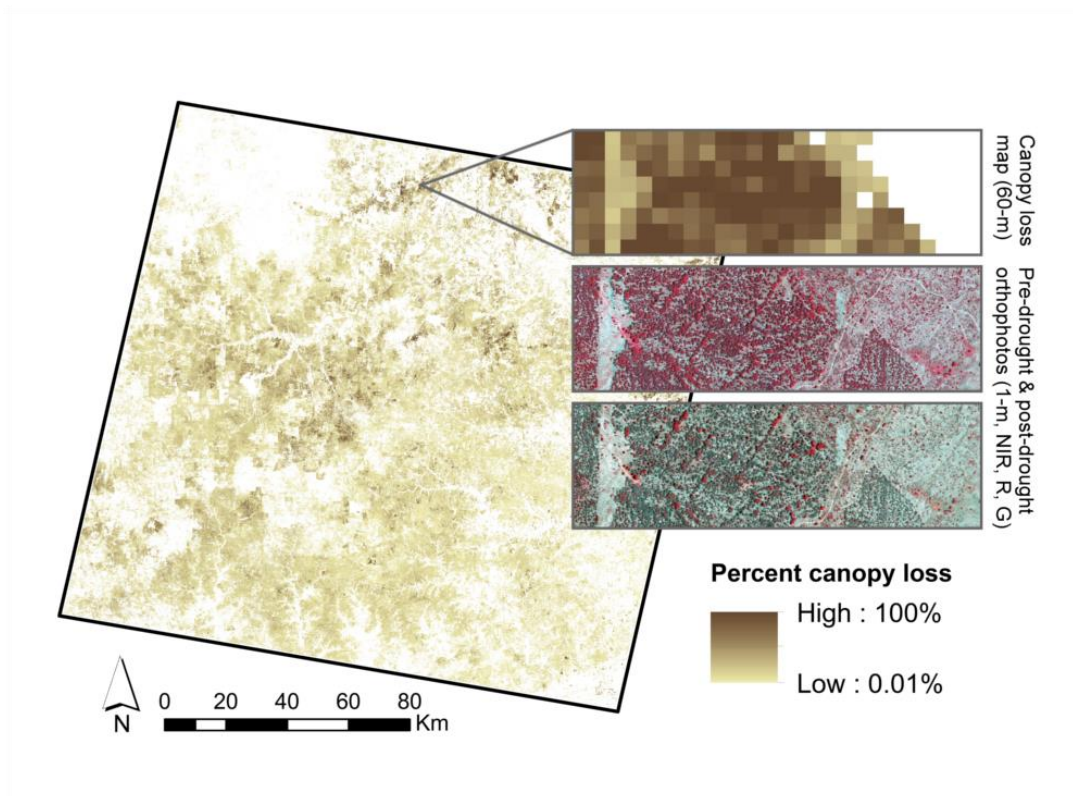


**Figure 5: Coarse-scale continuous canopy loss (60-m), quantified across the study area (Landsat scene path 28/row 39) in the Llano uplift & Edwards plateau region of central Texas. The insets of the orthophotos are false color composite images (NIR, R, G).**

## **2.5 Discussion**

We developed an approach capable of mapping drought-induced canopy loss at a regional scale that relied on high and moderate resolution remotely sensed data to create continuous canopy loss maps. Our approach works well in open canopy forests,

where it is inherently more difficult to detect canopy loss, because the changes in forest cover are more subtle than in fully forested areas. As such, our dataset is composed of zero-inflated continuous proportions and we present two models capable of handling this type of data: (1) RF and (2) ZOIB.

We found the ZOIB regression model to be more robust and less computationally demanding in predicting percent tree canopy cover loss compared to RF. ZOIB had a lower error rate and was also 20 times faster, with a much lower memory requirement. When models are run using zero-inflated data, the predicted results are typically biased in two ways: (1) for areas with a zero observation, the model fails to predict the zero correctly, and instead predicts very low values, and (2) where a non-zero observation occurs, the model underestimates the value (Savage et al., 2015). The ZOIB regression model was less biased, in comparison to the zero inflated RF approach, because it predicted a greater proportion of zeros, where there were actual zeros, and the full range of canopy cover loss, where non-zero observations occurred.

The design of the training and testing datasets significantly influenced the accuracy measures. We found that it was important to validate the model with spatially independent testing data. Spatially proximate testing data would be expected to produce the highest accuracy measures as we see here, yet when the goal is to predict in new areas outside the immediate validation area, the use of spatially independent testing data is the better true assessment of model/mapping performance (González-

Roglich & Swenson, 2016). Furthermore, if we had only validated using spatially proximate testing data, then we would have selected the RF model as having greater accuracy. However the RF model had lower accuracy in predicting canopy loss in new areas. Therefore, during model selection, it is necessary to test models with spatially independent testing data to achieve a valid estimate of the models' power to predict out-of-sample. Assessing models with spatially proximate testing data is appropriate in cases when the model is not extended to new locations.

Variable selection was also influenced by the design of the testing and training datasets. Including topographic variables (elevation, slope, and aspect) resulted in lower error rates when using spatially proximate testing data, but higher error rates when using spatially independent testing data for modeling canopy loss. Again if we had only validated with spatially proximate testing data, then the model would have included variables that would have decreased the models ability to predict in new areas. In general, including only remotely sensed variables led to a better predictive model for canopy loss. Conversely, for the RF model when predicting proportion live canopy, space and landscape variables had mixed effects, maintaining a similar, but slightly lower error rate for slope and aspect, decreasing the error rate for latitude and longitude, or increasing the error rate for elevation, when validated with spatially independent testing data. It is interesting that latitude and longitude played an

important role in predicting percent live cover in this region, likely due to the strong east-west precipitation gradient that exists in Texas.

Studies of forest disturbance typically take place in areas where pixels are almost entirely forested. However, climate models predict that subtropical dry zones will become even drier as climate change advances (Seager et al., 2010), and these areas are often dominated by shrublands, woodlands, and savannas, which are typically open-canopy systems. Detecting mortality in these systems is a key area that merits further exploration. It is challenging to map mortality for mixed and sparsely forested pixels (compared to closed-canopy forests); however, our method of defining percent canopy loss within a pixel quantifies mortality more accurately than methods that label entire pixels as mortality. In these open canopy ecosystems, the vegetation in a 60-m grid cell is rarely completely dead, let alone entirely forested.

Drought-induced tree mortality is a subtle land cover change; however it is also widespread and can cause substantial changes in forest cover over large regions. Using the ZOIB regression model, we found an average of 4.7% canopy loss (e.g. ~10% loss of forested area). Most of this mortality occurred in areas of medium canopy cover, compared to areas with sparse or closed-canopy (Figure 4). Spatial patterns of drought-induced tree mortality are often complex, due to interactions between multiple controlling factors (C. D. Allen et al., 2010). For example, sites with high tree density are often more prone to density-dependent mortality (Fensham, Fairfax, & Ward, 2009), due

to competition for limited water resources during a drought. However, sites with high tree density and adequate moisture can be favorable for tree growth, relative to dry landscape positions having less dense vegetation. Perhaps there is a trade-off between density-dependent factors and landscape position that could explain why tree mortality in our study region is predominantly occurring in areas with medium levels of canopy cover.

In the orthophoto classifications, the fine-scale 1-m spatial resolution allowed for the delineation of thinning/barely alive canopy and actual canopy loss. However, in scaling up to Landsat, perhaps some of the canopy loss, which we assume is due to mortality of trees, may in fact be due to canopy thinning. This could account for some of the error observed between the coarse-scale canopy loss maps created using Landsat and the fine-scale canopy loss maps created using the orthophotos.

To avoid quantifying canopy loss due to fire, we removed all areas that were burned; however, other disturbances, particularly due to insects and pathogens, could have also contributed to the canopy loss observed. Canopy loss occurred throughout the study area without definitive epi-centers inherent in most insect and disease outbreaks; therefore we assume that much of this mortality was due to drought. Nonetheless, drought-stressed oaks are more susceptible to *Hypoxylon* canker, which can occur in a latent state in healthy oaks. This may explain why disease incidence can increase rapidly following drought-stress (Bassett & Fenn, 1984). Also, oak trees already infected with

oak wilt (*Ceratocystis fagacearum*) typically have weakened vascular systems, and, as such, drought can exacerbate the disease (A. D. Wilson, 2001). Therefore, drought likely increased the susceptibility and/or accelerated the mortality risk of trees infected by insects and/or pathogens, and as such we still consider drought as a factor in killing these infected trees.

In the next chapter, we extended this analysis and created canopy cover loss maps across the entire state of Texas. Texas has a significant east-west precipitation gradient and, thus, a diverse range of natural systems. Canopy loss maps across Texas will provide valuable information on how trees respond to drought stress across this large climatic gradient.

### **3. Measuring canopy loss and climatic thresholds from an extreme drought along a 5-fold precipitation gradient across Texas**

#### ***3.1 Introduction***

As climate change progresses, droughts in many areas are expected to increase in severity, duration, and frequency and, as a result, forests will likely become more vulnerable to drought-induced tree mortality (C. D. Allen et al., 2015). Already, tree mortality events have been observed across the globe (C. D. Allen et al., 2010), ranging from increases in background mortality rates (van Mantgem et al., 2009) to regional die-offs (Breshears et al., 2005). As temperature extremes become more common under climate change, the likelihood of droughts occurring simultaneously with heatwaves is increasing (AghaKouchak et al., 2014). These 'hotter droughts' can be particularly destructive to forests by increasing respiration and, in consequence, the potential for carbon starvation; increasing water stress due to rising atmospheric moisture demand could also result in hydraulic failure (C. D. Allen et al., 2015). Increased tree mortality will affect many critical factors, including impacts to community composition (Mueller et al., 2005), food webs (Carnicer et al., 2011), biophysics (Robert B Jackson et al., 2008; Rotenberg & Yakir, 2010), carbon cycling (Ciais et al., 2005; Michaelian et al., 2011), ecohydrology (H. D. Adams et al., 2012), stream flow (Guardiola-Claramonte et al., 2011), and phenology (Ivits et al., 2014).

To improve forecasts of how forests will respond to climate change, quantitative relationships between tree mortality and climate are needed, even if these relationships are empirical (H. D. Adams et al., 2013). Until the mechanisms surrounding tree death are well understood and enough data exist to parameterize global vegetation models, empirical relationships may represent the most appropriate avenue for forecasting tree mortality (H. D. Adams et al., 2013). Tree mortality is often linked to reduced precipitation, increased temperature, and associated increased vapor pressure deficit (VPD) (C. D. Allen et al., 2015). VPD is defined as the difference between saturated vapor pressure and actual vapor pressure and is largely dependent on temperature. Other drought indices have been proposed that incorporate both precipitation and temperature. For example, the difference between precipitation and potential evapotranspiration,  $P - PET$ , accounts for both supply and atmospheric moisture demand (Rind, Goldberg, Hansen, Rosenzweig, & Ruedy, 1990). A water deficit occurs on the landscape when precipitation is less than potential evapotranspiration and  $P - PET$  is negative. Furthermore, tree mortality often has a threshold response with climate (Clifford et al., 2013). Once a specific climatic anomaly is surpassed, the likelihood of tree mortality increases substantially.

Many studies have linked mortality events to climatic anomalies. These studies include tree-ring analysis to develop a forest drought stress index in the southwest United States (Williams et al., 2013) as well as field surveys in Amazonia and Borneo

(Phillips et al., 2010) and in Australia (Mitchell et al., 2014). However, fewer studies have examined relationships between remotely sensed observations of tree mortality across climatic gradients. For example, precipitation and VPD thresholds were related to pinyon pine (*Pinus edulis*) mortality for a sub region of New Mexico (Clifford et al., 2013), and climatic water deficit was linked to aspen (*Populus tremuloides*) mortality in a part of Colorado (Anderegg et al., 2015). Such studies focused on one natural system with only a couple of dominant tree species. In this study we examine remotely sensed observations of tree mortality across a much larger climatic gradient from humid to semi-arid regions. Through remote sensing, climate can be linked to continuous spatially explicit estimates of tree mortality across large areas, closer to the extent of regional vegetation models.

Remote sensing approaches tailored specifically for drought-induced tree mortality that can span large areas at a fine resolution are also needed. Tree mortality caused by drought is often an irregular process by which some individuals die but neighboring trees remain alive. Dead trees scattered among many live trees are more difficult to quantify using remote sensing approaches compared to disturbances that kill entire stands (McDowell et al., 2015). At coarser scales pixels are often 'mixed', containing multiple cover types (i.e., canopy loss and live canopy) and there may be excess zero pixels (i.e., homogenous live canopy cover), if low-levels of mortality occur. Many remote sensing techniques have been proposed to quantify drought-induced tree

mortality, including spectral mixture analysis (Huang & Anderegg, 2012), zero-inflated models (Schwantes, Swenson, & Jackson, 2016), and time-series of spectral indices (Meddens et al., 2013; Vogelmann et al., 2009). However, these studies were designed for mapping mortality in only one natural system with a few dominant species. Other studies have proposed techniques that work across systems using Moderate Resolution Imaging Spectroradiometer (MODIS), such as the MODIS global disturbance index (Mildrexler, Zhao, & Running, 2009) and the ForWarn system (Norman, Koch, & Hargrove, 2016). However, the spatial resolution of these products ranges from 250 m to 1 km, which is too coarse to capture local-scale disturbances (McDowell et al., 2015). Alternatively, the 30-m resolution of Landsat imagery is a more appropriate scale to detect forest cover changes (Cohen & Goward, 2004). In this study, we implement a remote sensing approach that (1) maps canopy loss across diverse ecoregions at regional scales and (2) accommodates excess zeros and mixed pixels, inherent to disturbances like drought-induced tree mortality.

Texas was advantageous for studying drought-induced tree mortality because it was the location of an extreme drought and heat wave in 2011 and it spans a large climatic gradient from humid to semi-arid regions. Using statewide averages of Palmer Drought Severity Index (PDSI) data from 1895-2011, Hoerling et al. (2013) found that the 2011 drought reached a record statewide minimum PDSI of -7.93. The 2011 drought was also the driest 12-month period, October 2010 to September 2011, on record (Hoerling et

al., 2013). Furthermore, due to low atmospheric moisture and high temperatures, the 2011 drought was also associated with a record-high VPD (Williams et al., 2014). Although it is challenging to definitively link episodic climatic events to climate change, models indicate that abnormally high summer temperatures in Texas are increasing in likelihood (Rupp et al., 2015). Furthermore, in the southwestern United States, temperature and VPD are projected to increase in the future (Williams et al., 2014). Texas has over 200 ecological plant community types dominated by woody species (Elliott et al., 2014), spanning a broad range of annual precipitation regimes from humid to semi-arid. As such, Texas contains the most arid edge of many species' ranges (e.g., the eastern hardwoods). These trailing range edges often see heightened drought-induced tree mortality (Jump et al., 2009).

In this study, we identify empirical relationships between climate and canopy loss observed during and after the drought and determine if, and when, the 2011 climatic anomalies are projected to be crossed in the future. To detect canopy loss from the 2011 drought across Texas, we first created a multi-temporal training dataset by classifying 194 fine-scale 1-m orthophoto sets (Schwantes et al., 2016). We then used random forests models to relate the canopy loss observed in the 1-m orthophoto classifications to 30-m Landsat imagery to estimate drought impact across the state of Texas. These coarse-scale regional maps were used to identify ecological systems most impacted by the drought. We also identified threshold relationships between climate

and spatial patterns of canopy loss across the 5-fold precipitation gradient spanning humid to semi-arid regions. Lastly, we examined whether the 2011 climate anomalies would likely be surpassed in the future using downscaled projected climate data, under representative concentration pathway, RCP, 4.5 and 8.5 trajectories.

## **3.2 Materials and Methods**

### **3.2.1 Study area**

The state of Texas was selected because (1) it was the center of a major drought and tree mortality event in 2011, (2) its natural precipitation gradient was large for areas dominated by tree cover, extending from mean annual precipitation (MAP) of ~1500 mm in the east to ~300 mm in the west, and (3) it included the edges of many species' ranges (e.g., eastern hardwoods such as *Quercus stellata* and many western shrubland species like *Juniperus ashei*). The 12 U.S. EPA level III ecoregions in the state of Texas followed the east-west precipitation gradient, transitioning from dense closed-canopy forests to the open-canopy savannas to the western shrublands (Table 6). We excluded the high plains in this study, because the area was dominated by grasslands, with little or no woody plant cover. We divided our study area into six zones for purposes of modeling by combining the 11 ecoregions into zones based on similar species and climate: (1) Pineywoods, (2) Oakwoods/Blackland Prairies, (3) Rolling Plains, (4) Edwards Plateau, (5) South Texas, and (6) Trans Pecos (Figure 6, Table 6). A decrease in precipitation and an increase in mean temperature compared to historical averages was observed during

the 2011 drought across all six modeling zones (Table 6; PRISM Climate Group, 2015). Moreover, precipitation decreased by more than half of the historical average for the Trans Pecos and Edwards Plateau.

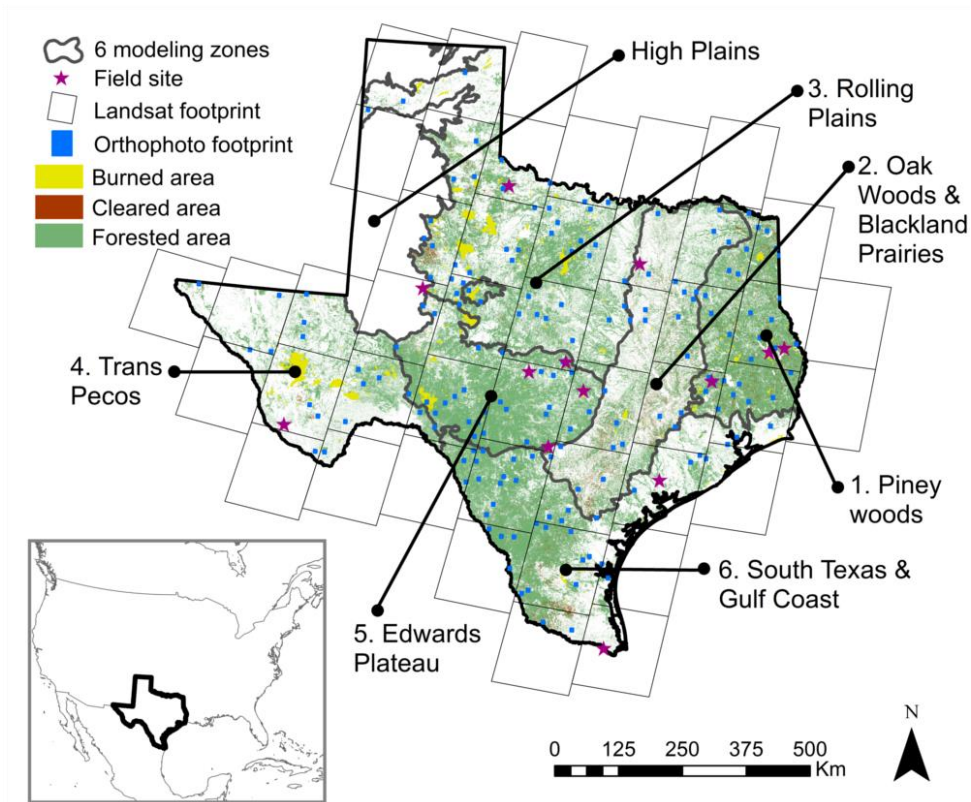


**Figure 6: Modeling zones of Texas characterized as temperate deciduous forest, grassland, and desert biomes. The High Plains, non-forested, burned and cleared areas were excluded from the analysis. We estimated canopy loss across three scales: field estimates of canopy loss (67 plots) were used to validate the fine-scale canopy loss maps derived from 1-m orthophotos (n =194 at ~41 km<sup>2</sup> each), which were used to scale up to Landsat (46 footprints covering Texas, ~600,000 km<sup>2</sup>).**

**Table 6: Climate data (historical averages and 2011 values) for the six modeling zones**

Modeling zone	Level III ecoregions (U.S. EPA)	Spatial mean of annual precipitation (mm)		Spatial mean of warm season mean temp (°C)	
		Hist. mean ± SD <sup>1</sup>	2011 mean	Hist. mean ± SD <sup>1</sup>	2011 mean
1. Pineywoods	• South Central Plains	1222 ± 228	826	25.9 ± 0.7	28.1
2. Oakwoods & Blackland Prairies	• Texas Blackland Prairies • East Central Texas Plains	948 ± 195	608	26.6 ± 0.7	28.6
3. Rolling Plains	• Southwestern Tablelands • Central Great Plains	646 ± 124	380	25.5 ± 0.8	28.0
4. Trans Pecos	• Cross Timbers • Arizona/ New Mexico Mountains • Chihuahuan Deserts	317 ± 100	110	25.0 ± 0.7	27.1
5. Edwards Plateau	• Edwards Plateau	614 ± 150	295	25.7 ± 0.7	27.7
6. South Texas & Gulf Coast	• Southern Texas Plains • Western Gulf Coastal Plain	767 ± 172	384	27.9 ± 0.6	29.3

<sup>1</sup> The historical mean and standard deviation as calculated for years 1950 to 2005, using PRISM data (PRISM Climate Group, 2015).

### 3.2.2 Creating training and testing data: classification and field validation of 1-m canopy loss maps

Following Schwantes et al. (2016), we created a training and testing dataset of fine-scale canopy loss maps, from supervised classifications of stacks of pre-drought (2010) and post-drought (2012) orthophotos from the National Agriculture Imagery

Program (NAIP) (US Department of Agriculture, 2014). The 1-m orthophotos (four bands: red, green, blue, near-infrared, NIR) were flown during the growing season, were already orthorectified to true ground, errors within 6 m, and were tiled based on quarter quads, each ~41 km<sup>2</sup>. We randomly selected 186 NAIP quarter quads using a blocked random sample, where blocks were the Landsat footprints (each ~23,000 km<sup>2</sup>), excluding areas of overlapping Landsat scenes. The number of NAIP quarter quads chosen per Landsat footprint was weighted by the forest-area proportion in the Landsat footprint. We selected an additional eight orthophotos non-randomly based on access to public land, for the purpose of field validation; field access was limited in Texas.

For validation, we compared observations of canopy loss in the 1-m orthophoto classifications to measurements of dead and live crowns taken on the ground, following Schwantes et al. (2016). From July – Sept 2013 and during July 2014, we measured dead and live crowns in 13 sites (Figure 6), with 3-7 plots per site (Table 15, appendix B), for a total of 67 plots. For each plot, we measured dead and live crowns (to the nearest 0.1-m) along four 25-m transects running from the randomized plot center to the plot edge following the four cardinal directions. All woody species >1-m in height were counted that intersected the transect. Rules for assigning the health status to each individual tree (e.g., dead, live, dead prior to drought) were outlined in Table 16, appendix B. Canopy cover loss measurements of the uppermost layer of canopy, from each of the four transects, were summed for each plot, and compared to the total canopy loss observed in

the orthophoto classifications, as estimated within a 25-m radius circular buffer from plot center. Further details on classification and validation of the orthophotos are described in Schwantes et al. (2016) and the supporting information.

### **3.2.3 Scaling up to regional estimates using random forests: 30-m binary canopy loss map**

To focus our analysis within forested regions and avoid misclassifications associated with fires and clearing, we excluded areas that were non-forest, burned, or cleared. We created a binary forest cover mask by including only ecological systems dominated by tree species (Elliott et al., 2014). Using data from the Monitoring Trends in Burn Severity project (USDA Forest Service/U.S. Geological Survey, 2014), we also excluded all areas that were burned from May 2009 to Oct 2014. Lastly, through visual inspection we used a band difference between post-drought and pre-drought tassel cap brightness bands (Baig et al., 2014; Crist, 1985) of 0.1 to remove trees that were cleared in the Pinewoods and Oakwoods/Blackland Prairies and 0.2 for the four remaining western modeling zones.

Atmospherically corrected imagery from the Landsat surface reflectance product (Masek et al., 2006) was acquired from May-Oct with a preference for late summer images. Pre-drought images were either taken in 2009 or 2010 from the Landsat 5 TM archive. Landsat 5 TM became nonoperational Nov 2011, and Landsat 8 OLI, launched Feb 2013; therefore post-drought images were from the Landsat 8 OLI archive, 2-3 years after the drought (2013 or 2014; see Table 17, appendix B, for acquisition dates). We

manually co-registered NAIP images that showed poor alignment with Landsat scenes to achieve an RMSE  $< 0.5$  of a 30-m Landsat pixel.

To scale up from the 1-m orthophoto classifications to the 30-m Landsat imagery, we used random forests models (Breiman, 2001; Liaw & Wiener, 2002) in classification mode to create 30-m binary maps (loss or no loss) across Texas. Using a separate model for each of the six modeling zones, we employed random forests, a machine learning algorithm that created an ensemble of decision trees. Each decision tree was grown using a sample of the data and a subset of the explanatory variables. The nodes on each decision tree were created by splitting the explanatory variables in a way that created the most homogenous groups, until a minimum/terminal node size was reached. Bootstrap samples were taken with replacement to build each decision tree; data withheld were used to compute the out-of-bag (OOB) error rate (Breiman, 2001). We did not find that our models were sensitive to parameterization; therefore, we used the following: 1001 decision trees, a node size of 1, and the number of variables used to build each decision tree equal to the square root of the total number of variables. By overlaying a grid at the spatial resolution of Landsat (30-m) onto the 1-m orthophoto classifications, we extracted proportion canopy loss for each 30-m grid cell and created a binary response variable for the random forests models: (1) pixels with zero canopy loss (no loss pixels with homogenous live canopy) and (2) pixels with greater than 25% canopy loss (loss pixels). The explanatory variables for the random forests models were

percent tree cover from the National Land Cover Databases (NLCD) (Homer et al., 2015) and 13 vegetation indices derived from Landsat (Table 7) for both pre- and post-drought images. For variable selection, we created parsimonious models by removing variables that were highly correlated to greater than  $|0.95|$ . The final variables selected for each random forests model can be found in Table 18, appendix B.

**Table 7: Landsat vegetation indices and auxiliary explanatory variables considered in random forests models.**

	Covariate	Citation
1	Difference vegetation index (DVI)	(Tucker, 1979)
2	Greenness normalized difference vegetation index (GNDVI)	(Gitelson et al., 1996)
3	Modified soil adjusted vegetation index (MSAVI)	(Qi, Chehbouni, Huete, Kerr, & Sorooshian, 1994)
4,5	Normalized burn ratio (NBR) Normalized burn ratio II (NBR2)	(van Wagtenonk et al., 2004)
6	Normalized difference water index (NDWI)	(E. H. Wilson & Sader, 2002)
7	Normalized difference vegetation index (NDVI)	(Tucker, 1979)
8	Ratio SWIR/NIR	(Vogelmann & Rock, 1988)
9	Red green index (RGI)	(Coops et al., 2006)
10	Soil adjusted vegetation index (SAVI)	(Huete, 1988)
11,12,13	Tasseled cap brightness (TCB), greenness (TCG), wetness (TCW)	(Baig et al., 2014; Crist, 1985)
14	Percent tree cover (% tree)	(Homer et al., 2015)

Much of the landscape experienced no mortality; thus, the canopy loss dataset contained many more pixels with zero canopy loss compared to pixels with greater than 25% canopy loss, and therefore, to improve the random forests model fits we made the following modifications. Firstly, we sampled each class equally for each decision tree in the random forests. Secondly, using random forests model outputs of the probability of

a pixel's class membership, we tuned the models with receiver operating characteristic (ROC) curves (Sing, Sander, Beerenwinkel, & Lengauer, 2005). To determine the class of each pixel (e.g., canopy loss vs. no loss), we balanced true positive rate (TPR, accurately predicting a loss pixel when a loss pixel occurred) and true negative rate (TNR, accurately predicting a no loss pixel when no loss pixel occurred). Finally, to remove the influence of slight atmospheric differences between Landsat scenes, the random forests model was first run using all data within the modeling zone. Then, unique probability thresholds were chosen using the ROC analysis based on groups of Landsat footprints. Groups were chosen to match rows with similar acquisition dates or for individual Landsat scenes that had unique acquisition dates. The cutoff values used to define a loss pixel from a no loss pixel can be found in Table 19, appendix B and a more detailed explanation of the ROC analysis can also be found in appendix B.

Not every pixel contained 100% canopy loss, and therefore to estimate the overall percent canopy loss, we multiplied the proportion of impacted 30-m pixels by the average canopy loss within each of the impacted pixels, as estimated using the 1-m orthophoto classifications for each modeling zone. We used the same procedure to compute overall relative canopy loss, defined as canopy loss divided by the live pre-drought canopy cover. In this way we could more precisely determine the percent of forest impacted by the drought. To test model performance, we used spatially independent testing data, which provided a better estimate of the true mapping

accuracy (González-Roglich & Swenson, 2016; Schwantes et al., 2016), by conducting leave-one-out cross validation for each orthophoto, independently for each of the six modeling zones (see supporting information for a complete description). As is the case for most remote sensing studies, we were only mapping aerial cover, defined as the uppermost layer of canopy (Fehmi, 2010); we were not mapping overlapping canopy cover. For example, if the overstory died and the midstory or understory remained alive, we would still consider this canopy loss. Moreover, analysis relying on remotely sensed imagery detect changes in canopy; therefore, we used the terms canopy loss and live canopy instead of dead and live trees. Image processing for the coarse-scale maps was completed in ENVI/IDL 5.0, ArcMap 10.3.1, Python 2.7.8, and R v. 3.1.3 (R Core Team, 2015).

#### **3.2.4. Defining relationships between spatial patterns of canopy loss and climate**

To examine how climate drove the spatial patterning of canopy loss across a landscape, we used 4-km spatially interpolated climate data from PRISM (PRISM Climate Group, 2015). First, for each 4-km cell we calculated the relative canopy loss, defined as the number of 30-m drought impacted pixels divided by the number of forest cover pixels. We then examined how four climate variables: annual precipitation, warm-season (May-Sept) mean temperature, warm-season VPD, and annual 2011 P-PET controlled mortality patterns across an east-west transect that was 100 km wide by ~1000 km in length. In selecting the transect, we chose the widest horizontal swath across

Texas that encompassed the greatest amount of ecosystem diversity. As the transect spans a precipitation gradient, we calculated percent deviations from historical values for precipitation; however, for temperature and VPD we calculated anomalies, and for P-PET we used the 2011 value. The analysis was conducted on a sample of 20% of the 4-km pixels within the transect, excluding adjacent pixels with a minimum distance between cell centers of < 8 km. We also only included pixels with >50% forested area to focus the analysis in predominantly forested regions. Precipitation and mean temperature were directly acquired (PRISM Climate Group, 2015), and daily VPD was calculated using mean temperature and dew point temperature following Daly, Smith, & Olson, (2015). PET was acquired from GRIDMET, a 4-km gridded climate dataset, where PET was calculated using Penman-Monteith (Abatzoglou, 2013).

We identified climatic thresholds that when surpassed were associated with greater canopy loss, based on the first split in regression trees (Therneau, Atkinson, & Ripley, 2015). In this case, the numeric response variable was relative canopy loss within a 4-km pixel and the continuous explanatory variable was percent deviation or anomaly from normal climate. For each climate variable, the regression tree selected a breakpoint along the continuous climate variable that created the most homogenous response group (De'ath & Fabricius, 2000). In this way, climatic conditions associated with large amounts of canopy loss were differentiated from climates associated with little canopy loss. The breakpoint between these two groups was considered the climatic threshold

that when crossed led to enhanced mortality. These climatic thresholds were identified across space; therefore, to further validate whether these thresholds could also hold true through time, we examined past climate from 1950 to 2015, using data from PRISM (PRISM Climate Group, 2015); however, PET data were only available from 1979 onwards (Abatzoglou, 2013).

### **3.2.5 Projecting whether 2011 climate anomalies were likely to be crossed in the future**

We determined whether the climate thresholds associated with canopy loss in 2011 were likely to be crossed in the future. First we acquired 4-km projected climate data, where statistical downscaling had been performed using the Multivariate Adapted Constructed Analogs (MACA) approach (Abatzoglou & Brown, 2012). Precipitation, temperature, and PET were acquired directly (Abatzoglou & Brown, 2012), whereas daily VPD was computed using mean temperature and specific humidity (Ross & Elliot, 1996). We examined the mean, standard deviation, and range of 20 general circulation models (GCMs), using Coupled Model Intercomparison Project Phase 5 (CMIP5) results, under the Representative Concentration Pathway (RCP) 4.5 and 8.5 trajectories from 2006 to 2099 (Abatzoglou & Brown, 2012). Then to calculate historical values used to compute the anomalies from current climate, we used historical PRISM data (1950-2005); however, for calculating the historical values used to compute anomalies for future climate, we used historical projected MACA data (1950-2005). We only considered pixels with >50% forested area. Also, to further characterize the variability between the models,

we estimated the percent of times that these climatic thresholds would be crossed over the latter half of the 21<sup>st</sup> century (2050-2099) across the 20 GCMs, creating spatially explicit maps for the state of Texas. For example, if 50% of the GCMs predicted that a threshold crossing would occur for 50% of the years from 2050-2099, then this would be represented by an average 25% times crossed.

### **3.2.6 Identifying ecological systems most impacted by the 2011 drought**

We determined which communities were most influenced by the 2011 drought through an overlay of our canopy loss maps and an ecological systems layer map (Comer et al., 2003; Elliott et al., 2014). We only considered ecological systems dominated by tree species, 231 systems, and then we further only included geographically dominant systems that covered at least 200 km<sup>2</sup>, for a total of 94 systems. Of these 94 dominant systems, we present the top 10 most and least impacted, where the most impacted systems had the largest relative canopy loss defined as drought-impacted area divided by total area. The full analysis for all 231 tree-dominant systems can be found in Table 20, appendix B.

## **3.3 Results**

Ground estimates of canopy loss and post-drought live canopy cover were both highly correlated with the same attributes observed in the orthophoto classifications ( $R^2 = 0.82$ , RMSE = 4.7% for canopy loss;  $R^2 = 0.89$  and RMSE = 11% for live canopy) (Figure 7). Overestimation of canopy cover loss in the orthophotos happened occasionally when

trees lost most of their foliage and thus appeared dead in the orthophotos.

Underestimates of tree cover loss occurred on occasion when dead trees were misclassified as alive, due to the presence of either dense understory shrubs or grass under the dead canopy, or extensive vines within the dead canopy.

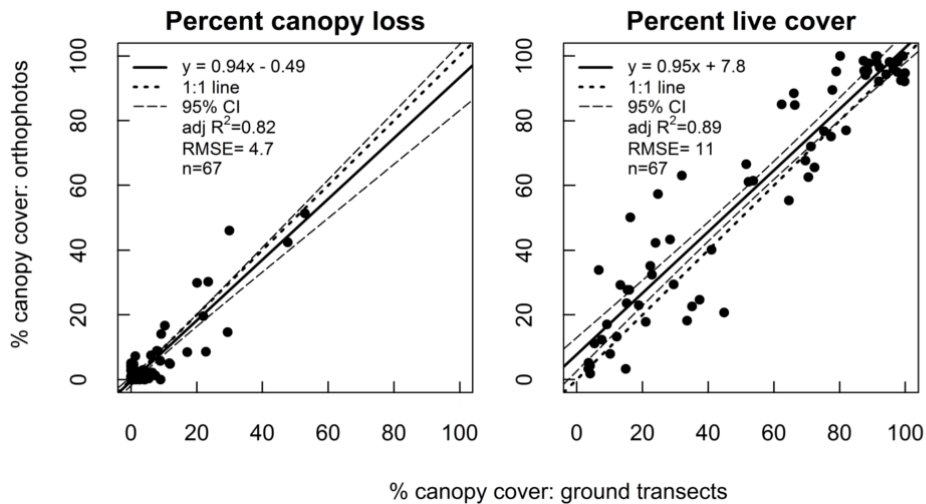


**Figure 7: Field validation: canopy loss and live canopy cover measured using ground transects (2013-2014) compared to canopy loss and live canopy cover observed in the 1-m orthophoto classifications (imagery from 2010 and 2012).**

In quantifying statewide 30-m binary canopy loss using random forests models, error rates and the covariates found to be the most important in predicting canopy loss were unique to each modeling zone. The normalized burn ratio and tassel cap brightness (TCB) indices were found to be the most important to modeling canopy loss in the Pineywoods region, whereas TCB, tassel cap wetness, and the difference vegetation index were the best predictors for the Trans Pecos and Edwards Plateau (Table 18,

appendix B). The out-of-bag (OOB) estimates of accuracy (ranging from 86-93%) were higher compared to the spatially independent estimates (ranging from 79-90%) (Table 8), likely because the latter were tested using spatially independent data. The spatially-independent accuracy metric also reflects that the data had excess zeros, and as such the models tended to predict the common (no loss) pixels well (TNR), but the rarer class (loss pixels) less well (TPR). The model with the highest error was for the South Texas & Gulf Coast modeling zone (Table 8).

**Table 8: Accuracy of random forests models in distinguishing pixels of canopy loss (>25%) from pixels of no (0%) canopy loss.**

Modeling zone	Spatially independent			Final model (OOB)		
	% Accuracy	% TPR	% TNR	% Accuracy	% TPR	% TNR
Pineywoods	90	80	90	91	90	91
Oakwoods & Blackland Prairie	83	61	83	88	87	88
Rolling Plains	79	53	80	86	87	86
Trans Pecos	83	68	83	93	90	93
Edwards Plateau	84	81	85	91	91	91
South Texas & Gulf Coast	79	30	81	92	91	92

*TPR = True Positive Rate (accurately predicting a loss pixel when a loss pixel occurred)*

*TNR = True Negative Rate (accurately predicting a no loss pixel when a no loss pixel occurred)*

Overall, 61,000 km<sup>2</sup> of forested area was impacted by the drought as defined by having >25% canopy loss per pixel (Figure 8, Table 9). Within forested pixels across the state, the drought caused an average 9.5% canopy loss and 15% relative canopy loss, defined as canopy cover loss divided by pre-drought live canopy cover (Table 9). Relative canopy loss was a more useful comparison metric considering that average pre-drought percent live canopy ranged from 21% in the Trans Pecos to 85% in the Pineywoods according to the orthophoto classifications. The Pineywoods region was the least impacted in terms of canopy loss and relative canopy loss. The other five western modeling zones were severely impacted by the drought when considering relative canopy loss.

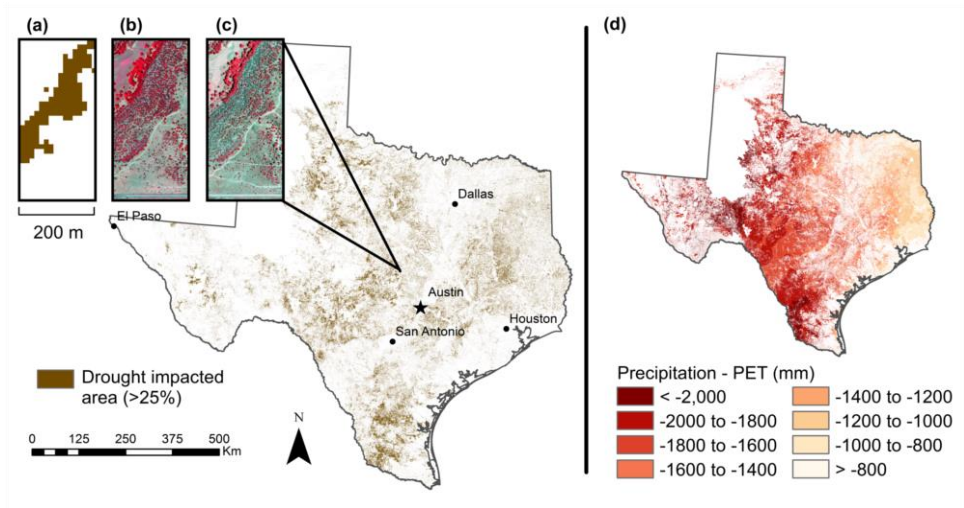


**Figure 8: Drought impacted area (> 25% canopy loss per pixel) across Texas. Insets: an example near Lampasas of (a) 30-m binary canopy loss maps, (b) pre-drought 2010 orthophoto (1-m) and (c) post-drought 2012 orthophoto. On average the 2011 drought caused 9.5% canopy loss (15% relative canopy loss) statewide within all forested pixels. (d) The difference between 2011 annual precipitation and potential evapotranspiration (PET) originally at a 4-km spatial resolution was resampled to 30-m to provide a direct comparison to the 30-m drought-impacted area maps.**

**Table 9 Summary of percent forest cover lost and impacted area by modeling zone**

Modeling zone	Estimated area impacted (km <sup>2</sup> )	Avg. % canopy loss in loss pixels <sup>1</sup>	Avg. relative % canopy loss in loss pixels <sup>2</sup>	Overall avg. % canopy loss <sup>3</sup>	Overall avg. relative % canopy loss
Pineywoods	8,842	35	40	6.8	7.8
Oakwoods & Blackland Prairie	8,818	36	43	9.8	12
Rolling Plains	15,760	36	60	9.9	16
Trans Pecos	3,865	42	73	7.9	14
Edwards Plateau	11,522	39	65	8.8	15
South Texas & Gulf Coast	12,157	46	68	10	16
<b>Total</b>	<b>60,969</b>	<b>41</b>	<b>63</b>	<b>9.5</b>	<b>15</b>

<sup>1,2</sup>The average percent canopy loss (col 3) and relative percent canopy loss (col 4) per each loss pixel, according to the 1-m orthophoto classifications.

<sup>3</sup>The overall average percent canopy loss (col 5) was computed as the percent of the landscape experiencing loss multiplied by the average percent cover loss per loss pixel (col 3).

Spatial patterns of canopy loss in Texas exhibited threshold responses with warm season VPD, warm season temperature, annual precipitation, and 2011 annual P-PET. When a climatic threshold was surpassed, more tree mortality occurred. A threshold response was apparent, where 4-km pixels had greater canopy loss with either a VPD anomaly greater than 0.66 kPa, a temperature anomaly greater than 1.6 °C, a percent

deviation in precipitation less than -38%, or a 2011 P-PET water deficit less than -1206 mm (Figure 9).

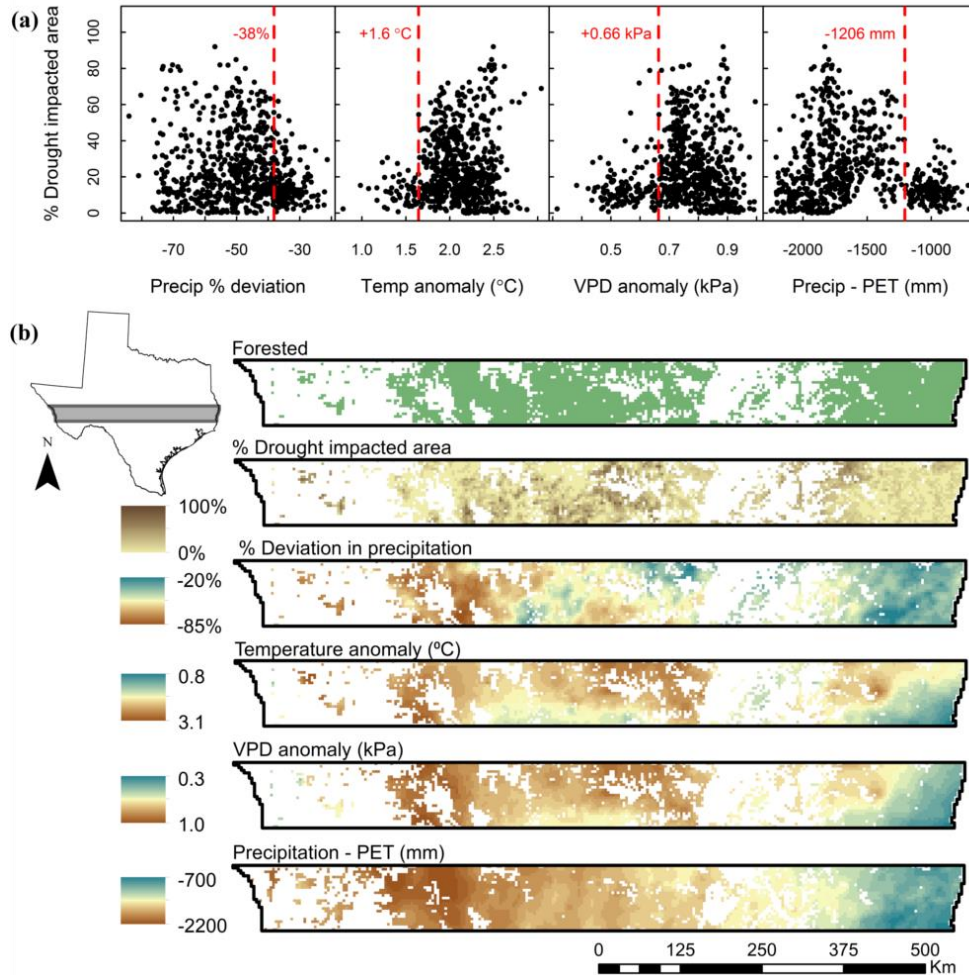


**Figure 9: Climatic drivers of the spatial patterns of canopy loss across Texas. (a)** Threshold values (red) for annual precipitation, warm season temperature, warm season vapor pressure deficit, VPD (PRISM Climate Group, 2015) and 2011 annual precipitation minus potential evapotranspiration, P-PET, (Abatzoglou 2013). Positive anomalies for temperature and VPD indicate greater mortality, whereas negative values for precipitation and P-PET signify greater canopy loss. **(b)** Spatial comparison of climate to percent impacted area and forest cover (majority of 4-km pixel within forest cover mask), along the 100 km by ~1000-km east-west transect. Data points (a) represent randomly selected 4-km pixels along the transect (b).

To test whether the climatic thresholds we identified for 2011 occurred in the past, we used PRISM data from 1950 to 2015. The temperature threshold was only crossed twice, during 1998 and 2011 (Figure 10), whereas the VPD anomaly was only surpassed once, during the 2011 drought. The precipitation threshold was crossed twice (1950s and 2011) over the historical climate period. Precipitation levels in 2011 were similar to the 1950s drought; however, the 2011 drought was uniquely characterized by higher temperatures and VPDs.

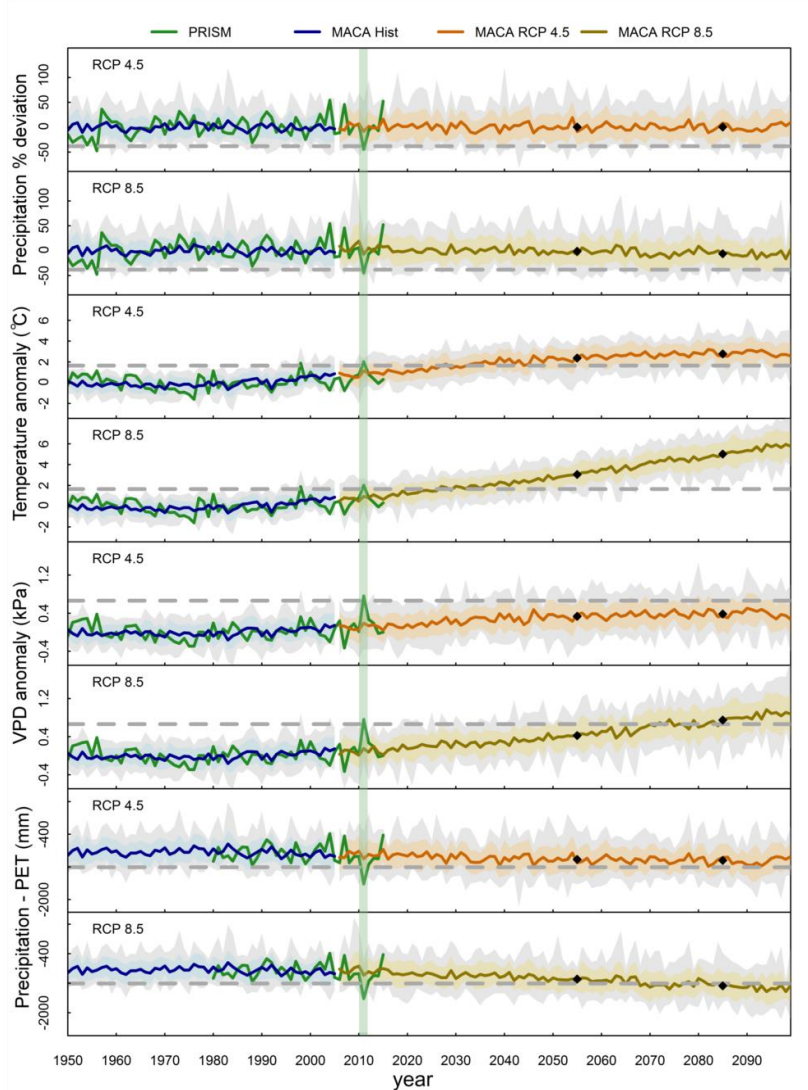
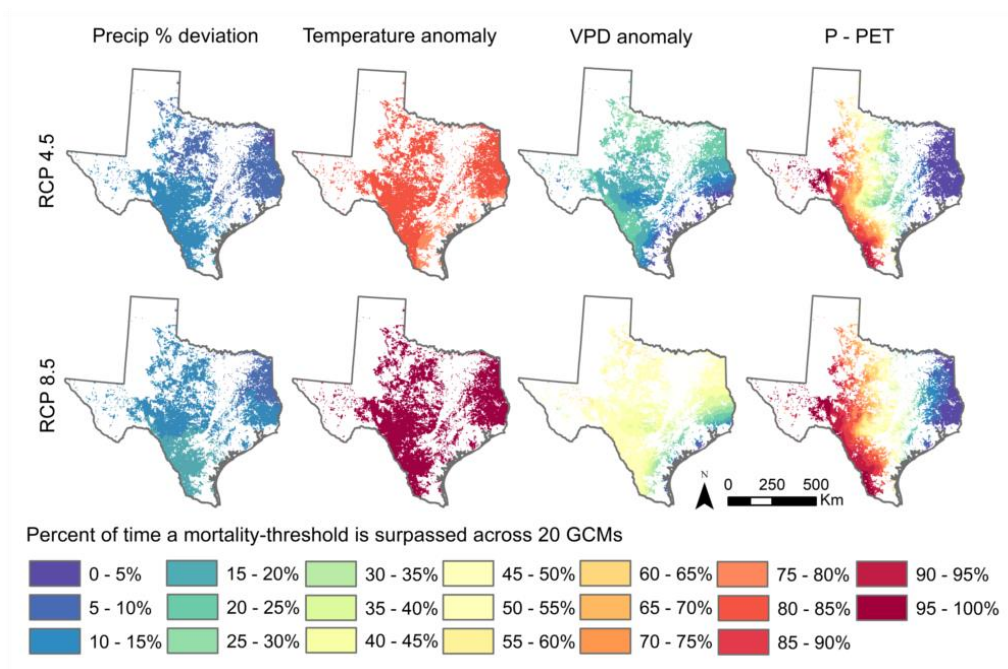


Figure 10: Historical and future projections of climate threshold crossings associated with canopy loss: Spatial averages of percent deviation in annual precipitation, anomalies in warm-season temperature and vapor pressure deficit (VPD), and annual precipitation minus potential evapotranspiration (PET) for all forested 4-km pixels in Texas. The 2011 drought shown in light green. Climatic thresholds indicated by grey dashed lines, as defined in Figure 9. Historical data acquired from PRISM Climate Group (2015) and Abatzoglou (2013). Projected statistically downscaled historical and future MACA climate data an ensemble of 20 GCMs (Abatzoglou & Brown, 2012); solid line: mean, shading: 1 standard deviation, grey shading: range. The first black diamond represents the mean for the period from 2040-2069 and the second: 2070-2099.

The proportion of times and models for which a threshold was projected to be crossed varied across space and was unique to each climate variable, when considering 20 GCMs and a 50-year time-period, 2050-2099 (Figure 11). Although, the ensemble mean for precipitation was never projected to cross the precipitation threshold in the future, for portions of the landscape, precipitation thresholds were crossed 4-16% (RCP 4.5) and 6-20% (RCP 8.5) of the time for the latter half of the 21<sup>st</sup> century and across 20 GCMs. Thresholds were crossed more often for VPD ranging from 0-28% (RCP 4.5) and 0-62% (RCP 8.5) as well as for temperature ranging from 75-86% (RCP 4.5) and 96-98% (RCP 8.5) (Figure 11). P-PET threshold crossings ranged from 0-100% for both RCP 4.5 and 8.5 scenarios. The precipitation thresholds were projected to be crossed more frequently for Central and South Texas, for both RCP 4.5 and 8.5, and the southern edge of East Texas (Pineywoods) for RCP 8.5. For VPD under both scenarios, and for temperature under RCP 4.5, thresholds were less likely to be crossed near the gulf coast; however, for RCP 8.5, the temperature threshold was crossed almost uninterruptedly for most of the region (Figure 11).



**Figure 11: Percent of time for which a climate threshold (defined in Figure 9) was surpassed, considering 20 general circulation models (GCMs) over the latter half of the 21st century (2050-2099). For example, if a climate threshold was crossed for 25 years in the 50-year period, for 10 of the 20 GCMs, then this would be represented by an average threshold crossing of 25%. We used statistically downscaled 4-km climate data for Representative Concentration Pathways (RCP) 4.5 and 8.5 scenarios (Abatzoglou & Brown, 2012).**

For the 94 ecological systems where trees were dominant and covered >200 km<sup>2</sup> in area, we present the top most and least impacted systems. Table 20, appendix B contains drought impacts for all 231 ecological systems dominated by tree species. The systems most negatively affected by the 2011 drought (Figure 12) were the pinyon-juniper (*Pinus cembroides*, *Juniperus deppeana*, *J. pinchotii*, and *J. flaccida*) and oak systems (*Quercus grisea*, *Q. emoryi*, *Q. hypoleucoides*, *Q. arizonica*, *Q. rugosa*, and *Q. mohriana*) of the

Trans Pecos, the post-oak (*Q. stellata*) woodlands of the Llano uplift, and the juniper woodlands (*J. ashei*, *J. virginiana*, *J. monosperma* and *J. pinchotii*) of the Edwards Plateau (Elliott et al., 2014; Moir, 1982). Furthermore, systems on sandy sites (e.g., sandy mesquite evergreen woodlands and sandy shinnery shrublands) tended to have more canopy loss. Alternatively, systems in riparian and mesic areas as well as managed systems were less impacted. Lastly, communities dominated by the invasive Chinese Tallow (*Triadica sebifera* L.), had some of the lowest canopy loss.

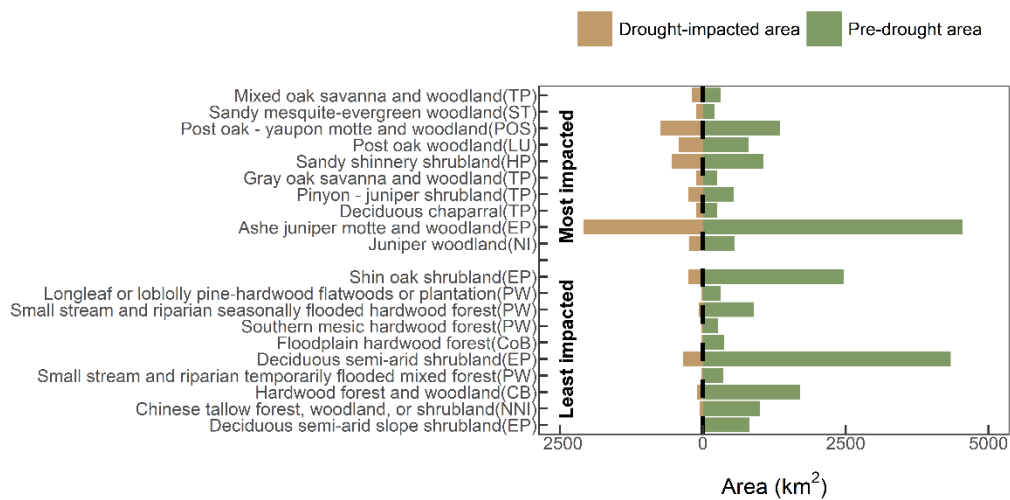


**Figure 12: The top 10 ecological systems with the highest relative loss (top) and lowest relative loss (bottom), due to the 2011 drought, as quantified through an overlay of our canopy loss maps with an ecological systems map (Elliott *et al.*, 2014). Only ecological systems dominated by trees (231 systems) and with > 200 km<sup>2</sup> of area (94 systems) in Texas were considered here. Natural regions in parentheses: TP – Trans Pecos; ST- South Texas; POS – Post Oak Savannah; LU – Llano Uplift; HP – High Plains, EP – Edwards Plateau; NI – Native Invasive; PW – Pineywoods; CoB – Coastal Bend; CB – Columbia Bottomlands; NNI – Non-Native Invasive.**

### **3.4 Discussion**

We mapped drought-induced canopy loss using a consistent method across a 5-fold precipitation gradient that spanned humid to semiarid regions. We took advantage of open-source remotely sensed imagery at two spatial scales and new machine learning algorithms to create binary canopy loss maps. We then used these maps to identify climatic thresholds that explained spatial patterns of canopy loss and determined which ecological systems were most impacted and thus potentially more vulnerable to climate change.

Across Texas, we found 9.5% canopy loss resulting from the 2011 drought in a region that is vulnerable to ongoing climate shifts. Canopy loss occurred across all the ecoregions of Texas, with the western systems most impacted. The humid systems (e.g., Pineywoods and Oakwoods/Blackland Prairies) had less relative canopy loss, 8% and 12% respectively, compared to the other more arid western systems, all with greater than or equal to 14% relative canopy loss (Table 9). However, canopy loss occurred across the entire precipitation gradient, signifying that drought-induced tree mortality was not limited to only semi-arid water-limited systems, as was also observed by Allen et al., (2010). Our estimates were corroborated by Texas Forest Service field surveys of observed tree mortality by genus (G. W. Moore et al., 2016), which found a ~6.2% loss of trees (stems) and a 7.5% loss of basal area following the 2011 drought. In this study we did not differentiate canopy loss caused directly from drought vs. indirectly from insects

or other pathogens. Many diseases in Texas are more likely to infect water stressed trees (e.g., in oaks, Hypoxylon canker, *Hypoxylon atropunctatum*, (Bassett & Fenn, 1984) and oak wilt, *Ceratocystis fagacearum* (A. D. Wilson, 2001) and for pines, Ips bark beetles (G. W. Moore et al., 2016)), and thus we still considered this drought-induced canopy loss.

Although overall our method was capable of predicting canopy loss across all six modeling zones ranging from closed canopy forests to open canopy woodlands/shrublands, the approach had some limitations. Underestimation could have occurred in select areas, firstly, because some of the cleared trees we excluded from the analysis could have been dead (e.g., salvage logging). Secondly, regrowth of grass and shrubs under dead canopies can reduce mortality signals (McDowell et al., 2015). Lastly, some studies have observed lagged mortality due to drought (Bigler, Gavin, Gunning, & Veblen, 2007); therefore, trees in Texas may have continued to die, beyond the acquisition date of our post-drought images.

Overestimates of canopy loss in some areas could have also occurred. Firstly, in scaling up to Landsat, some of the predicted mortality could be due to canopy thinning, or partial canopy die-back. In the fine-scale canopy loss maps we could more accurately distinguish between canopy thinning and dead canopy; therefore, misidentification of canopy thinning as mortality could account for some of the discrepancy between the fine-scale maps and the regional coarse-scale maps. Secondly, to avoid extensive leaf desiccation during drought, many of the trees in Texas can lose their leaves earlier in the

season in times of water stress and become “drought-deciduous”. We avoided detection of drought-deciduousness across Texas, because we selected post-drought imagery in 2012 instead of in 2011, directly following the drought. It is unlikely that a tree without leaves in 2011 and 2012 would have recovered. However, this was not the case for trees in South Texas, where we did note evidence of full recovery of trees post-2012 (observed in 10 out of 42 orthophotos in South Texas and 1 out of 29 along the southern edge of the Oakwoods). Post-drought orthophotos used as training data were acquired in 2012; however, post-drought Landsat images used for scaling were acquired in 2013 and 2014. Therefore, if trees recovered post 2012, then the training data would not have captured this recovery. This was likely why the models in South Texas had lower accuracy, particularly in the true positive rate.

Many plant communities were differentially impacted by the drought. Similar to field surveys conducted by the Texas Forest Service in 2012 (G. W. Moore et al., 2016), we found that the 2011 drought did not affect all species/ecological systems equally. Specifically, systems dominated by juniper woodlands, pinyon-juniper shrublands, gray oak savanna and woodlands, and post oak woodlands (Figure 12) were most impacted; these systems may be particularly vulnerable to climate change. During the 1950s drought, similar systems were also impacted, including oak (post, spanish, blackjack and shin) as well as juniper and elm, with particularly high levels of *J. ashei* mortality in central Texas (Young, 1956). Since the 1950s, *J. ashei*, a woody encroacher, recovered only

to be once again killed in large numbers by the 2011 drought. This result would suggest that drought was acting as a control to check the encroachment of *J. ashei*. Other studies, have also found mortality of recently encroached shrubs (Fensham et al., 2009). Future drought events could turn these encroaching shrubs/trees from carbon sinks to carbon sources with substantial consequences to regional carbon cycling (Barger et al., 2011).

Interestingly, much research has focused on pinyon-juniper woodlands dominated by *Pinus edulis* and *Juniperus* spp of Arizona, New Mexico, and Colorado, where significant tree mortality due to drought and bark beetle occurred, mostly impacting *P. edulis* (Floyd et al., 2009; Mueller et al., 2005). However, less research has focused on drought-induced tree mortality in the pinyon-juniper stands in the Trans Pecos, with different dominant species including *P. cembroides*, *J. deppeana*, *J. pinchotii*, and *J. flaccida* (Moir, 1982). The pinyon juniper stands of the Trans Pecos also had significant drought-induced canopy loss. A study of the pinyon-juniper stands in Big Bend National Park, found that *P. cembroides* had the highest tree mortality followed by *J. deppeana*, and *Q. emoryi*, resulting from a combined stress of a severe winter freeze event and the 2011 drought (Poulos, 2014). Therefore, within the pinyon-juniper communities of both these regions, the pinyon pine species (e.g., *P. cembroides* and *P. edulis*) were more vulnerable to drought compared to the juniper species.

In identifying how climate explained spatial patterns of canopy loss across the 5-fold precipitation gradient in Texas, we found that canopy loss patterns revealed

threshold responses. For example, when either a 1.6 °C temperature anomaly, 0.66 kPa VPD anomaly, -38% deviation in precipitation, or -1206 mm P-PET water deficit were crossed, then canopy loss increased substantially. Although the precipitation threshold was crossed during the 1950s and 2011 droughts, over the past 50+ years the temperature threshold was surpassed for the forested areas of Texas only during 1998 and 2011, and the VPD threshold only in 2011. The temperature threshold was crossed in both 1998 and 2011; however, only in 2011 was there a widespread loss of trees in Texas, which suggests that perhaps these forests were responding more to changes in VPD than temperature. Other studies have also found VPD to be an important climate driver of tree mortality (Breshears et al., 2013; Eamus, Boulain, Cleverly, & Breshears, 2013; McDowell et al., 2016; Williams et al., 2013). VPD is the difference between saturation vapor pressure and actual vapor pressure. Saturation vapor pressure is exponentially related to temperature based on the Clausius-Clapeyron equation and actual vapor pressure is a measure of atmospheric moisture content (Anderson, 1936). The conditions leading to the 2011 VPD anomaly occurred due to a combination of high saturation vapor pressure, attributable to the record high temperatures and the low moisture content in the atmosphere (Williams et al., 2014). For example, atmospheric moisture could increase with rising temperatures to maintain a constant relative humidity. However partly due to limited surface water, models in the southwestern United States do not predict that relative humidity will likely remain constant in the

future (Williams et al., 2014). Therefore, VPD is projected to increase with climate change for the southwestern US, both due to increases in the saturation vapor pressure due to rising temperatures and a minimized increase in atmospheric moisture (Williams et al., 2014).

The 2011 climate conditions were projected to be surpassed on average for the periods from 2040-2099 for the temperature anomaly and 2070-2099 for both the VPD anomaly and the 2011 P-PET water deficit, under the RCP 8.5 scenario. As these anomalies were projected to become the norm for the latter half of the 21<sup>st</sup> century, the projected changes could have severe effects on the structure and function of forests in Texas. The ensemble range of 20 GCMs encompassed the variability in historical precipitation; however, the ensemble mean did not, due to buffering that occurred with averaging many models, as other studies in Texas have also noted (Venkataraman, Tummuri, Medina, & Perry, 2016). Therefore, although precipitation projections for the ensemble mean did not cross the precipitation threshold (Figure 10), some of these GCMs individually did project threshold crossings in the future (Figure 11). Additionally, there is still great uncertainty surrounding precipitation and VPD projections of extreme values. Many GCMs do not include regional processes and feedbacks, and thus projections of climate extremes at the regional scale are often less accurate than global trends (Burke, Brown, & Christidis, 2006; Jentsch, Kreyling, & Beierkuhnlein, 2007). Given that future precipitation follows historical observations,

atmospheric water demand will increase where temperatures increase; consequently, trees will need to increase evapotranspiration, which could lead to greater water stress (McDowell et al., 2015). This was reflected in the increasingly negative annual P-PET water deficits for the later half of the 21<sup>st</sup> century (Figure 10).

There are limitations in defining empirical relationships between climate and spatial patterns of canopy loss. Although climate contributed to these canopy loss patterns, the trends were sometimes variable, indicating that other local-scale factors related to soil, topography, management, and stand density also likely played a role. Moreover defining thresholds that lead to canopy loss is only a first step. The sequence of several drought events can matter more than trends or single events (Miao, Zou, & Breshears, 2009), and the time spent below a threshold can be more significant than the actual threshold crossing for some systems (McDowell et al., 2013). Also, climatic thresholds defined for the 2011 drought may cause more or less tree mortality in the future depending on the ecosystem. For example, a drought may kill vulnerable and poorly adapted trees, with surviving trees remaining on more favorable landscape positions. However, the capacity of a heterogeneous landscape to buffer climate could be overcome if climate extremes are too severe or rapid and if regional climate is coupled to local climate (Hylander, Ehrlen, Luoto, & Meineri, 2015). Also, surviving trees could become more resilient to drought by switching carbon allocation and increasing root or sapwood area at the expense of leaf area (Bréda, Huc, Granier, &

Dreyer, 2006), or recovering from declines in hydraulic conductivity through xylem refilling (Meinzer & McCulloh, 2013). Alternatively, surviving trees have the potential to become more vulnerable to future droughts due to xylem dysfunction, such as cavitation fatigue, (Hacke, Stiller, Sperry, Pittermann, & McCulloh, 2001) and reduced carbon reserves (Galiano, Martínez-Vilalta, & Lloret, 2011).

Future research is needed on the recovery of ecosystems following drought, mortality thresholds that incorporate both climate and the environment, and improved projections of extreme climatic events. This study does not quantify recovery following drought. If favorable climates for seedling establishment are never achieved, semi-arid communities may fail to recover following a mortality event (Breshears et al., 2005) or differential species recovery may favor species that resprout (Zeppel et al., 2015) and that have more favorable recruitment under global change. Additionally, we only examined how canopy loss related to climatic thresholds. Stronger correlations may exist by incorporating climate and environment, for example by including soil moisture thresholds (H. D. Adams et al., 2013). Metrics derived from process-based models (e.g., soil water) have been used to predict future range shifts in western North America (Mathys, Coops, & Waring, 2016). Lastly, improvements are needed for projections of extreme climate conditions in general circulation models (Bahn, Reichstein, Dukes, Smith, & McDowell, 2014), that work at both regional and global scales. Understanding

changes in mean climate values can only go so far (Jentsch et al., 2007), as forests are more likely to respond to changes in extremes.

## **4. Accounting for landscape heterogeneity improves spatial predictions of tree vulnerability to drought**

### **4.1 Introduction**

As climate change continues, more frequent and intense heatwaves and droughts will likely lead to greater tree mortality (C. D. Allen et al., 2015). Instances of climate-induced tree mortality have already been documented worldwide (C. D. Allen et al., 2010). Increases in tree die-off can alter plant community composition and species distributions (Engelbrecht et al., 2007; Mueller et al., 2005), with consequences to biodiversity, carbon cycling, hydrology and biophysics (e.g., Ciais et al., 2005; Jackson et al., 2008; Vicente-Serrano et al., 2014).

To better understand the fate of forests under a changing climate, model improvements are needed to predict ecosystem changes now and in the future. Dynamic Global Vegetation Models, DGVMs, are typically used to predict how forests will respond to changes in climate. While DGVMs include various mechanisms for modeling tree mortality, their algorithms are rarely tested with spatially explicit canopy loss observations (McDowell et al., 2011). Although many mortality algorithms depend on climate or heat-stress thresholds (McDowell et al., 2011; Schwantes et al., 2017) spatial patterns of canopy loss often follow local stress gradients and depend on both climate and edaphic factors (Gitlin et al., 2006; Loehle & LeBlanc, 1996; McLaughlin et al., 2017). Moreover, DGVMs typically account for neither spatial interactions (Fisher et al., 2010) nor landscape heterogeneity of abiotic factors at fine spatial resolutions, such as soil

conditions, slope and aspect (Moorcroft, 2006). Although, many studies have focused on improving model representations of the physiological mechanisms of tree mortality (Mackay et al., 2015; McDowell et al., 2013; Parolari et al., 2014), only a few studies have examined whether including landscape heterogeneity can improve predictions of tree mortality (Anderegg et al., 2015; Tague et al., 2013; Tai et al., 2017).

Spatial patterns of tree mortality are associated with changes in soil texture and depth (Bowker et al., 2012; Peterman & Waring, 2014; Twidwell et al., 2014), topographic position (H. R. Adams, Barnard, & Loomis, 2014; Hawthorne & Miniati, 2017) and local water stress gradients (Gitlin et al., 2006). Soil moisture variability across a landscape is driven by spatial variability in soil texture and depth to bedrock, surface runoff and subsurface lateral flow of water (K. J. Beven & Kirkby, 1979; Dunne et al., 1975), and differences in radiation and resulting evaporation due to aspect and slope (McCune & Keon, 2002; I. D. Moore et al., 1991). This landscape heterogeneity creates microsites or refugia with cooler, moister conditions that allow for tree survival during severe drought events. However, rarely is landscape heterogeneity considered in models, even though topography is important in identifying refugia locally buffered from climate change.

Many studies have found that the topographic compound index, TCI, is significantly correlated to spatial patterns of soil moisture (I. D. Moore, Burch, & Mackenzie, 1988; Western, Grayson, Blöschl, & Willgoose, 1999) and tree mortality

(Kaiser, McGlynn, & Emanuel, 2013). TCI is a spatial distribution function that can be used to describe lateral subsurface water flow along hillslopes (K. Beven, 1995). It is a physically based index of hydrologic similarity, with areas having similar index values likely to respond in hydrologically similar ways (K. Beven, 1997). TCI is defined as  $\ln(a_c/\tan(b))$ , where  $a_c$  is the upslope contributing area per unit contour length and  $\tan(b)$  is the local land surface slope. The index assumes that (1) the hydraulic gradient (i.e., a metric controlling the capacity of accumulated water to pass through the grid cell) is approximated by the local slope and (2) lateral discharge (i.e., the water volume passing through a grid cell) is proportional to upslope contributing area (K. Beven, 1997; Quinn, Beven, & Culf, 1995).

Spatial patterns of soil moisture are also correlated with solar radiation (Western et al., 1999) and landscape positions with higher insolation often have greater tree mortality (Kaiser et al., 2013). In the northern hemisphere, south-facing slopes tend to have greater temperatures and evaporative demand, because they receive more radiation per unit area (i.e. insolation) compared to north-facing slopes. Additionally, although the amount of radiation is equivalent on eastern- and western-facing slopes averaged over a day, insolation on western-facing slopes is highest in the afternoon, leading to higher afternoon temperatures (McCune & Keon, 2002). Higher temperatures typically lead to greater vapor-pressure deficits and potential evapotranspiration, PET. Under high temperatures and vapor-pressure deficits, trees usually close stomata, thus

decreasing transpiration and the rates of photosynthesis and net assimilation.

Photosynthesis also tends to be higher in the morning when leaf temperatures and vapor pressure deficits are low (Owens, 1996), at the time when eastern-facing slopes have higher insolation. We can create spatially explicit maps of PET by applying a heat-load index that accounts for both potential direct incident radiation as well as temperature differences, by rescaling aspect so that southwestern-slopes have the highest values and northeastern-slopes have the lowest, considering steepness of slope and latitude (McCune & Keon, 2002).

Two kinds of forest ecohydrological models exist: (1) empirically-based models defining statistical relationships, but with little input of a system's structure, and (2) process-based models defining key mechanisms to describe the structure and functioning of a system (Korzukhin, Ter-Mikaelian, & Wagner, 1996). Inevitably, there is a trade-off between purely empirical models, which can be biased when extrapolated beyond observed input values, and process-based models that can have higher error attributable to lack of data for parameters, especially at global scales (H. D. Adams et al., 2013). However, these model classifications are not mutually exclusive. We can combine modeling frameworks by using statistical-dynamical models of soil-plant water to model the probability of tree vulnerability to drought. Simplified mortality mechanisms are incorporated (Parolari et al., 2014); the model is forced using stochastic precipitation (Laio et al., 2001; Rodriguez-iturbe & Porporato, 2004); and spatially explicit input

parameters are included. The probability of tree mortality can then be predicted given the mean intensity, duration, and number of threshold crossings for percent loss in hydraulic conductivity (PLC) associated with tree vulnerability. Simulations show, for instance, that tree species impacted by drought spend more time at higher PLC values (H. D. Adams et al., 2017; McDowell et al., 2013); chronically high PLC values among other risk factors can also predispose a tree to mortality (Sperry & Love, 2015).

From Oct 2010 to Sept 2011, Texas experienced its most severe one-year drought since record-keeping began in 1895 (Hoerling et al., 2013). The drought killed millions of trees across the region (G. W. Moore et al., 2016; Schwantes et al., 2017, 2016). In this study, we combined a new modeling approach with a detailed spatial dataset of tree canopy loss (Schwantes et al., 2017) to identify which processes were most important for determining tree water stress due to drought. Starting with a non-linear stochastic model of plot-scale soil moisture dynamics for a single watershed in central Texas, we added complexity in the form of multiple drivers of tree mortality, including spatial heterogeneity of soil parameters, lateral redistribution of water using TCI, and spatially variable PET attributable to differences in aspect. What makes our approach unique is that it integrates plant hydraulics and landscape processes, incorporating effects of lateral redistribution of water as well as radiation and temperature differences on dynamic soil moisture. A second objective was to explore the effect of incorporating landscape heterogeneity in models, when forecasting future drought stress. To better

understand how landscape heterogeneity will buffer against future droughts projected in the 21<sup>st</sup> century, we used climate projections under multiple climate-warming trajectories, comparing models with and without landscape heterogeneity.

## **4.2 Materials and Methods**

### **4.2.1 Study area**

Our study area is a watershed in the Edwards Plateau region of Texas (Figure 13). We model tree water stress for a dominant tree species, *Juniperus ashei*, which experienced substantial mortality during the 2011 drought (G. W. Moore et al., 2016; Schwantes et al., 2017, 2016). Our analysis only includes areas where *J. ashei* is a dominant species, as defined using an ecological systems map of Texas (Elliott et al., 2014) and a percent tree cover threshold > 25%, using the National Land Cover Database percent tree cover product (Homer et al., 2015). In 2011, a severe drought and heatwave led to 9.5% tree canopy loss overall across Texas, with *J. ashei* woodlands being one of the systems most impacted by the drought (Schwantes et al., 2017). Within the study watershed, we acquired maps of drought-impacted area in 2011 from Schwantes *et al.* (2017). We then used these drought-impacted area maps to validate our models of tree water stress.

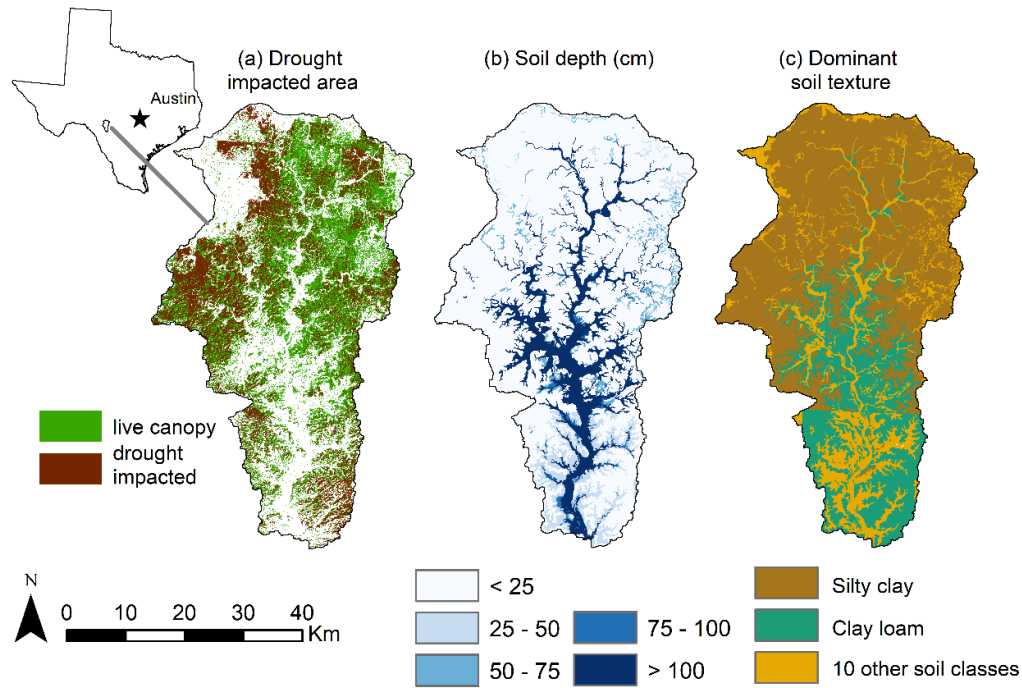


Figure 13: Comparison of (a) drought-impacted area, as defined as pixels with > 25% canopy loss acquired from Schwantes et al., (2017), (b) soil depth and (c) soil texture, both acquired from the SSURGO database (United States Department of Agriculture, 2014), for a watershed in the Edwards Plateau region of Texas.

#### 4.2.2 Soil water balance model

Following Laio et al. (2001) we employ a non-linear stochastic, ordinary differential equation of soil moisture dynamics, where rainfall follows a marked Poisson process. We express the soil moisture balance at a point as:

$$nZ_r \frac{ds(t)}{dt} = R(t) - I(t) - Q[s(t), t] - ET[s(t)] - L[s(t)] \quad \text{Equation 4.1}$$

where  $Z_r$  is the active soil depth,  $n$  the porosity,  $s(t)$  the relative soil moisture content,  $R(t)$  the rainfall rate,  $I(t)$  the amount of rainfall intercepted by the canopy cover,  $Q[s(t),t]$  the surface/subsurface runoff rate,  $ET[s(t)]$  the evapotranspiration rate, and  $L[s(t)]$  the leakage. The runoff, evapotranspiration, and leakage rate depend on soil moisture levels through simple yet realistic representations of plant hydraulics, soil properties, and topography. Under steady state conditions, we obtain analytical solutions of the soil moisture probability density function for each 30-m grid cell across the watershed. The solution is provided in the supporting information, Eq. C1; however, the full derivation can be found in Laio et al. (2001) and Rodriguez-Iturbe et al. (1999). We then assess the role of climate, soil properties, plant hydraulics, and topography on soil moisture dynamics and associated tree water stress.

#### **4.2.3 Infiltration: rainfall, canopy interception, and lateral water flow**

Infiltration from rainfall is treated as an external random forcing factor where the occurrence of a rainfall event follows a marked Poisson process with a mean storm frequency,  $\lambda$  ( $\text{day}^{-1}$ ). The depth of each rainfall event follows an exponential probability density function with a mean depth,  $\alpha$  (cm). These distributions are commonly used to model rainfall at the daily time-scale (Laio et al., 2001; Parolari et al., 2014; Porporato, Laio, Ridolfi, & Rodriguez-Iturbe, 2001; Rodriguez-Iturbe et al., 1999). Following Daly et al. (2008), we assume that for small storm events below a certain threshold,  $\Delta$ , the canopy completely intercepts all rainfall. For *J. ashei*,  $\Delta$  equals 0.25 cm; storms below this

value are typically fully intercepted (Owens, Lyons, & Alejandro, 2006). The process describing the frequency of a rainfall event then becomes a censored marked Poisson process, and  $\lambda$  is reduced to  $\lambda'$  as:

$$\lambda' = \lambda e^{-\Delta/\alpha} \quad \text{Equation 4.2}$$

For larger rainfall events above  $\Delta$ , throughfall (e.g., precipitation minus interception) is linearly related to the depth of the rainfall event (E. Daly et al., 2008). On average ~35% of bulk rainfall is intercepted by the canopy of *J. ashei* per storm event and sequentially lost due to evaporation (Owens et al., 2006). The depth of each rainfall event still follows an exponential distribution; however, the mean rainfall depth is reduced to  $(k_i\alpha)$ , where  $k_i$  is equal to 0.65 (Owens et al., 2006).

To predict the pattern of soil moisture attributable to topographic position (e.g., describing lateral surface and subsurface flow from topographically divergent areas such as ridges to topographically convergent areas such as valleys), we further modify the mean rainfall depth  $(k_i\alpha)$  to depend on each pixel's topographic compound index, TCI, which is defined as:

$$TCI = \ln\left(\frac{a_c}{\tan(b) + 0.001}\right) \quad \text{Equation 4.3}$$

where  $a_c$  is upslope contributing area ( $\text{m}^2$ ) and  $b$  is the local slope angle (degrees) (K. Beven, 1997). Upslope contributing area ranges from  $90 \text{ m}^2$  (e.g., the size of a single pixel) to the total area of the watershed ( $1961 \text{ km}^2$ ). To avoid undefined values of TCI in areas of zero local slope (i.e., a zero denominator), we add a small number (0.001) to the

denominator for all pixels. TCI is calculated using a 30-m digital elevation model (DEM) from the Shuttle Radar Topography Mission (SRTM; Version 2). We calculate  $a_c$  using a multiple flow direction approach and the TauDEM ArcGIS toolbox (Tarboton, 2005).

Topographically convergent areas (e.g., valleys) tend to be associated with higher than average values of TCI, greater upslope contributing area (e.g., greater lateral discharge, water volume passing through a grid cell) and lower slopes (e.g., low hydraulic gradient, a metric associated with the capability of accumulated water to pass through a grid cell). Therefore, the mean rainfall depth is adjusted for each pixel to account for landscape position, by redistributing water from areas of low TCI to areas of high TCI. Thus, we use the index to modify water inputs ( $\alpha'$ ), which now represent both infiltration from rainfall as well as lateral surface flow and subsurface lateral discharge. If soil moisture is rapidly redistributed daily during each individual storm event then  $\alpha'$  can be reasonably linked to TCI as

$$\alpha' = k_i * \alpha \left[ 1 + f * \frac{[TCI - \overline{TCI}]}{\overline{TCI}} \right] \quad \text{Equation 4.4}$$

where  $f$  is a parameter that controls the magnitude of lateral redistribution. A sensitivity analysis is performed using  $f$  from 0.1 to 1.0, in increments of 0.1.

#### **4.2.4 Losses: evapotranspiration and leakage**

Evapotranspiration,  $ET(s)$ , accounts for losses from both soil evaporation  $E(s)$  and tree transpiration  $T(s)$ . We assume that for this system,  $ET(s)$  has an upper limit defined by the potential evapotranspiration,  $PET$ , which depends on climate conditions and the

tree species. We also assume that tree water uptake from the soil declines as a function of water stress. Under water stress, trees will partially close their stomata, and transpire at a reduced rate, up to a point where stomata close and transpiration ceases. Following (Laio et al., 2001), we model this process by assuming that trees transpire at a maximum level above a soil moisture associated with a stress point ( $s^*$ ). When soil moisture drops below  $s^*$ , transpiration decreases linearly up to a soil moisture associated with stomatal closure ( $s_w$ ). Below  $s_w$  only soil evaporation occurs, which we model as decreasing linearly from potential soil evaporation,  $PE$ , at  $s_w$  to zero at the hygroscopic point,  $s_h$ , defined as follows:

$$ET(s) = \begin{cases} PE' \frac{s - s_h}{s_w - s_h}, & s_h < s \leq s_w, \\ PE' + (PET' - PE') \frac{s - s_w}{s^* - s_w}, & s_w < s \leq s^*, \\ PET', & s^* < s \leq 1, \end{cases} \quad \text{Equation 4.5}$$

Evapotranspiration also depends on the surface energy budget (I. D. Moore et al., 1991). We account for spatial variation in  $PET$ , defined as:

$$PET' = PET * HL \quad \text{Equation 4.6}$$

by using a heat load index ( $HL$ ), which accounts for potential direct incident radiation and temperature differences attributable to aspect and steepness of slope (Evans, Oakleaf, Cushman, & Theobald, 2014; McCune & Keon, 2002). Higher values of  $PET'$  are associated with greater radiation (e.g., south-facing slopes) and warmer afternoon temperatures (e.g., western-facing slopes).

To differentiate potential soil evaporation ( $PE$ ) from potential transpiration, we use the fraction of solar radiation that the canopy intercepts, defined as:

$$v_f = 1 - e^{-k_f * LAI} \quad \text{Equation 4.7}$$

where  $LAI$  represents leaf area index and  $k_f$  is a light extinction coefficient (Elkington et al., 2014). The higher this vegetation factor ( $v_f$ ), the less  $PET$  is partitioned into potential soil evaporation ( $PE$ ), following:

$$PE' = PET' * (1 - v_f) \quad \text{Equation 4.8}$$

We measured LAI using a LAI-2200C Plant Canopy Analyzer (LI-COR, Lincoln, NE, USA) during July 2016 at Colorado Bend State Park, in Central Texas. All measurements were taken at twilight, to minimize changing sky-conditions and scattering errors. We used a 45° view cap and masked out the outer most ring. Measurements were taken every 1 m, along ten 10-m transects. Average LAI for stands of *J. ashei* was  $2.92 \pm 0.46$  ( $\pm$  std. dev.). We used a light extinction coefficient,  $k_f$ , for juniper of 0.37 from Kiniry (1998).

The soil moisture value at which stomata start to close,  $s^*$ , and the soil moisture at which stomatal close completely,  $s_w$ , both depend on tree species and soil texture. We obtain the relative soil moisture,  $s$ , for a corresponding soil water potential,  $\Psi_s$ , using soil water retention curves, as defined in Clapp and Hornberger (1978), as follows:

$$\Psi_s = \bar{\Psi}_s s^{-b} \quad \text{Equation 4.9}$$

where  $\bar{\Psi}_s$  and  $b$  are experimentally derived parameters that vary with soil texture. The relative soil moisture for the hygroscopic point,  $s_h$ , and the field capacity,  $s_{fc}$ , can be

found using Eqn 9 and the following soil water potentials respectively,  $\Psi_{sh} = -10$  MPa (Laio et al., 2001) and  $\Psi_{sfc} = -0.033$  MPa (Hudson, 1994). To define  $\Psi_{s*}$  we assume that stomata start to close when the soil water potential reaches a point associated with 50% loss of hydraulic conductance in the leaves,  $-1.67$  MPa for *J. ashei* (Johnson et al., 2016), and we define  $\Psi_{sw}$ , by assuming that stomata close completely when the soil water potential reaches the turgor loss point for *J. ashei*, which is  $-3.8$  MPa (Johnson et al. in review).

Soil properties were obtained from the Soil Survey Geographic (SSURGO) database (United States Department of Agriculture 2014). Soil depth ( $Z_r$ ) was taken directly from SSURGO. We computed area- and depth-weighted averages of percent sand, clay, and silt for each soil polygon. Based on these soil texture observations, we classified each soil polygon as one of 12 United States Department of Agriculture (USDA) soil classes. The experimentally derived parameters for the soil water retention curves,  $\bar{\Psi}_s$  and  $b$ , the saturated hydraulic conductivity,  $K_s$ , and the porosity,  $n$ , were estimated using the USDA soil type classifications, following Clapp and Hornberger (1978), Daly et al. (2004), and Laio et al. (2001). Lastly, we assume that the soil hydraulic conductivity,  $K(s)$ , follows an exponential decay from  $K_s$ , at  $s = 1$  to zero, at  $s = s_{fc}$ :

$$K(s) = L(s) = \frac{K_s}{e^{\beta(1-s_{fc})} - 1} \left[ e^{\beta(s-s_{fc})} - 1 \right], \quad s_{fc} < s \leq 1 \quad \text{Equation 4.10}$$

where  $\beta$  depends on the soil texture and is equal to  $2b + 4$  and  $b$  is defined in Eqn 4.9 (Laio et al., 2001).

## 4.2.5 Static and dynamic water stress

Our objective is to model tree water stress in a semi-arid ecosystem and evaluate factors contributing to tree mortality. In semi-arid systems, trees are well adapted to handle stress conditions below soil moistures associated with turgor loss ( $s_w$ ); therefore, we define a new soil moisture level below the turgor loss point, at which a tree is under severe stress and vulnerable to mortality,  $s_m$ . We define  $\Psi_{sm}$  as the soil water potential associated with a 50% loss in hydraulic conductivity in the roots, -9.48 MPa for *J. ashei* (Johnson et al., 2016). Therefore, we adapt the static water stress equations developed by Porporato et al. (2001), and define static water stress,  $\zeta$ , as zero at  $s > s_m$  to approaching 1 as  $s$  approaches the hygroscopic point,  $s_h$ :

$$\zeta(t) = \left[ \frac{s_m - s(t)}{s_m - s_h} \right], \quad s_h < s(t) \leq s_m \quad \text{Equation 4.11}$$

We expect that larger deviations from  $s_m$  would result in higher probabilities of tree mortality. Derivations for computing the probability distribution for the static water stress,  $\zeta$ , Eqn C3, as well as the mean static water stress,  $\bar{\zeta}$ , Eqn C6, and the mean static water stress given that the tree was under stress,  $\bar{\zeta}'$ , Eqn C7, can be found in the supporting information section.

To predict tree vulnerability to drought-induced tree mortality, we calculate the dynamic water stress  $\bar{\theta}$  as follows:

$$\bar{\theta} = \begin{cases} \left( \frac{\bar{\zeta}' \bar{T}_{sm}}{T_{seas}} \right)^{1/\sqrt{\bar{n}_{sm}}} & \text{if } \bar{\zeta}' \bar{T}_{sm} < T_{seas} \\ 1 & \text{otherwise,} \end{cases} \quad \text{Equation 4.12}$$

$\bar{\theta}$  was adapted from the original equation proposed by Porporato et al. (2001) by incorporating  $\bar{\zeta}$  and two crossing properties below the soil moisture threshold associated with severe water stress and potential mortality,  $s_m$ . The two crossing properties include:  $\bar{n}_{s_m}$  the average number of crossings below  $s_m$ , and  $\bar{T}_{s_m}$  the average time spent below  $s_m$ . As such, dynamic water stress incorporates mean intensity, duration, and frequency of soil water deficits associated with crossings below the point to which a tree loses 50% of its hydraulic conductivity in the roots. We can obtain analytical solutions for both  $\bar{T}_{s_m}$  and  $\bar{n}_{s_m}$ . Full solutions are in the supporting information, Eqn C8 and Eqn C9, respectively. We used the full year as the duration of the growing season ( $T_{\text{seas}}$ ), because *J. ashei* is an evergreen species, and the model was run at a 30-m spatial resolution.

#### 4.2.6 Historical and future projections of water stress

Historical, 1980-2015, spatially interpolated 4-km gridded daily precipitation and monthly potential evapotranspiration,  $PET_g$ , values were acquired from GridMET (Abatzoglou, 2013). We used spatial averages across the watershed for annual  $PET_g$ , the mean rainfall depth,  $\alpha$ , and the average time between rainfall events,  $1/\lambda$ .  $PET_g$  was calculated using Penman-Montieth for a grass reference surface (Abatzoglou, 2013). For a similar juniper-dominated woodland/savannah in the Edwards Plateau of Texas, Heilman *et al.*, (2014) found that the average annual  $PET$  was 69 cm from 2005-2009, whereas the  $PET_g$  estimates in this region were 176 cm according to GridMET data;

therefore we applied a plant correction coefficient of 0.39. This value was similar to expected crop coefficients for trees, which range from 0.4-1.0 (R. G. Allen, Pereira, Raes, & Smith, 1998). Therefore,  $PET$  for *J. ashei* was calculated by multiplying the crop coefficient, 0.39, by  $PET_g$  acquired from GridMET (Abatzoglou, 2013).

We also acquired downscaled (4-km) climate projections from the coupled model intercomparison project, CMIP5, under two representative concentration pathways, RCP, 4.5 and 8.5 trajectories from 2006-2099 for  $PET_g$  and precipitation (Abatzoglou & Brown, 2012). Of 20 general circulation models (GCMs) we considered, we selected 10 GCMs that showed the best performance in projecting historical annual precipitation values (1980-2005) for our study watershed, considering mean absolute error (MAE) in annual precipitation. We again took spatial averages across the watershed for future annual projections of  $PET_g$ ,  $\alpha$ , and  $\lambda$ . We then examined historical (1980-2016) and future projections of dynamic water stress (2006-2099) for models with and without landscape heterogeneity.

#### **4.2.7 Accuracy assessments**

The soil water balance model was run for each 30-m grid cell within the watershed, to obtain spatially explicit estimates of tree water stress. We then compared our modeled results forced using  $PET$ ,  $\alpha$ , and  $\lambda$  values for 2011 to remotely sensed 30-m drought impacted area maps for 2011 from Schwantes et. al., (2017), where areas of drought-impact were defined as having greater than 25% canopy loss. We first

aggregated both modeled results and observations of drought impacted area to hydrologically similar but non-contiguous stands of *J. ashei*, similar to Tai et al., (2017). Hydrologically similar stands,  $n = 24$ , were defined as stands with (1) similar aspects, NE,  $-45^{\circ}\sim 135^{\circ}$  versus SW,  $135^{\circ}\sim 315^{\circ}$ , (2) with similar soil depths,  $< 100$  cm versus  $> 100$  cm, (3) soil texture, e.g., silty clay, clay loam, or other, and (4) with topographic divergence versus convergence, TCI below or above the mean, respectively. Following aggregation, we used linear regressions to compare modeled outputs to observations of drought-impacted areas.

We also identified stands of spatially contiguous pixels of two classes: (1) drought-impacted vs. (2) homogenous live canopy. Pixels were considered contiguous if one of eight neighboring cells was the same class. We then compared explanatory power (e.g., Cragg and Uhler's pseudo  $R^2$ ) for logistic regressions, in predicting whether a stand was either drought-impacted vs homogenous live canopy using dynamic water stress as the continuous predictor variable. Dynamic water stress represents a probability of tree vulnerability to drought. Therefore, in order to select a threshold of dynamic water stress that best distinguished drought-impacted stands from live canopy stands, we also used receiver operating characteristic (ROC) curves (Sing et al., 2005). For multiple cut-off values of the modeled dynamic water stress, ROC curves plot true positive rate (TPR, accurately predicting a drought-impacted stand) against true negative rate (TNR, accurately predicting a homogenous live canopy stand). The cut-off

value that balanced TPR and TNR was chosen. We used 10-fold cross validation, where 10% of the data was withheld for testing and the remaining 90% was used in the ROC curve analysis; we repeated this 10 times, using a different 10% testing dataset, and averaged percent accuracy and cutoff values across all 10 runs. To test whether accuracy improved when considering average dynamic water stress in larger stands, we sequentially removed stands below a certain size threshold. Other studies have found that aggregation up to a 100-m pixel (e.g., 1 ha) was necessary to improve correlations between modeled and observed soil moisture (Pellenq et al., 2003). The water stress model was solved using MATLAB; statistical analysis was conducted in R; and spatial analysis was performed using ArcGIS and Python.

## **4.3 Results**

### **4.3.1 Comparing modeled water stress to observations of drought-impacted area**

Using our dynamic water-stress model for each 30-m pixel across a watershed in central Texas, we found that canopy loss due to drought was greatest in areas of shallow soils, on hillslopes with low values of TCI, and on southwestern-facing aspects (Figure 14). We started with models that only had spatially explicit soil conditions, and then added parameters associated with lateral redistribution and then spatially explicit *PET* driven by radiation and temperature differences attributable to aspect. Spatially distributed inputs, characterizing soil conditions, lateral water flow, and *PET*, all drove patterns of dynamic water stress across the landscape. By increasing model complexity,

modeled dynamic water stress had high spatial concordance with remotely-sensed observations of drought-impacted area (Figure 14).

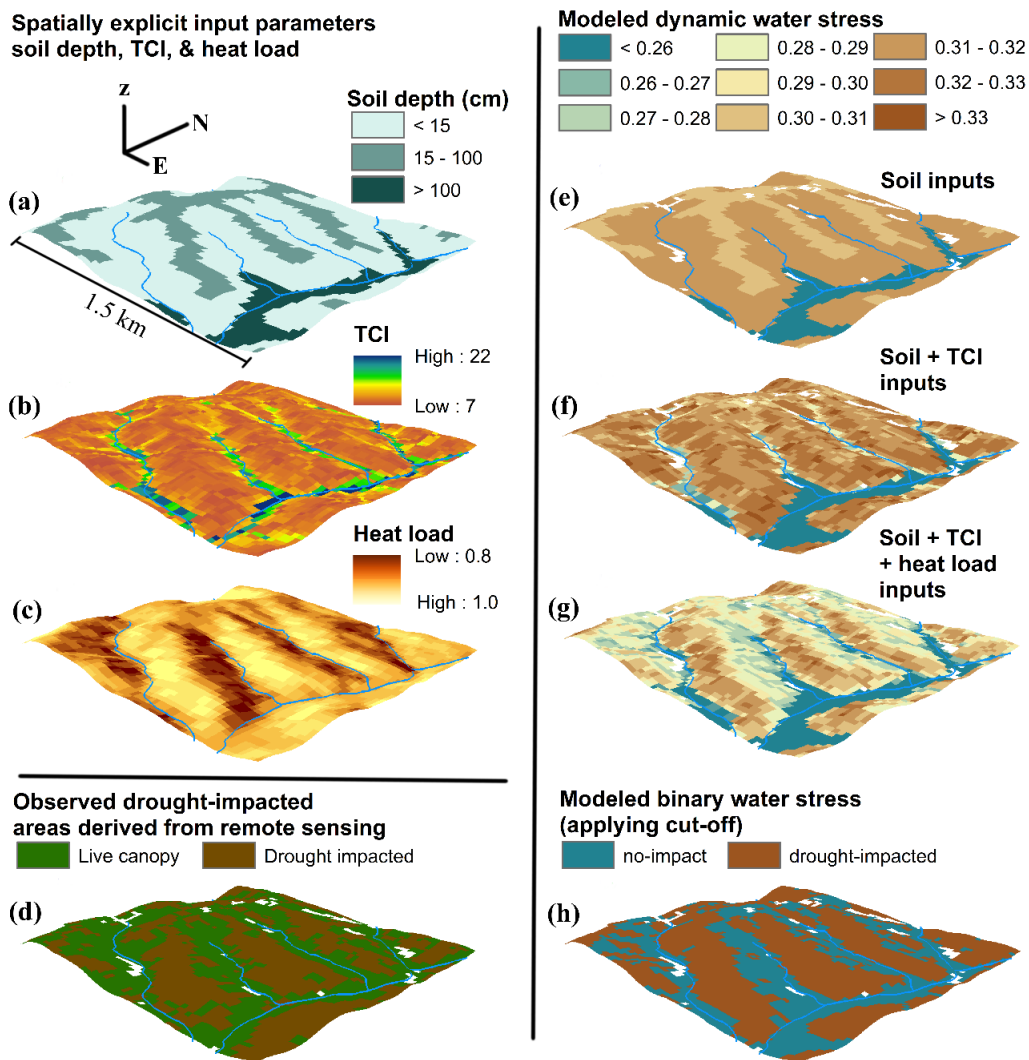
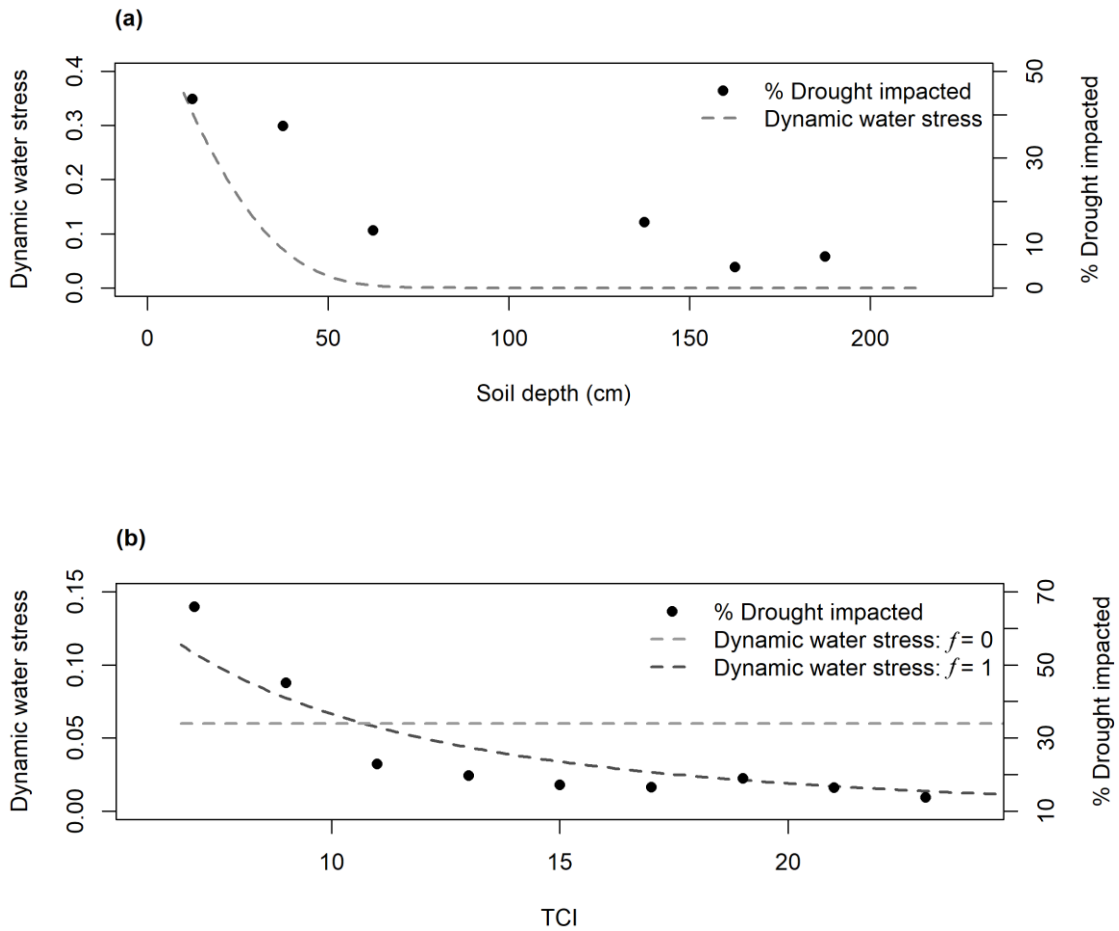


Figure 14: Comparison of spatially explicit input variables of (a) soil depth, (b) topographic compound index (TCI) and (c) heat load index to (d) 30-m remotely sensed drought-impacted area maps. We also present modeled estimates of mean dynamic water stress ( $f = 1$ ) for scenarios including processes specific to (e) heterogeneous soil inputs, (f) lateral redistribution of water using TCI and (g) spatially variable potential evapotranspiration using a heat load index, accounting for radiation and temperature differences attributable to aspect. Using a cutoff value of dynamic water stress (defined in Table 11), we also show binary water stress maps (h), which are directly comparable to observed canopy loss (d).

Modeled dynamic water stress varied across two important environmental gradients. As expected, dynamic water stress decreased with increasing soil depth, as simulated with the following assumptions, a constant clay loam soil texture, constant PET, and no lateral flow of water (Figure 15a). Directly matching model predictions, observations of drought-impacted area also decreased with increasing soil depth. Furthermore, dynamic water stress decreased with increasing values of TCI (Figure 15b). The model was forced using a constant clay loam soil texture and average soil depth. Observations of drought-impacted area aggregated up to 2-unit bins of TCI, also decreased with increasing TCI, following modeled dynamic water stress.



**Figure 15: Modeled dynamic water stress decreased with increasing (a) soil depth and no lateral redistribution ( $f=0$ ) and (b) topographic compound index (TCI, forced with average soil depth and a clay loam soil texture). Modeled results tracked observed drought impacted area (right axis, black circles): in (a) drought-impacted area was aggregated to non-contiguous stands with similar soil properties (e.g., clay loam soil texture with multiple soil depth bins of 25 cm) and in (b) drought-impacted area was binned by 2-units of TCI for areas with clay loam soils.**

To test the accuracy in predicting observed values of canopy loss during the 2011 drought year, we first aggregated modeled results and observed drought-impacted area

in 24 hydrologically similar but non-contiguous stands (Table 10). We compared explanatory power for linear regressions of observations of percent drought-impacted area and four modeled outputs. We found that explanatory power for dynamic water stress increased, as model complexity increased. When only considering spatial variability of soils, adjusted  $R^2$  was equal to 0.76; however, when including lateral flow of water and spatially variable PET from radiation and temperature differences the explanatory power increased to 0.82 (Table 10).

**Table 10: Summary of linear regression coefficients: a comparison of drought-impacted area to model outputs forced with the climate anomalies observed in 2011: dynamic water stress ( $\bar{\theta}$ ), static water stress given a tree was under stress ( $\bar{\zeta}'$ ), the average number of crossings ( $\bar{n}_{sm}$ ) below root P<sub>50</sub> (50% hydraulic conductivity lost), and the average time spent ( $\bar{T}_{sm}$ ) below root P<sub>50</sub>, where  $f = 1$ , and the number of hydrologically similar non-contiguous stands is equal to 24.**

Modeled output	Soils			Soils + LR			Soils + LR + H		
	$R^2$	$\beta$	$p$	$R^2$	$\beta$	$p$	$R^2$	$\beta$	$p$
$\bar{\theta}$	0.76	0.89	***	0.80	0.92	***	0.82	1.00	***
$\bar{\zeta}'$ ,	0.75	0.52	***	0.75	0.52	***	0.76	0.53	***
$\bar{n}_{sm}$	0.77	0.02	***	0.83	0.02	***	0.85	0.03	***
$\bar{T}_{sm}$	0.75	-0.48	***	0.47	-0.37	***	0.45	-0.41	***

\*\*\* = <0.001

Soils = soil texture and depth; LR = lateral redistribution; and H = heat load

Secondly, we tested how well modeled dynamic water stress differentiated spatially contiguous *J. ashei* drought-impacted stands compared with homogenous live

canopy stands. We compared Cragg and Uhler's pseudo  $R^2$  for logistic regressions as well as percent accuracy for a threshold distinguishing the two types of stands using ROC curves (Figure 16, Table 11). We also tested the influence of only including stands above a certain stand size class. There seemed to be an inflection point, where percent accuracy and explanatory power increased dramatically for stands greater than ~1 ha and started to level off at ~2 ha (Figure 16). Also, increasing model complexity resulted in higher accuracy and higher explanatory power. For example, models that only included spatially variable soil conditions reached an accuracy of 60%, when considering stands greater than 2 ha; however, when including spatially variable inputs related to soil, lateral flow of water, and radiation/temperature effects, the accuracy increased to 72% (Table 11). Furthermore, increasing the amount of lateral redistribution of water, by increasing  $f$ , led to improvements in model accuracy and higher explanatory power. However, as  $f$  got larger and approached 1, large changes in  $f$  only led to minimal improvements in accuracy (Figure 16). A cut-off value of 0.29 for dynamic water stress was most successful at distinguishing homogenous live canopy stands from drought-impacted stands (Table 11). We therefore, used this cut-off value as well as  $f = 1$ , to determine the percent of the landscape that surpassed a dynamic water stress value associated with canopy loss for both historical and future climate projections. The cut-off value was not dependent on the size of stands considered (Figure 16c).

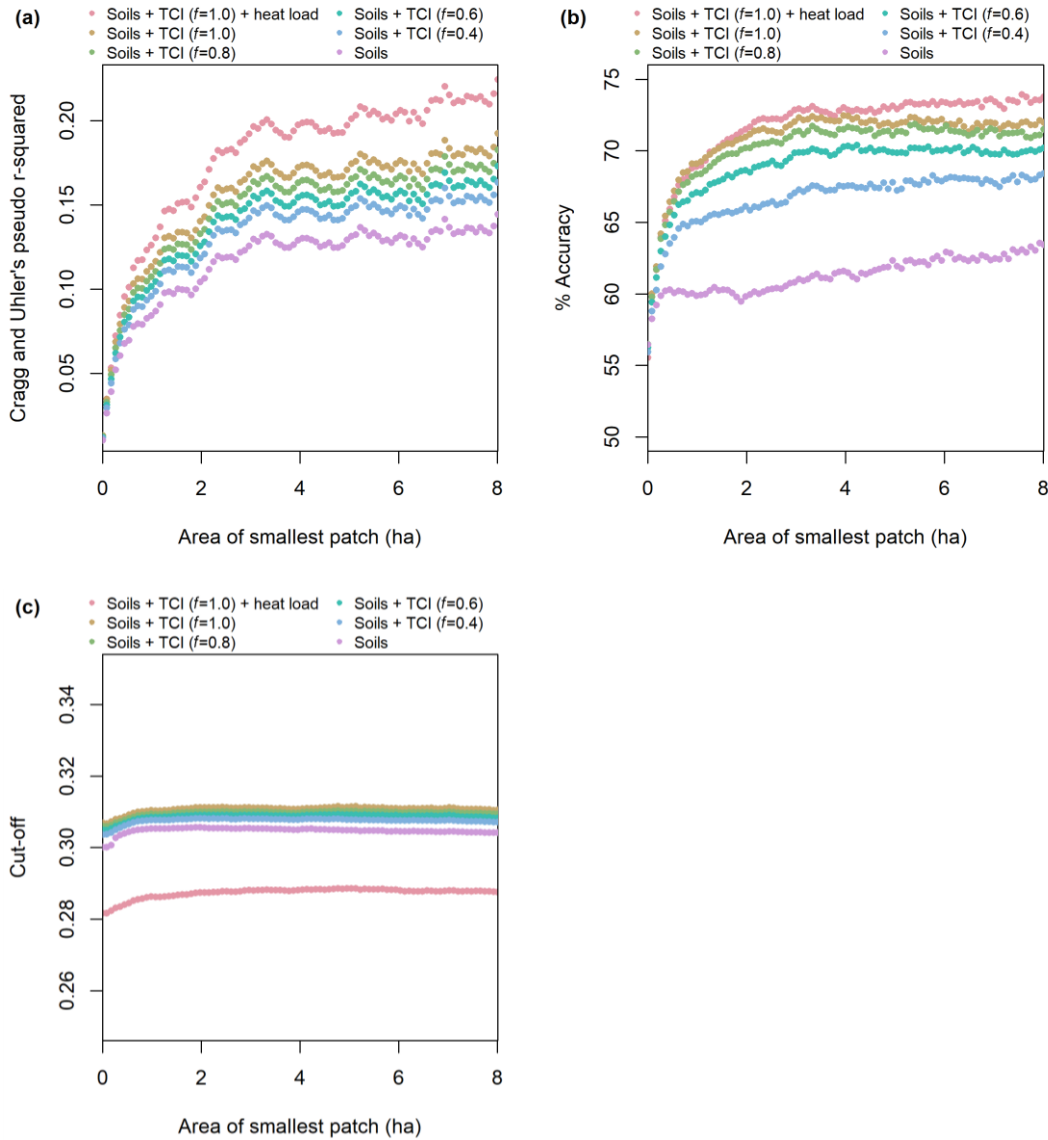


**Figure 16: Accuracy in distinguishing drought-impacted stands from homogenous live canopy stands of *J. ashei* above a certain size threshold (x-axis): (a) Cragg and Uhler's pseudo  $R^2$  for logistic regressions, (b) percent accuracy and (c) the dynamic water stress cutoff defined using receiver operating characteristic (ROC) curves. Each line represents a different model with multiple levels of complexity, including only spatially variable soil conditions (soils), lateral redistribution of water (soils + TCI) with the constant,  $f$ , ranging from 0.4, 0.6, 0.8, and 1.0, and spatially variable PET due to radiation/temperature differences (soils + TCI + heat load). The number of stands ranged from ~42,000 when including all size patches to ~1,000 when including only patches greater than 8 ha.**

**Table 11: Summary of logistic regression coefficients and outputs of the ROC curve analysis for models of increasing complexity, testing the capacity of model outputs in distinguishing drought-impacted stands from homogenous live canopy stands. Model outputs included dynamic water stress ( $\bar{\theta}$ ), static water stress given a tree was under stress ( $\bar{\zeta}'$ ), the average number of crossings ( $\bar{n}_{sm}$ ) below root P<sub>50</sub> (50% hydraulic conductivity lost), and the average time spent ( $\bar{T}_{sm}$ ) below root P<sub>50</sub>, where  $f = 1$ , and the size of drought-impacted or homogenous live canopy stands of *J. ashei* was either greater than 1 ha or greater than 2 ha.**

<i>Modeled output</i>	Soils				Soils + LR				Soils + LR + H				
	<i>R</i> <sup>2</sup>	<i>p</i>	<i>AIC</i>	% <i>acc</i>	<i>R</i> <sup>2</sup>	<i>p</i>	<i>AIC</i>	% <i>acc</i>	<i>R</i> <sup>2</sup>	<i>p</i>	<i>AIC</i>	% <i>acc</i>	<i>Cut-off</i>
<b>&gt;1 ha</b>													
$\bar{\theta}$	0.08	***	7715	60	0.11	***	7577	69	0.13	***	7515	69	0.29
$\bar{\zeta}'$ ,	0.08	***	7717	60	0.09	***	7711	60	0.09	***	7686	62	0.68
$\bar{n}_{sm}$	0.08	***	7718	59	0.13	***	7516	70	0.14	***	7443	69	10.58
$\bar{T}_{sm}$	0.08	***	7722	40	0.01	***	8054	59	0.01	***	8070	59	9.43
<b>&gt;2 ha</b>													
$\bar{\theta}$	0.10	***	4570	60	0.14	***	4466	71	0.16	***	4406	72	0.29
$\bar{\zeta}'$ ,	0.10	***	4574	60	0.10	***	4569	60	0.11	***	4545	64	0.68
$\bar{n}_{sm}$	0.10	***	4573	59	0.16	***	4423	71	0.18	***	4352	72	10.66
$\bar{T}_{sm}$	0.10	***	4577	40	0.01	***	4822	59	0.01	***	4834	59	9.43

\*\*\* = <0.001

Soils = soil texture and depth; LR = Lateral redistribution using TCI; and H = heat load  
*R*<sup>2</sup> = Cragg and Uhler's pseudo r-squared

% *acc* = percent accuracy in differentiating drought-impacted vs. live canopy stands using receiver operating characteristic (ROC) curve analysis and 10-fold cross validation

### 4.3.2 Projecting dynamic water stress through the 21<sup>st</sup> century

To understand how dynamic water stress was projected to change in the future, we selected 10 GCMs that showed the lowest MAE in predicting mean annual precipitation (Table 21, appendix C). For several years and for several of the GCMs, the mean rainfall depth,  $\alpha$ , and the time between rainfall events,  $1/\lambda$ , surpassed drought conditions that were more severe than the 2011 drought year (Figure 17a,b).

Furthermore, *PET* for *J. ashei* increased dramatically compared to historical averages for both RCP 4.5 and even more so for RCP 8.5 (Figure 17c). Ensemble means of dynamic water stress across 10 GCMs, showed that average dynamic water stress increased over the 21<sup>st</sup> century (Figure 18a) for both RCP 4.5 and 8.5 scenarios. Furthermore, the percentage of the landscape surpassing a threshold of dynamic water stress associated with mortality increased through the 21<sup>st</sup> century (Figure 18b).

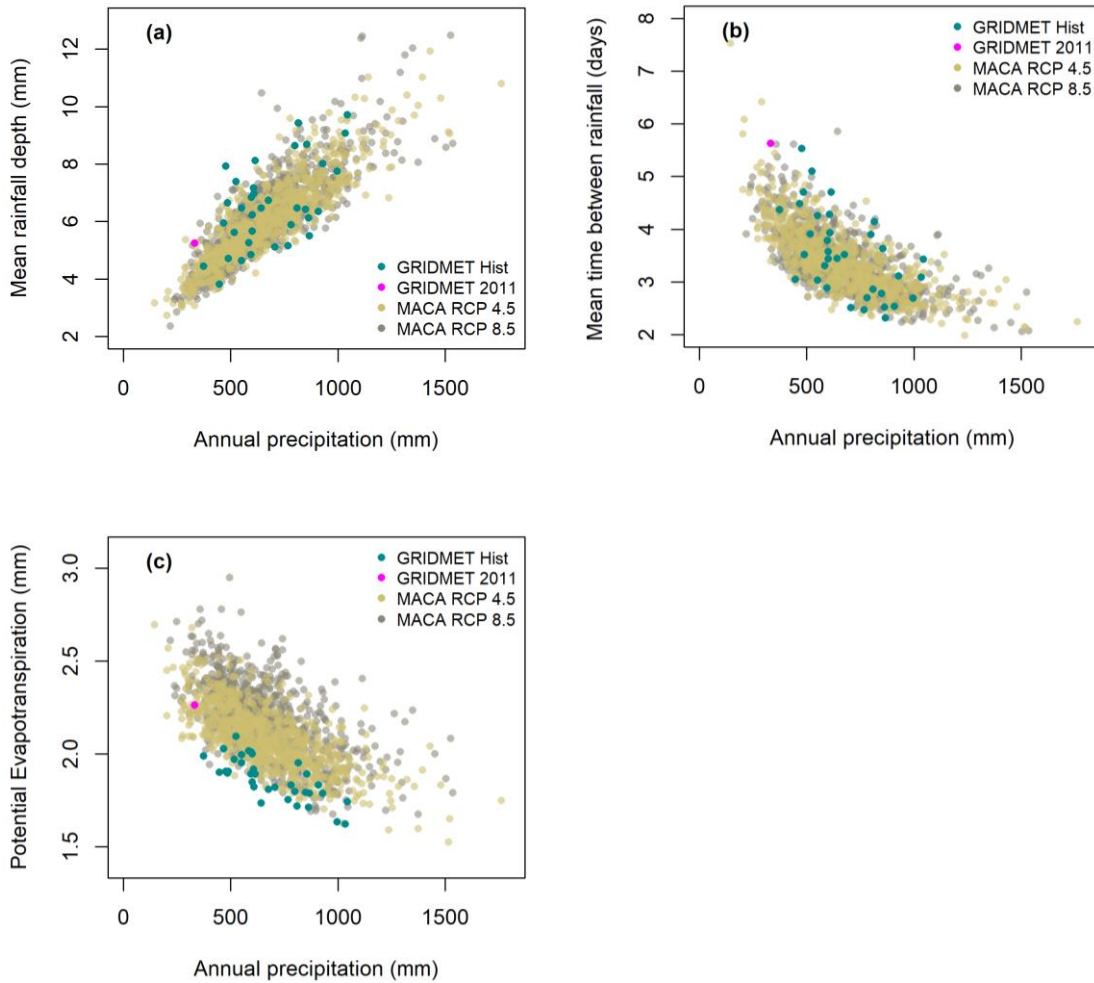


**Figure 17: Comparison of how climate parameters vary with annual precipitation: (a)  $\alpha$ , mean rainfall depth (mm), (b)  $1/\lambda$ , time (days) between rainfall events, and (c) PET, potential evapotranspiration for *J. ashei*, using spatial averages across all areas in the watershed. We include both historical gridMET climate data: 1980-2016 (Abatzoglou, 2013) and future MACA climate projections: 2020-2099, from two representative concentration pathway trajectories, RCP 4.5 and 8.5, acquired from Abatzoglou & Brown, (2012). Each point represents climate parameters for each year from 2020-2099, for each of the 10 general circulation models (GCMs).**

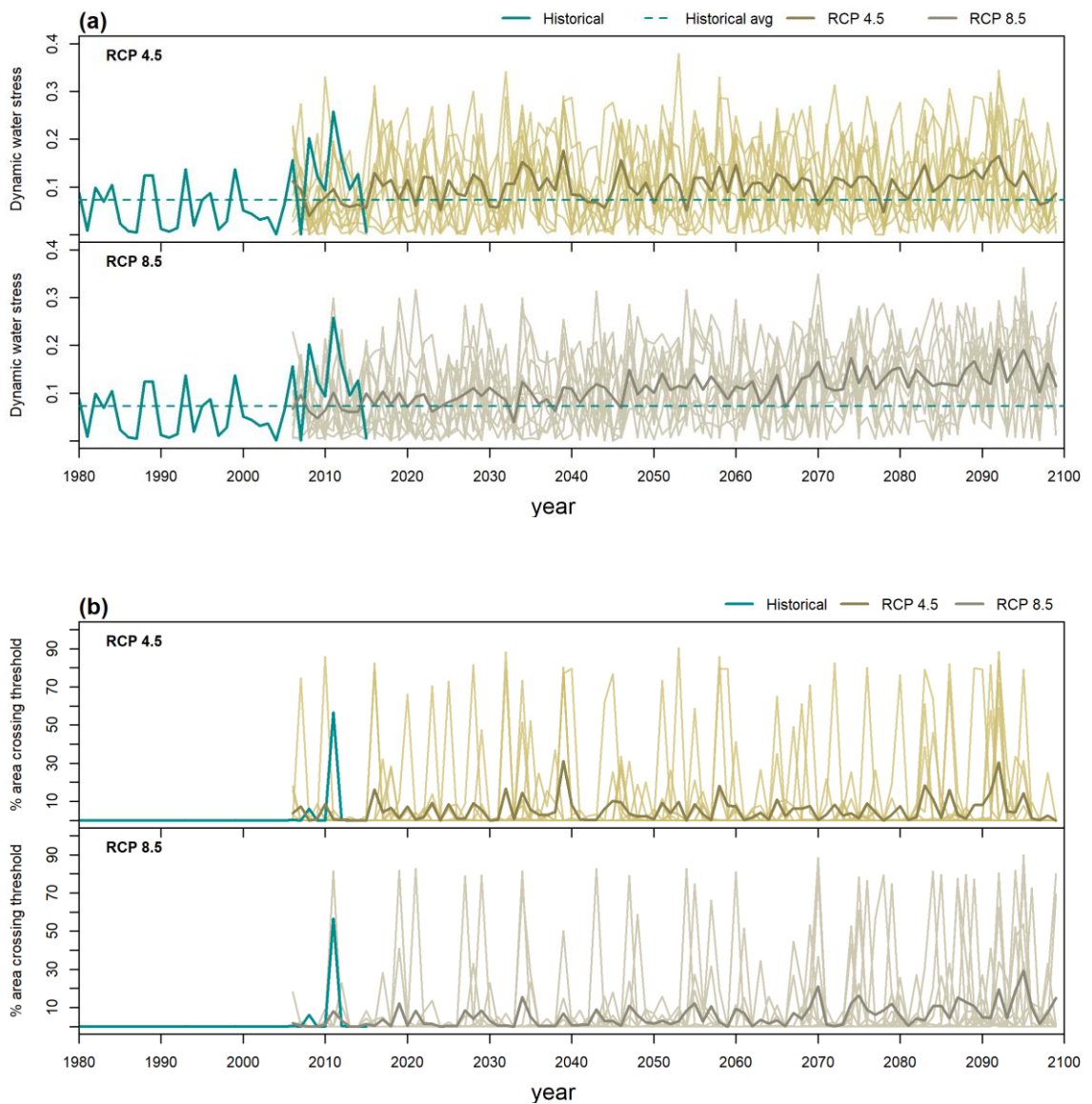


**Figure 18: Comparison of how dynamic water stress has changed over the past 30+ years (1980-2016) (Abatzoglou, 2013) and was projected to change in the future 2006-2099, using climate data from two representative concentration pathway trajectories, RCP 4.5 and 8.5 (Abatzoglou & Brown, 2012): (a) spatial averages of dynamic water stress across the watershed with *Juniperus ashei* cover and (b) percent area drought-impacted (e.g., percentage of the landscape that surpassed the dynamic water stress threshold of 0.29 associated with canopy loss during the 2011 drought year, defined in Table 11). Each of the 10 general circulation models is presented as well as the average (darker line).**

The average percent of the landscape crossing a mortality threshold in the future was lower for models forced with no landscape heterogeneity (<1% for both RCP 4.5 and 8.5 trajectories) compared to models with landscape heterogeneity (~5% for both RCP 4.5 and 8.5, Table 12). Models forced using average conditions across the watershed (no landscape heterogeneity), predicted that less of the watershed would surpass mortality thresholds. On the other hand, for models forced using no landscape heterogeneity the maximum percent of the area impacted by model construction was 100% for the most severe droughts projected in the 21<sup>st</sup> century. However, when including landscape heterogeneity, the maximum percent area impacted in the future was ~90% for both RCP 4.5 and 8.5.

**Table 12: Comparison of future water stress projections of dynamic water stress for models with and without landscape heterogeneity, compiling dynamic water stress across 10 model runs, each forced with climate projections from 10 general circulation models from 2006-2099, and two representative concentration pathways (RCP), 4.5 and 8.5.**

	Landscape heterogeneity	No landscape heterogeneity
<b>RCP 4.5</b>		
<i>Dynamic water stress</i>		
Mean	0.101	0.037
standard deviation	0.080	0.059
range	[0.000, 0.379]	[0.000, 0.368]
<i>% landscape past threshold</i>		
mean	5.5%	0.6%
standard deviation	16.9%	8.0%
range	[0%, 90.5%]	[0%, 100%]
# crossings at 100%	0	6
<b>RCP 8.5</b>		
<i>Dynamic water stress</i>		
mean	0.109	0.040
standard deviation	0.078	0.057
range	[0.000, 0.363]	[0.000, 0.343]
<i>% landscape past threshold</i>		
mean	5.4%	0.2%
standard deviation	16.2%	4.6%
range	[0%, 89.9%]	[0%, 100%]
# crossings at 100%	0	2

## **4.4 Discussion**

### **4.4.1 Incorporating topography in models of tree water stress**

Model estimates of dynamic water stress compared well with remotely-sensed observations of drought-impacted area from the 2011 drought. When using dynamic water stress to distinguish between drought-impacted stands versus homogenous live

canopy stands greater than 2 ha, we found that accuracy increased from 60% for models including only spatially variable soil conditions to 72% for models considering soils and topography, including lateral redistribution of water using TCI and spatially variable PET attributable to radiation/temperature differences (Table 11). Tai et al. (2017) also found that including topography to approximate lateral redistribution improved predictions of Aspen, *Populus tremuloides*, mortality in Colorado; however, only in topographically convergent low elevation areas. We found that accounting for topography improved predictions of spatial patterns of canopy loss across the landscape. Our approach expands upon Tai et al. (2017), by providing an alternative framework that cohesively integrates plant hydraulics and landscape processes.

When aggregating modeled results to larger stands (> 1 ha, Figure 16), we observed improved accuracy, which could be attributable to hydrological processes acting across pixels. The topographic index, TCI, was used to directly relate the land surface to lateral water flow; however, the land surface may not be the best predictor of below ground processes. As an example, the water table configuration could be smoother than the land surface (Wolock & Price, 1994). Also, the minimum size map delineation for the SSURGO soil database ranges from 0.4 to 4 ha; a much coarser resolution than the 30-m digital elevation maps used to derive TCI. Moreover, soil maps often show sharp unrealistic changes of soil texture and soil depth between neighboring soil polygons (Zhu & Mackay, 2001); aggregating across stands may smooth these

transitions. Lastly, at fine spatial scales, tree mortality could appear stochastic, due to a variety of mechanisms that are not included in most models (e.g., insects and pathogens, harvesting/land management, and plasticity of plant traits). For these reasons, accuracy improved as we aggregated modeled results to larger stands, until a threshold of ~2 ha was reached. Past this threshold of 2 ha, accuracy did not increase substantially. Theoretically, if we aggregated to even larger stands beyond 8 ha (e.g., at the scale of the entire watershed), this would be equivalent to forcing the model with no spatially distributed input variables and accuracy would be reduced.

#### **4.4.2 Limitations**

The modeling framework had a few important limitations. *J. ashei* is an evergreen species; therefore, we defined the growing season as the full year; however, this assumed that vegetation and climatic parameters remained constant throughout the year. Allowing climatic parameters to vary throughout the growing season could improve our ability to model tree water stress (Feng, Dawson, Ackerly, Santiago, & Thompson, 2017; Viola, Daly, Vico, Cannarozzo, & Porporato, 2008). Also, we did not consider water inputs from the deep regolith, which could provide additional sources of water (Fellows & Goulden, 2013). A few *J. ashei* individuals have been observed to access water in caves up to 8-m below the soil surface in central Texas (R B Jackson, Moore, Hoffmann, Pockman, & Linder, 1999). Moreover, when examining tree water stress in the future, we did not consider effects associated with increased water use efficiency

(WUE) from elevated atmospheric CO<sub>2</sub> concentrations. However, an experiment examining the interactive effects between elevated CO<sub>2</sub> and drought, found that elevated CO<sub>2</sub> did not delay time to mortality for two gymnosperm species (Duan et al., 2015). If projected future droughts are too severe and cause complete closure of stomata then the benefit of elevated CO<sub>2</sub> will have no effect on photosynthesis (Franks et al., 2013) and in some species elevated CO<sub>2</sub> can cause changes in plant hydraulics that lead to greater potential for drought stress (Domec, Smith, & McCulloh, 2017). Another limitation affecting our projections of water stress was limited accuracy in forecasted precipitation extremes. Regional processes are often not included in many GCMs, causing projections of precipitation extremes to be less accurate at regional scales (Burke et al., 2006; Jentsch et al., 2007). We also do not account for recovery following drought. Models that can account for both within-watershed spatial patterns of soil moisture as well as growth of vegetation could provide additional insight on the effect of landscape heterogeneity on tree survival and recovery following drought (Tague et al., 2013; S M Vicente-Serrano et al., 2015)

#### **4.4.3 Modeling future tree water stress**

Using projected climate data from 10 GCMs, we found that dynamic water stress was forecasted to increase through the 21<sup>st</sup> century due to both projected increases in PET as well as changes in the timing and amount of rainfall. When comparing models with and without landscape heterogeneity, it is important to consider that landscape

heterogeneity allows for the existence of both stressful (e.g., drier, hotter) and favorable (e.g., wetter, cooler) landscape positions for tree growth. Also, the modulating effect of landscape heterogeneity varies across drought severity. With no landscape heterogeneity, the whole landscape experiences the same level of water stress and it takes a more severe drought to cause stress. Models forced using average conditions, include neither stressful nor favorable landscape positions, and may have less average water stress if droughts are moderate. With landscape heterogeneity, across a gradient of drought severity, some stress appears more readily compared to the uniform landscape, (e.g. in hotter, drier landscape positions even under moderate drought). However, some refugia still remain under the most severe drought. Therefore, the average water stress may be higher with landscape heterogeneity, but the range may be lower due to buffering from cooler, mesic landscape positions during severe drought. We observed these hypothesized patterns when we compared models with and without landscape heterogeneity. When the model was forced with parameters assuming no landscape heterogeneity, then the average percent of the watershed impacted by drought was lower (Table 12). Not all positions of a landscape are equally stressful; therefore, models parameterized using average conditions across large grid cells, have the potential to underestimate future tree vulnerability during moderate droughts. When we included landscape heterogeneity, we found that the landscape did buffer against water stress during very severe droughts projected in the 21<sup>st</sup> century. For

example, the maximum percent of the watershed impacted by drought was lower for models including landscape heterogeneity (Table 12).

By including landscape heterogeneity in models, we identified microrefugia capable of buffering against water stress, allowing tree survival even during the most severe drought projected in the 21<sup>st</sup> century. For this study area, these microsites included areas with deep soil, substantial contributing area, and northeastern-facing aspects. Although, we found that landscape heterogeneity did buffer against water stress; the buffering capacity was small for this watershed. When considering outputs from 10 GCMs across the 21<sup>st</sup> century (2006-2099), the maximum percent area of the watershed surpassing a dynamic water stress threshold associated with canopy loss was 100% for models with no landscape heterogeneity, compared to ~90% for models including landscape heterogeneity (Table 12). For the most severe drought, only ~10% of the landscape did not pass a dynamic water stress threshold associated with tree mortality in 2011. This supports the hypothesis by Allen et al., (2015) that the potential for microsites to buffer may be overwhelmed under the severe droughts and heatwaves projected under climate change. On the other hand, microsites might exist across the landscape that are too small to be adequately captured by the spatially distributed input variables of soil conditions and topography included in this model. For example, the SSURGO soil database does not identify areas with unique soil conditions below the minimum size map delineation of 0.4 to 4 ha. By using finer-scale DEMs and soil maps

we could potentially identify additional microsites, capable of providing buffering against future water stress.

Failure to capture landscape heterogeneity in models could limit our capacity to accurately predict forest response to a changing climate. Tree mortality is often observed across local stress gradients within a species range, rather than at trailing range edges due to shifts in climate (Gitlin et al., 2006). Therefore, when projecting future water stress, it is important to account for the fact that not all landscape positions are equally stressful. For our watershed in central Texas, models only predicted minimal buffering of tree water stress through the 21<sup>st</sup> century. However, different watersheds would likely have different buffering capacities, depending on the landscape complexity. Models including landscape heterogeneity can also be used to determine the likely configuration of surviving stands. Landscape heterogeneity has the potential to act as a stabilizing process, if seeds can disperse from surviving trees (Lloret, Escudero, Iriondo, Martínez-Vilalta, & Valladares, 2012); these sites could then be prioritized for conservation (McLaughlin et al., 2017). However, if droughts become too severe and leave only isolated stands, this isolation may limit dispersion and the potential for a species to migrate to keep pace with changing climate conditions (Gitlin et al., 2006; Hewitt & Kellman, 2004; Lazarus & McGill, 2014).

## **5. Projecting tree species abundance shifts in response to drought across Texas into the 21st century**

### **5.1 Introduction**

Forests are increasingly becoming more vulnerable to drought and heat stress due to a changing climate (C. D. Allen et al., 2010; Clark et al., 2016). With this increase in tree mortality, the species composition of forests is expected to shift. Shifts in species distributions can have large ecological consequences, including changes to biodiversity, net primary production, and biophysics. Typically, “climate-envelope” species distribution models (SDMs) are used to define relationships between climate means and current species distributions. These SDMs are then used to predict species occurrence, persistence, and shifts under changing climate conditions.

Most SDMs, are fit to species independently using univariate models and do not consider relationships between species or how species covary across landscapes. Alternatively, recent studies have taken advantage of joint species distribution models, which use multivariate frameworks to model multiple species jointly with their environment (Clark, Gelfand, Woodall, & Zhu, 2014; Clark et al., 2017; Pollock et al., 2014). For example, Pollock et al., (2014) proposed a joint species distribution model for presence-absence data using a multivariate probit regression model. Clark et al., (2017) went a step further, and proposed a generalized joint attribute model, GJAM, which can account for multiple responses (e.g., species abundance, counts, presence-absence, etc.) simultaneously (Clark et al., 2017). Unlike traditional species distribution models, as a

multivariate model, GJAM, can explain covariation among species that remains after accounting for the environment. This covariation could include species-specific interactions as well as species-specific responses to environmental variables not considered in the model. Typically, these models are validated by testing the model's ability to predict current species ranges and in some cases their past ranges. However, droughts and heat waves have already started to shift the composition of forests. Therefore, we can instead take advantage of observations of canopy loss from recent severe droughts and heatwaves to test whether models can predict recent shifts in species abundance.

Ultimately species distribution shifts occur in pulse events, where trees die from drought and/or heat stress during extreme droughts. Recruitment of the same community may not be possible due to shifts in historical climate regimes. Species compositions may also shift, for example if recovery favors species that resprout (Zeppel et al., 2015). Therefore, it could be advantageous to model dead and live tree basal area simultaneously to more accurately capture shifts in communities. For example, Allen et al (2015) proposed that "climate envelope" species distribution models could be used to predict tree mortality.

Selecting appropriate covariates to model species distributions can be challenging. Instead of only relying on relationships between species abundance and normal climate conditions, it is often useful to consider climatic extremes. As climate

change continues, many recent severe droughts and heatwaves that are currently considered extreme events are projected to be within the range of interannual climate variability in the future (Bahn et al., 2014; Williams et al., 2013), such as the 2011 drought in Texas (Schwantes et al., 2017). Many species are more resilient to highly variable precipitation/heat extremes, whereas others may have lower tolerances to variable climate (C. D. Allen et al., 2010; Niu et al., 2014; Orsenigo, Mondoni, Rossi, & Abeli, 2014). Certain species may also have physiological thresholds or tipping points at which mortality is more likely (Reyer et al., 2015). By including information on the historical climate variability, we can account for species-specific tolerances to extreme events. Fewer studies include climate extremes, even though studies have shown that incorporating climate variability can improve accuracy in predicting species ranges (Zimmermann et al., 2009).

We used a generalized joint attribute model, GJAM (Clark et al., 2017), with a Bayesian framework to model species abundance simultaneously with tree mortality over the past 15 years. Then, using future climate projections under representative concentration pathway 4.5 and 8.5 trajectories, we forecasted changes in species abundance as well as tree mortality through the 21<sup>st</sup> century. Our analysis of shifts in species distributions is unique in that (1) we examined live abundance and mortality simultaneously and (2) we used covariates related to average climate as well as climate extremes.

## **5.2 Methods**

We model species-specific mortality in conjunction with species abundance, using a generalized joint attribute model, GJAM (Clark et al., 2017). We use observations of dead and live basal area by species from ~15,000 USDA Forest Inventory and Analysis plots across Texas, and covariates associated with climate, soils, and topography. We compared model outputs to an independent dataset of remotely sensed canopy loss observations from a severe drought in 2011 (Schwantes et al., 2017, 2016). We also projected future shifts in tree species communities into the 21<sup>st</sup> century.

### **5.2.1. Plot-level data**

To fit the model, we used dead and live abundance observations by species observed in ~15,000 Forest Inventory and Analysis (FIA) plots across Texas, sampled from 2001-2015. FIA data is collected by the United States Department of Agriculture Forest Service. In western Texas, baseline FIA plots are still being established; therefore, we were unable to track plots through time, as only the eastern plots had been re-measured after the drought. Pre- and post- drought plots are independent samples and are not in the same location for western Texas. Each plot is composed of four subplots (each ~1/24<sup>th</sup> of an acre, where all trees  $\geq 5$  inches in diameter are measured). Four smaller microplots are nested within each microplot (each ~1/300<sup>th</sup> of an acre, where trees 1-5 inches in diameter are measured). We aggregated basal area by species to the plot level. We excluded observations of dead trees that occurred due to either vegetation

suppression/competition or land clearing/silviculture. Trees classified as dead due to suppression and/or competition are typically understory shade intolerant trees or saplings that are unlikely to reach maturity.

To protect land owner identities, most plot locations are fuzzed within an approximately 800-m region from the original plot location. Therefore, for environmental variables not collected within the FIA plots, we took spatial averages within an 800-m radius from the fuzzed plot location. To avoid rare species, we only considered species that were observed to be alive in more than 50 plots, 76 species in total. Remaining rare species were then grouped into two 'other' dead or alive categories.

### **5.2.2 Explanatory covariates**

For the climate covariate, we calculated the climatic water deficit, P-PET, as the difference between annual precipitation and annual potential evapotranspiration, using 4-km Gridmet data acquired from (Abatzoglou, 2013). P-PET considers both supply and atmospheric moisture demand (Rind et al., 1990). When precipitation is less than potential evapotranspiration then P-PET is negative and a water deficit occurs. We considered both the mean and standard deviation of annual P-PET from 1980 to the FIA plot's inventory year. For example, if an FIA plot's inventory year was 2001, then the P-PET mean and standard deviation were calculated using climate from 1980-2001.

We also considered local-scale covariates related to soil conditions and topography. Elevation, slope, and aspect were obtained from the FIA plots directly, whereas spatial averages within an 800-m radius buffer from the plot center were taken for the other environmental variables. Available water storage was directly obtained from the Soil Survey Geographic (SSURGO) database (United States Department of Agriculture, 2014). We computed area- and depth-weighted averages of percent sand, clay, and silt for each soil polygon. We also calculated a heat load index that considered potential direct incident radiation and differences in temperature attributable to steepness of slope and aspect (McCune & Keon, 2002). When fitting the model, we used elevation, slope, and aspect collected on the ground in the plots; however, for spatial predictions across Texas we used elevation, slope and aspect computed from a 30-m void-filled digital elevation model (DEM) from the Shuttle Radar Topography Mission (SRTM; Version 3). We also calculated, the topographic compound index, TCI, which is an index that describes lateral subsurface water flow across landscapes (K. Beven, 1995). As a physically based index of hydrologic similarity, TCI is defined as  $\ln(a_c/\tan(b))$ , where  $a_c$  is the upslope contributing area per unit contour length and  $\tan(b)$  is the local land surface slope. The hydraulic gradient, which is the ability of accumulated water to transfer through a grid cell, can be approximated by the local slope and the lateral discharge, which is the volume of water transferring through a grid cell is expected to be proportional to the upslope contributing area (K. Beven, 1997; Quinn et al., 1995). A

small number (0.001) was added to the denominator of all grid cells, to avoid zero values in the denominator and thus undefined values of TCI. We also tested interactions between the local-scale soil and topographic variables and the climate variables, but none were significant.

To understand how species may shift in response to future climate, we used 4-km projected downscaled climate data acquired from Abatzoglou & Brown, (2012). We selected the general circulation model (GCM), MIROC5, because this GCM showed the lowest mean absolute error in predicting annual historical precipitation from 1980-2005 for our study region. We considered two climate trajectories, representative concentration pathway (RCP) 4.5 and 8.5. We then calculated P-PET mean and standard deviation from 2060-2099 for each scenario.

### 5.2.3. Joint species distribution modeling

We used GJAM (Clark et al., 2017) to relate live and dead basal area to environmental predictors across Texas. As our response variables are continuous abundance data, GJAM takes the form of a multivariate Tobit,

$$y_{is} = \begin{cases} w_{is}, & w_{is} > 0 \\ 0, & w_{is} \leq 0 \end{cases} \quad \text{Equation 5.1}$$

$$w_i | x_i, y_i \sim MVN(B'x_i, \Sigma)$$

where, for each observation ( $i$ ), species ( $s = 1, \dots, S$ ) and covariate ( $q = 1, \dots, Q$ ),  $y_i$  is a vector of responses, where  $y_i = (y_{i1}, y_{i2}, \dots, y_{is})$  and  $x_i$  is a vector of covariates where  $x_i =$

$(x_{i1}, x_{i2}, \dots, x_{iQ})$ . Both dead and live basal area can be reasonably treated as continuous random variables; however, trees cannot have negative basal area. Therefore, the distribution of  $y_{is}$  follows a censored normal distribution censored below zero, and  $w_i$  is the latent continuous variable. Additionally, the covariance  $\Sigma$  represents the covariance between species beyond what has already been explained by the environmental covariates. For model fitting, we use Gibbs sampling for posterior simulation in R (R Core Team, 2015) using the `gjam` package (Clark et al., 2017). We have no prior information, and therefore we selected non-informative priors, with minimal influence on the posterior distribution. Also, in univariate models, we can compare  $\beta$  coefficients to evaluate the importance of each covariate. Alternatively, in multivariate models, following Clark et al., (2017) we can determine the sensitivity ( $f$ ) of the response matrix to each covariate as the diagonal of  $F$ , where  $F$  is defined as,

$$F = B\Sigma^{-1}B'$$

We compare three model runs of variable complexity, in order to show the importance of (1) including a covariate related to climate variability (e.g., P-PET standard deviation) and (2) modeling live basal area and mortality simultaneously. Firstly, most species distribution models only use covariates related to average climate conditions, therefore, for Model A, we define the response matrix as live basal area only and define the base model covariates as: mean P-PET, elevation, heat load, topographic compound index, percent sand, percent clay, and available water storage. Secondly, for

Model B, we add in a covariate related to climate variability, the P-PET standard deviation. Thirdly, for Model C, we define the response matrix as live and dead basal area, and use the same covariates as Model B. We spatially predict tree abundance across Texas at a 4-km spatial resolution, and then compare our model projections to the drought-impacted areas observed during the 2011 drought, using remote sensing (Schwantes et al., 2017, 2016). We present results for 4-km grid cells with >25% forest cover as defined as ecological systems where the dominant species were trees using an ecological systems map of Texas (Comer et al., 2003; Elliott et al., 2014).

### **5.3 Results**

Of the 30 most dominant species across Texas, many of the eastern hardwoods had the most mortality (10-17% loss in basal area) over the past 15 years, including *Quercus stellata*, *Q. nigra*, *Pinus echinata*, *Q. falcata*, *Q. phellos*, *Ulmus Americana*, *P. elliotii*, *Q. laurifolia*, *Q. marilandica* (Table 13). The dominant species with the least basal area lost was *Juniperus coahuilensis* with only 1.1% loss observed.

**Table 13: Basal area and percent loss in basal area for the 30 most dominant species in Texas, aggregated across the FIA plots.**

Symbol	Basal area (m <sup>2</sup> )	Percent loss in basal area	Species
PITA	18034	4.4%	<i>Pinus taeda</i>
PRGL2	7076	5.0%	<i>Prosopis glandulosa</i>
JUAS	5606	4.8%	<i>Juniperus ashei</i>
LIST2	4449	5.3%	<i>Liquidambar styraciflua</i>
QUST	3894	10.3%	<i>Quercus stellata</i>
QUNI	2956	10.2%	<i>Quercus nigra</i>
QUVI	2635	5.7%	<i>Quercus virginiana</i>
PIEC2	2233	11.9%	<i>Pinus echinata</i>
QUFA	1647	13.6%	<i>Quercus falcata</i>
ULAL	1468	5.6%	<i>Ulmus alata</i>
JUPI	1343	5.1%	<i>Juniperus pinchotii</i>
ULCR	1089	7.0%	<i>Ulmus crassifolia</i>
QUPH	1063	11.2%	<i>Quercus phellos</i>
CELA	988	6.2%	<i>Celtis laevigata</i>
NYSY	928	4.1%	<i>Nyssa sylvatica</i>
JUVI	876	7.6%	<i>Juniperus virginiana</i>
QUAL	842	6.6%	<i>Quercus alba</i>
FRPE	806	8.1%	<i>Fraxinus pennsylvanica</i>
TRSE6	772	5.7%	<i>Triadica sebifera</i>
QUPA5	611	9.8%	<i>Quercus pagoda</i>
ACRU	547	7.6%	<i>Acer rubrum</i>
ULAM	534	11.9%	<i>Ulmus americana</i>
JUCO11	514	1.1%	<i>Juniperus coahuilensis</i>
PIEL	475	11.5%	<i>Pinus elliottii</i>
TADI2	472	5.2%	<i>Taxodium distichum</i>
QULA3	466	13.0%	<i>Quercus laurifolia</i>
QUMA3	412	17.1%	<i>Quercus marilandica</i>
CAIL2	397	9.3%	<i>Carya illinoensis</i>
QULY	366	8.0%	<i>Quercus lyrata</i>
CACA18	340	9.3%	<i>Carpinus caroliniana</i>

For Model C, which considers both dead and live basal area, a sensitivity analysis demonstrated that mean/historical climatic water deficit, calculated from 1980 to the inventory year of the plot, as well as elevation had stronger effects on the response compared to covariates related to soil conditions (e.g., available water storage and soil texture) and landscape position (e.g., heat load, and a topographic compound index) (Figure 19a). When considering only live basal area in the response matrix, P-PET variability (standard deviation) was the 6<sup>th</sup> most important covariate (Figure 19b Model B); however, when considering both alive and dead basal area P-PET variability became slightly more important (Figure 19a). When only fitting the model to dead basal area, available water storage was the most important covariate and P-PET variability was the second most important (Figure 19c).

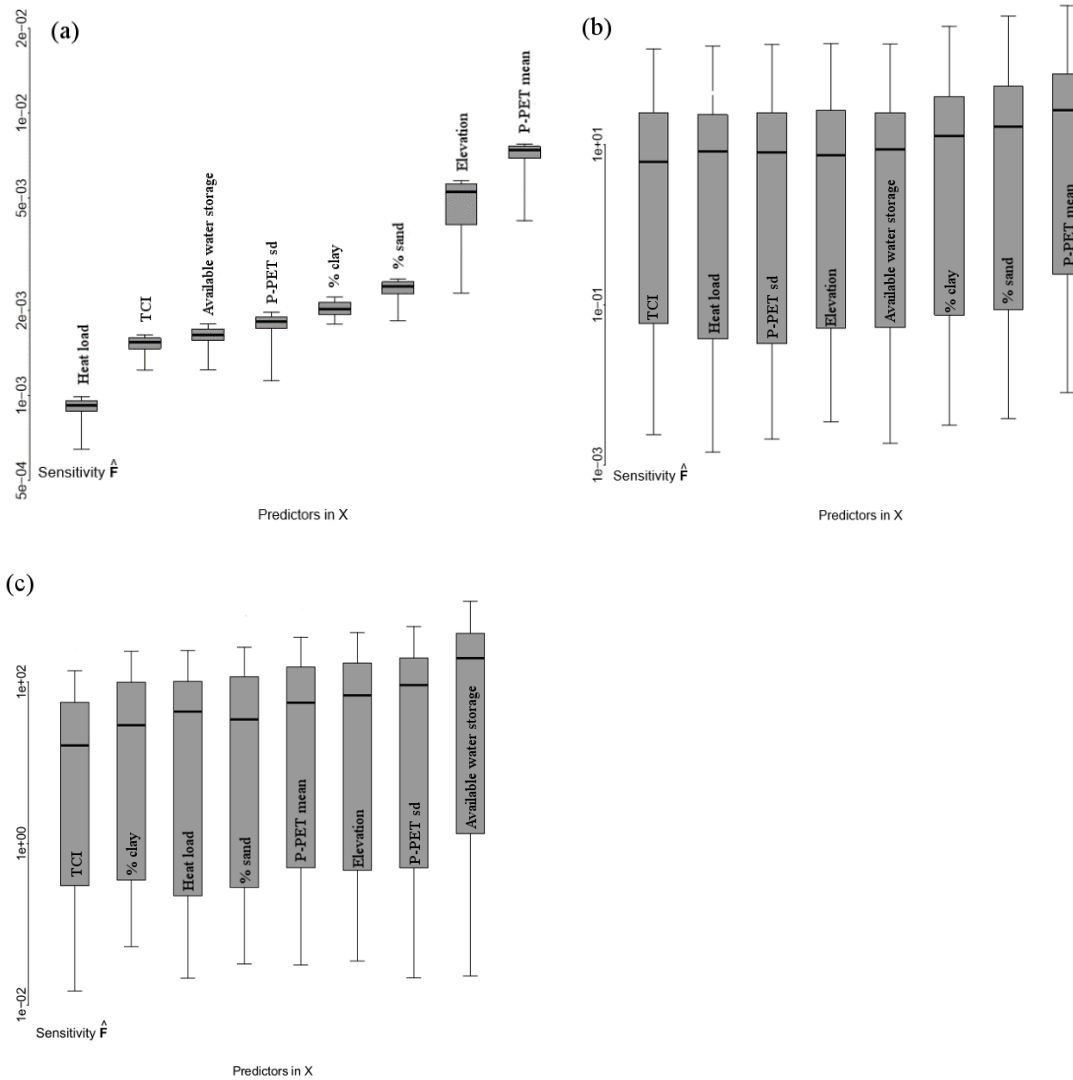


**Figure 19: Sensitivity coefficients ( $\hat{f}$ ) for covariates where the response matrix included (a) dead and live basal area, Model C (b) only live basal area, Model B and (c) only dead basal area. Higher values indicate covariates with stronger effects (e.g., covariates that account for more of the variation in the response). Covariates include: % sand, % clay, available water storage, elevation, topographic compound index (TCI), heat load, and climatic water deficit (P-PET) standard deviation (sd) and historical mean.**

In general  $\beta_{sq}$  represents the main effect of changing  $x_q$  on the latent variable  $w_s$ .

Examining the  $\beta$  coefficients for the covariate available water storage (Figure 20a) for the

final model (Model C), we observed that greater dead and live basal area was associated with lower available water storage for species like *Juniperus ashei* (JUAS), a drought-tolerant tree that typically grows in shallow soils. On the other hand, greater dead and live basal area for *Prosopis glandulosa* (PRGL2) was associated with high available water storage. *P. glandulosa* typically grows on deep sandy soils.  $\beta$  coefficients for both dead and live basal area are linked for these species, because mortality only occurs in areas where the species are present. Alternatively, for climatic water deficit (P-PET) variability (Figure 20b), higher dead basal area for many species were associated with greater variability in the climatic water deficit. Higher values of P-PET variability indicate potentially greater water stress over the period from 1980 to the inventory year of the FIA plot. For example, the beta coefficient for live basal area of *Quercus incana* (QUIN) was negatively associated with P-PET variability, whereas dead basal area for *Q. incana* was positively associated with P-PET variability. A year with higher precipitation would also lead to increased variability in P-PET, which is likely why not all species followed this trend.



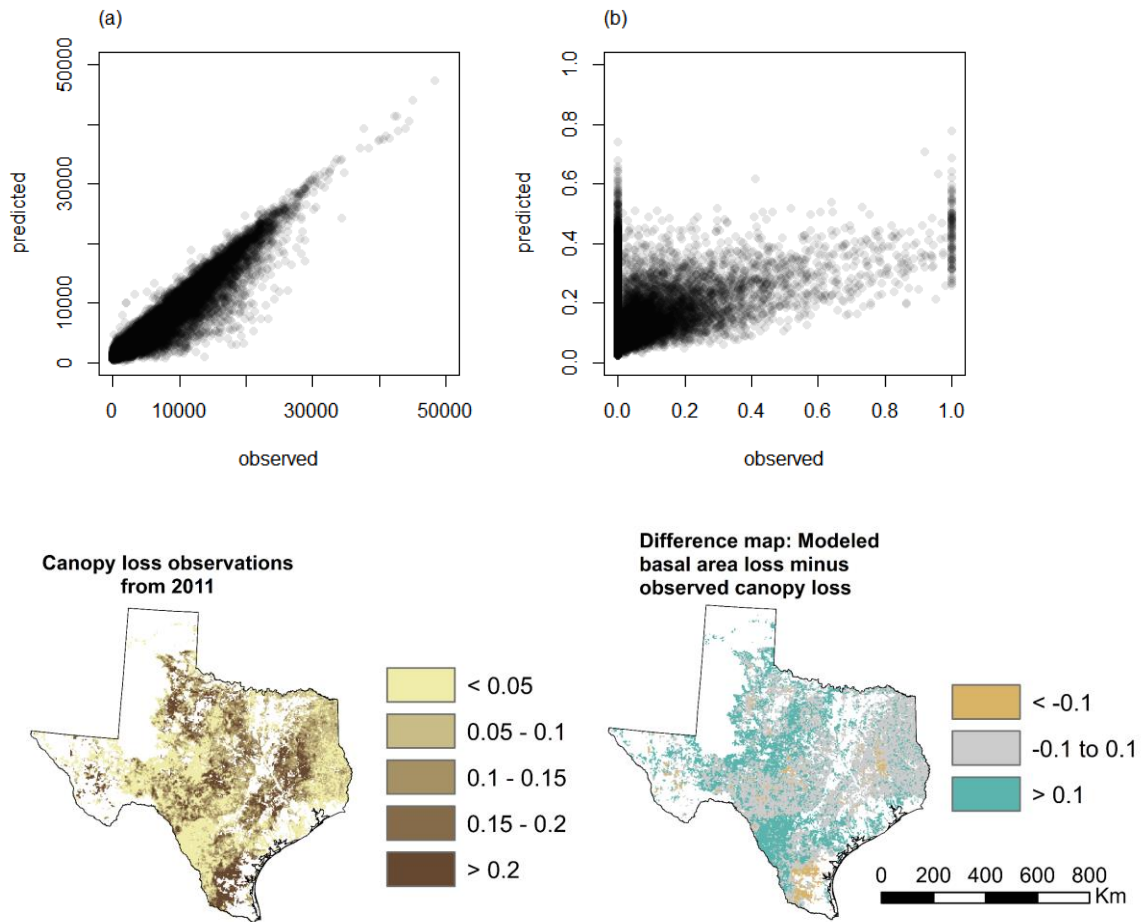


**Figure 21: In-sample prediction of (a) total live abundance and (b) percent basal area loss compared to observed values in FIA plots for Model C. Remotely sensed derived drought-impacted area maps were also compared to modeled percent basal area loss (bottom right), where blue indicates areas where loss was overpredicted by the model, and orange indicates areas where loss was underpredicted.**

Model C included dead and live basal area in the response matrix, and therefore, we could directly predict percent basal area loss, which showed high spatial congruence with canopy loss observed during the 2011 drought in many regions across Texas

(Figure 21). Covariate and response matrix selection also affected the projections of shifts in abundance under RCP 4.5 and 8.5. For example, the projections of abundance were similar for Model A and B; however, when dead and live basal area were modeled simultaneously (Model C), there was a larger increase in abundance of basal area across Texas, under RCP 8.5. Also, examining percent basal area loss predicted under Model C, there was greater loss projected in the eastern hardwoods, for RCP 8.5 compared to RCP 4.5, Figure 22.

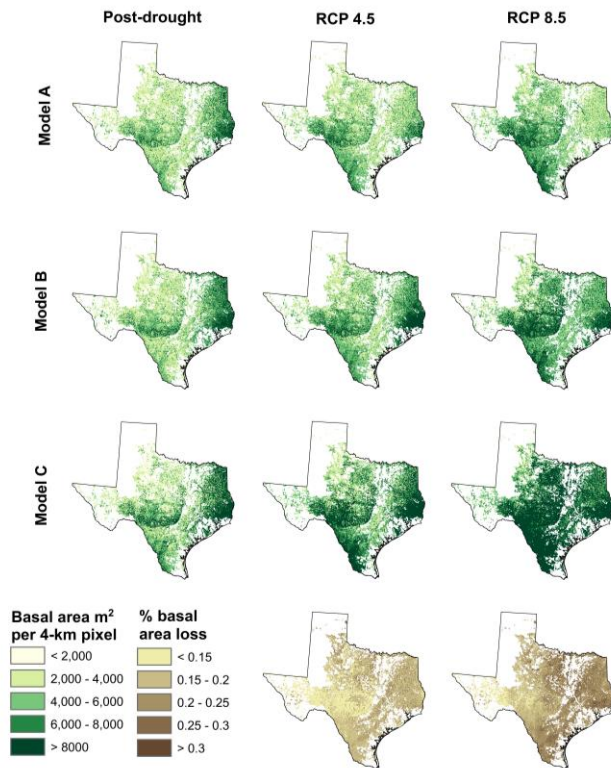


**Figure 22: Percent loss of basal area projected for general circulation model, MIROC5, under two representative concentration pathways 4.5 and 8.5 from 2060-2099, with covariates related to Model A: the base model, Model B: the base model and climatic water deficit P-PET variability and Model C: the base model and P-PET variability, while also simultaneously modeling both live and dead basal area as the response.**

Model C indicated that the eastern hardwood species were expected to decrease in abundance, under both RCP 4.5 and 8.5 (Table 14), such as *Pinus taeda*, *Pinus echinata*, and *Liquidambar styraciflua*. On the other hand, the western woodland/shrubland species were expected to become more dominant, including *Juniperus ashei*, *Prosopis glandulosa*, *Quercus virginiana*, and *Juniperus pinchotii* (Table 14). As an example, Figure 23 shows the retraction of the range for *Q. nigra*, under RCP 8.5, as well as the expansion of the range for *J. pinchotti*. Furthermore, we also classified the dominant species predicted for each 4-km grid cell as either a woodland or forest tree species, as defined by the FIA. Examining the projected trends, we see an expansion of dominant tree species that are classified as woodland/shrubland species under RCP 4.5 and 8.5, compared to current (post-drought, 2015) climate conditions (Figure 24).

**Table 14: Projected decreases (in bold) vs increases in basal area from the baseline (current, 2015, post-drought climate) compared to 2060-2099 climate conditions under representative concentration pathway, RCP, 4.5 and 8.5 trajectories, for 30 abundant species across Texas.**

Id	Basal area 2015 (10 <sup>5</sup> m <sup>2</sup> )	Projected change in basal area		Species
		RCP 4.5 (10 <sup>5</sup> m <sup>2</sup> )	RCP 8.5 (10 <sup>5</sup> m <sup>2</sup> )	
JUAS	230.8	83.3	204.6	<i>Juniperus ashei</i>
PITA	195.4	<b>-1.7</b>	<b>-54.1</b>	<i>Pinus taeda</i>
PRGL2	190.7	114.6	182.9	<i>Prosopis glandulosa</i>
QUVI	123.7	89.7	278.8	<i>Quercus virginiana</i>
QUST	75.3	6.8	14.6	<i>Quercus stellata</i>
JUPI	50.4	54.5	126.4	<i>Juniperus pinchotii</i>
PIEC2	49.9	<b>-4.1</b>	<b>-15.2</b>	<i>Pinus echinata</i>
LIST2	47.6	<b>-8.0</b>	<b>-26.8</b>	<i>Liquidambar styraciflua</i>
ULAL	34.3	0.0	<b>-1.9</b>	<i>Ulmus alata</i>
QUNI	31.9	2.4	<b>-5.1</b>	<i>Quercus nigra</i>
CELA	24.6	9.0	22.6	<i>Celtis laevigata</i>
ULCR	22.6	19.8	56.9	<i>Ulmus crassifolia</i>
QUPH	22.2	<b>-4.0</b>	<b>-14.9</b>	<i>Quercus phellos</i>
QUFA	19.0	<b>-4.8</b>	<b>-10.1</b>	<i>Quercus falcata</i>
DITE3	17.3	51.8	199.0	<i>Diospyros texana</i>
JUVI	17.1	9.4	22.6	<i>Juniperus virginiana</i>
FRPE	17.0	<b>-0.4</b>	<b>-2.2</b>	<i>Fraxinus pennsylvanica</i>
QUAL	15.4	<b>-3.7</b>	<b>-12.4</b>	<i>Quercus alba</i>
SANI	13.9	<b>-0.5</b>	<b>-0.5</b>	<i>Salix nigra</i>
ACFA	12.7	32.8	142.5	<i>Acacia farnesiana</i>
TRSE6	11.1	7.0	3.7	<i>Triadica sebifera</i>
NYSY	10.0	<b>-3.6</b>	<b>-8.5</b>	<i>Nyssa sylvatica</i>
JUCO11	9.6	<b>-1.9</b>	<b>-5.1</b>	<i>Juniperus coahuilensis</i>
COHO	8.9	29.8	139.0	<i>Condalia hookeri</i>
QUMA3	8.8	<b>-0.7</b>	<b>-1.4</b>	<i>Quercus marilandica</i>
QUBU2	8.6	2.9	10.4	<i>Quercus buckleyi</i>
ULAM	8.2	<b>-0.4</b>	<b>-1.1</b>	<i>Ulmus americana</i>
QUPA5	7.3	<b>-0.1</b>	<b>-2.8</b>	<i>Quercus pagoda</i>
ACRU	6.6	<b>-3.6</b>	<b>-6.3</b>	<i>Acer rubrum</i>

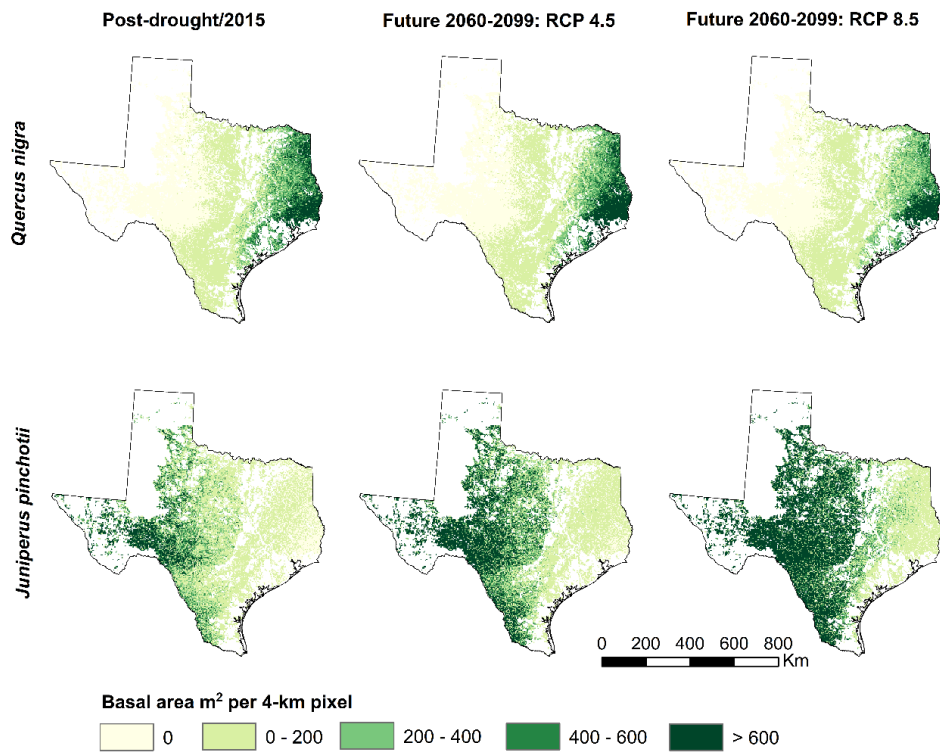
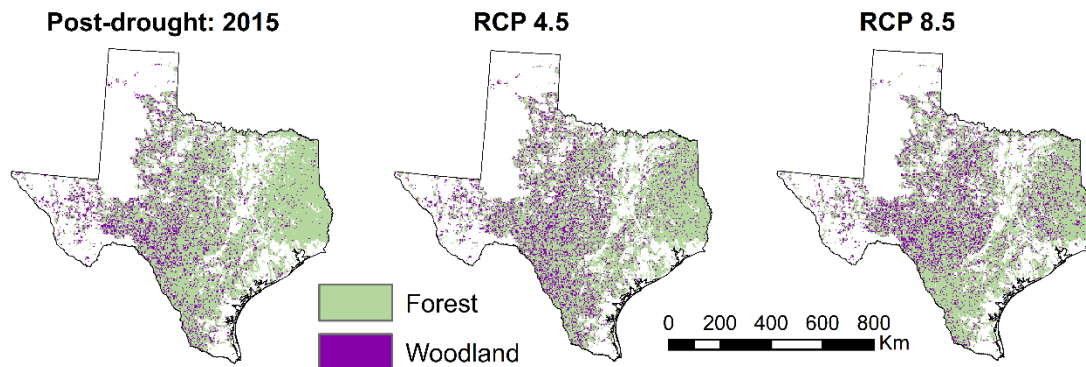


Figure 23: Comparison of species-specific abundance (basal area) for two species: water oak, *Quercus nigra* (top) and redberry juniper, *Juniperus pinchottii* (bottom), across three climate regimes: post-drought (2015, current conditions) and future climate under representative concentration pathway (RCP) 4.5 and 8.5 using the MIROC5 general circulation model.



**Figure 24: Change in forest vs. woodland dominant tree species from current 2015, post-drought climate to future climate projected from 2060-2099 using the MIROC5 general circulation model and considering two representative concentration pathways (RCP) 4.5 and 8.5.**

## **5.4 Discussion**

We found that by modeling both live and dead basal area jointly with their environment we could predict shifts in tree species abundance due to a recent severe drought in 2011. In this analysis, we used a joint species distribution model with a Bayesian framework and observations of dead and live basal area from FIA plots across Texas, to model current species abundance as well as tree mortality over the past 15 years. We then compared remotely-sensed drought-impacted area observations from the 2011 drought to post-drought model projections of tree basal area loss. We also used multiple climate warming scenarios to forecast future tree composition shifts and to determine which tree species may be most vulnerable to climate change. Lastly, we

discussed how projected shifts in abundance depend on the covariates selected and the types of responses included.

Overall, we found that the eastern hardwoods were expected to shift farther eastwards as a result of climate change, and that shrubland and woodland species were expected to become increasingly dominant throughout Texas. For example, species like *Juniperus pinchottii* were projected to increase their range, whereas species like *Q. nigra* were projected to have range retractions (Figure 23). Other studies have also projected a transition from forest to savanna-type ecosystems for the southeastern United States under the more severe climate scenarios (Bachelet, Neilson, Lenihan, & Drapek, 2001; Clark, Bell, Kwit, & Zhu, 2014). However, it's important to consider that other factors, in addition to climate, control the amount of woody biomass in a savanna ecosystem, such as fire and herbivory (van Langevelde et al., 2003).

By overlaying an ecological systems layer with the canopy loss maps derived from remote sensing, we observed that ecological systems dominated by *J. ashei* were some of the most drought-impacted systems in 2011 (Schwantes et al., 2017), whereas, within the FIA dataset, we only observed a 4.8% reduction in *J. ashei* basal area over the past 15 years (Table 13). Moore et al., (2016) also observed mortality of *J. ashei* in central Texas in field plots sampled in 2012 across Texas. Studies have observed that *J. ashei* is unlikely to resprout following fire disturbances (Andruk, Schwoppe, & Fowler, 2014). However, following the 2011 drought in Texas approximately 10% of *J. ashei* with crown

death from drought resprouted (Crouchet, 2016). Many of the FIA plots were sampled several years after the 2011 drought in comparison to directly after the drought in Moore et al., (2016). Therefore, perhaps *J. ashei* appeared dead in remotely sensed imagery (e.g., because the majority of the canopy was lost), but this species actually had resprouts, and were thus considered alive in the FIA plots. We know that resprouting species are more likely to survive a drought disturbance compared to species that do not resprout (Bond & Midgley, 2001; Zeppel et al., 2015). Therefore, although we observed significant canopy loss of *J. ashei* in our remote sensing analysis, *J. ashei* will likely be able to persist and even expand as our model projects in this chapter, because it can resprout after drought-disturbances. An important limitation of the FIA data, is that the plot design and sampling was originally designed for forest ecosystems, so there may also be fewer shrubs/woodland species counted, and thus less knowledge of how these shrubland/woodland species may respond to drought.

We also show the importance of including climate variability when projecting changes in species distributions to climate change. Extreme droughts, which are often coupled by extreme heatwaves (AghaKouchak et al., 2014), can lead to rapid die-off events and significant changes in species compositions in pulses. Without including covariates related to climate variability, models may fail to capture these mortality events. For example, when we only used normal climate conditions and local-scale predictors of tree abundance, we could not predict changes in abundance observed

during the 2011 drought. Therefore, SDMs trained exclusively using average climate conditions and average projections of future climates, may fail to capture community level shifts associated with changes in climate variability that are expected to continue with climate change.

We found that it was also important to model both dead and live basal area simultaneously (Model C), because we could confirm that the model could predict percent basal area loss that matched with our canopy loss maps (Figure 21). Interestingly we also noted unique patterns in the  $\beta$  coefficients; for example many of the  $\beta$  coefficients for dead and live basal area by species were tightly linked (Fig 20a). The model was capable of only predicting species-specific mortality in areas where the species was present. For example, increases in dead and live basal area were both associated with decreases in available water storage for *J. ashei*, with the dead basal area having a slightly but not significantly more negative beta value, as expected (Figure 20a). On the other hand, P-PET variability was the only covariate, where dead and live basal area for the same species had  $\beta$  coefficients with different signs. For example, high P-PET variability was associated with higher dead basal area, whereas high live basal area tended to be associated with low P-PET variability.

Compared to altitudinal shifts of trees, fewer studies have looked at latitudinal range retractions (Jump et al., 2009). Populations at trailing range edges can experience increased drought stress and susceptibility to pests and disease (C. D. Allen & Breshears,

1998; Jump et al., 2009). For example, Allen & Breshears, (1998) observed a 2 km ecotone shift in the ponderosa pine forest in Northern New Mexico during the 1950s drought. Ponderosa pine has not returned despite favorable climatic conditions within this region. We also, observed greater tree mortality along the western edge of the eastern hardwoods in Texas, as modeled using current, post-drought climate conditions from 2015. This trend was confirmed by remotely sensed observations of drought-induced tree mortality, where we observed greater percent drought impacted area along the western edge of the eastern hardwoods due to the 2011 drought, (Figure 21) (Schwantes et al., 2017).

In summary, we modeled both species-specific live abundance and mortality jointly, using covariates related to mean climate, climate variability, and local-scale factors (e.g., soils, and topography). We found that by modeling both live and dead basal area simultaneously, we could predict percent basal area loss that matched spatial patterns of observed canopy lost from the recent severe 2011 drought in Texas. We also found that it was important to include covariates related to climate extremes in predicting both mortality and shifts in species abundance, as species are likely to respond to changes in both climate means and variability. Lastly, we observed that species distributions for the eastern hardwoods were projected to shift eastwards, whereas western shrubland species were projected to become increasingly dominant

throughout Texas, considering the increase in droughts and heatwaves projected under climate change through the 21<sup>st</sup> century.

## 6. Conclusion

In chapters 2 and 3 of this dissertation, I identified two new remote sensing approaches capable of quantifying canopy loss due to the 2011 drought in Texas. As droughts and heatwaves have already intensified under continuing climate change, remote sensing gives us the opportunity to monitor forest response. By using remotely sensed data, the frequency and extent of drought-induced tree mortality can be measured, across large regions in a systematic and thorough manner. Then in chapters 3, 4, and 5, I showed how these canopy loss maps can be used to validate models, to improve forecasts of tree water stress and to improve predictions of potential tree community shifts. Specifically, in chapter 3, I quantified how likely 2011 climatic anomalies are projected to be surpassed in the future. In chapter 4, I showed the importance of including local landscape factors, in addition to climate, when interpreting spatial patterns of canopy loss and when forecasting changes in future tree water stress. Lastly, in chapter 5, I presented how future droughts and heatwaves will likely change the tree composition of Texas' forests.

In 2011, the most severe single year drought on record caused significant tree mortality across Texas. Droughts like this in Texas and elsewhere are expected to become more common as temperatures increase; therefore, reliable and robust methods are needed that can systematically detect drought-induced canopy loss. In chapter 2, I present a semi-automated method to quantify the canopy loss due to the 2011 drought

using multiple scales of publically available data, from high to moderate resolution imagery. For open canopy systems, I proposed using zero-inflated beta regression models instead of linear regressions and RF models to predict percent canopy loss within a pixel, as they were more suitable for zero-inflated continuous proportion data. Knowing where canopy loss occurred will help us to quantify ecological impacts, to calibrate and/or validate mortality algorithms in regional models, and to better understand the spatiotemporal dynamics of tree mortality.

In chapter 3, I mapped drought-induced canopy loss across the state of Texas and documented impacted ecological systems and climate drivers that explained canopy loss patterns across a 5-fold precipitation gradient from humid to semiarid regions. Our approach could be used to identify relationships between climate and tree mortality in other semi-arid and/or temperate systems experiencing drought. Much of the loss was from *J. ashei*, a recently encroaching shrub/tree. Substantial levels of mortality also occurred for this species during the 1950s drought, suggesting that *J. ashei* was being restricted from further encroachment by drought. Studies have proposed that gains in woody shrub encroachment may counter balance drought-induced forest loss. However, given that woody encroachment seemed to be drought-restricted in this ecosystem, then perhaps less forest loss will be offset than originally thought (Barger et al., 2011). Additionally, we found that the 2011 climate anomalies associated with a 9.5% loss in canopy were likely to become the norm under RCP 8.5 scenario, for the 2011 VPD

anomaly and 2011 P-PET water deficit during the 2070-2099 period and for the temperature anomaly during the 2040-2099 period, which could have significant impacts for the forests of Texas. Until more mechanistic approaches can be developed, tested, and parameterized globally, defining empirical relationships between canopy loss and climate may improve our ability to forecast how forests will respond to increased drought pressure following climate change.

Other local scale factors in addition to climate, also account for spatial variation in tree mortality across a landscape. In chapter 4, we modeled dynamic water stress across a landscape at a 30-m spatial resolution by incorporating spatial heterogeneity of (1) soil conditions (e.g. texture and depth), (2) surface/subsurface lateral water flow using a topographic index, and (3) PET attributable to radiation and temperature differences. We defined dynamic water stress by incorporating the average intensity, frequency, and duration of deviations in soil moisture below a point associated with a 50% loss in hydraulic conductivity of roots for *J. ashei*. Including topographically variable input parameters improved our ability to predict spatial patterns of canopy loss observed during the 2011 drought. Furthermore, the model projected increases in mean dynamic water stress throughout the 21<sup>st</sup> century. Models with landscape heterogeneity showed some buffering capacity, but it was limited. The landscape can act as a buffer against water stress, but depending on the topography of the watershed, the buffering capacity has the potential to be overwhelmed if future droughts are too severe. By

incorporating landscape heterogeneity in models, we can test whether landscapes can act as effective buffers against future droughts and heatwaves projected under climate change.

In chapter 5, I modeled species-specific dead and live basal area using a generalized joint attribute model, by fitting the model to plot-level estimates of abundance observed in FIA plots. I observed improved spatial congruence between our canopy loss maps and model predictions of changes in abundance before and after the 2011 drought, when incorporating climate extremes and modeling live and dead basal area by species simultaneously. Species have unique responses to drought stress, and as such we expect future droughts and heat stress to change the community composition of forests. Differential tree mortality due to drought can change the structure and function of a forest and cause cascading consequences across trophic levels. We projected a reduction in species abundance for the eastern hardwoods and an expansion of western woodland and shrubland species across Texas. By simultaneously modeling species abundance as well as tree mortality, we can improve upon forecasts of shifts in species compositions over the latter half of the 21<sup>st</sup> century.

In summary, I improved upon our ability to monitor drought-induced tree mortality across large regions in systematic ways, by identifying remote sensing approaches capable of quantifying canopy loss across a diverse range of ecological systems. I also showed how these canopy loss maps could be used to better train and

validate models, to aid in future predictions of forest response to a changing climate. I identified empirical relationships between canopy loss and tree mortality; and showed how often climate anomalies associated with canopy loss would be crossed through the 21<sup>st</sup> century. I then showed the importance of including local scale factors related to soil texture/depth as well as landscape position in order to more accurately predict changes in tree water stress. Then using GJAM, I modeled dead and live basal area, using covariates related to climate variability as well as local-scale landscape factors; and found that tree community shifts will likely occur in Texas with continuing climate change, with an expansion of western shrubland species and a retraction of the eastern hardwoods.

## Appendix A

To understand the effect of aggregation on the error rate for our models, we conducted leave-one-out cross validation, where one orthophoto image was withheld as testing data and the remaining 14 images were used to train a ZOIB regression model. We did this 15 times, until each image had acted as testing data. We then repeated this analysis for each of the three aggregation datasets: 30-m, 60-m, and 90-m cells. The 60-m spatial resolution decreased the error rate significantly, while only slightly increasing the spatial resolution of Landsat (Figure 25), and thus data were aggregated to 60-m.

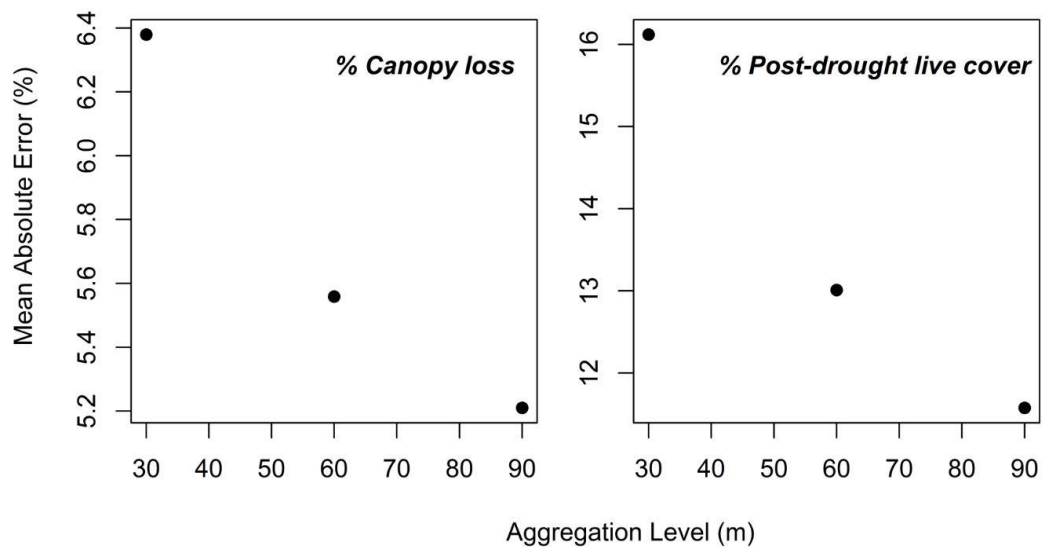


Figure 25. Comparison of the effect of increasing aggregation on model error.

## **Appendix B**

### ***B.1 Canopy loss maps: remotely sensed observations***

#### **B.1.1 Fine-scale canopy loss maps: training and testing data**

For NAIP image selection, we chose cloud-free images with >5% usable data, in other words subtracting out non-forest cover and burned area. At least one orthophoto was chosen per Landsat scene. However, Landsat scenes on the edge of the state, which represented less than 2% of the forest cover total within the state, were not assigned an orthophoto as training data (5 out of 46 images). We co-registered each pre-drought (2010) and post-drought (2012) orthophoto by manually selecting 30 tie points, using a 1st or 2nd order polynomial transformation (root mean square error, RMSE <1.0 m), and resampling with nearest neighbor. For each of the 194 selected quarter quads, we ran a supervised classification using the maximum likelihood algorithm, on a stack of pre-drought and post-drought orthophotos (10 bands: 2010 - R, G, B, NIR & NDVI (Normalized Difference Vegetation Index) and 2012 - R, G, B, NIR & NDVI). Training data were manually defined, dependent on dominant features in the scenes (e.g., live canopy, water, pasture) as well as features that changed during the study period (e.g. canopy loss: live canopy in 2010 and dead canopy in 2012). Post-classification features were grouped into three main classes: post-drought live canopy, canopy loss due to the drought, and non-tree cover. We then removed isolated single pixels using a 3 by 3-pixel majority filter. All orthophoto processing was completed in ENVI/IDL 5.0.

For field validation, we used a stratified random sample to identify plot locations by dividing the potential sampling area into three equal area strata based on high, medium, and low tree canopy cover loss derived from the orthophoto classifications. We chose an equal number of plots per strata. As such, within a site, we were able to sample the entire range of canopy loss with a relatively small number of plots. Because of time constraints, one additional plot location in Sam Houston National Forest was chosen using a simple random sample. On surveying two additional sites (Table 15), the majority of the dead trees had already fallen to the ground, which made it unfeasible to accurately map canopy cover loss; therefore, we did not include these sites in the analysis. Rules for defining dead and live crowns can be found in Table 16. For areas with slopes greater than  $5^\circ$ , we corrected transect length to account for slope. For trees  $\leq 2.5$  m in height, we used a perpendicular metal sampling rod to estimate crown cover, and for trees  $> 2.5$  m we used a GSR densitometer (sighting device). GPS points of the plot center were collected using a JUNO Trimble GPS unit and later differentially corrected using Pathfinder.

**Table 15: Field site location and number of plots collected at each site.**

<b>Modeling zone</b>	<b>Site name (# of plots)</b>
Piney woods	1. Sam Houston National Forest (7) 2. Angelina National Forest (6) 3. Sabine National Forest (3)
Oak woods & Blackland Prairie	4. Government Canyon State Natural Area (3) 5. Irving City Parks (6) **Fort Boggy State Park
Rolling Plains	6. Copper Breaks State Park (6) 7. Big Spring State Park (6)
Trans Pecos	8. Big Bend Ranch State Park (6)
Edwards Plateau	9. Mason Mountain Wildlife Management Area (6) 10. Colorado Bend State Park (6) 11. Turkey Bend Recreational Area (6)
South Texas & Gulf Coast	12. Resaca de la Palma State Park (3) 13. Texana Park & Campground (3) **Athey Nature Area

\*\*We surveyed trees at Athey Nature Area (3 plots) and Fort Boggy State Park (3 plots); however, we had little confidence in our ground estimates of dead crowns, because the majority of the trees at these sites had fallen to the ground and therefore, it was impossible to accurately determine the true size of the dead canopies, when they were standing.

**Table 16: Rules for determining the health status of a tree on the ground**

<b>Dead crowns due to 2011 drought</b>	<b>Post-drought live crowns</b>	<b>Dead crowns prior to 2011 drought</b>
<i>Rule 1</i> If dead overstory crowns were above live understory crowns.	<i>Rule 4</i> If live crowns were below dead crowns, but the tree was the same individual (e.g., dead crown, re-sprouts greater than 1-m tall)	<i>Rule 6</i> If a tree appeared to be dead for greater than 3-4 years (e.g. missing bark and medium to large branches), it was considered to have died before the drought.
<i>Rule 2</i> If a tree had re-sprouts, but these re-sprouts were not over the line transect.	<i>Rule 5</i> If live crowns were above or at relatively the same level as another dead tree. We are not estimating understory tree mortality in this study; it's difficult to say whether these understory trees died due to water stress or competition.	
<i>Rule 3</i> If a tree had resprouts from the root collar, that were less than 1-m tall, then the resprouts were considered to be unlikely to be viable or if viable then a new tree		

### **B.1.2 Regional coarse-scale 30-m binary canopy loss maps**

For masking out cleared areas we used a more conservative threshold of 0.2 in the 4 western ecological zones, because (1) there was less clearing and (2) canopy loss could look like clearing in these regions, because the understory was less dense. There were no cloud-free images for six Landsat scenes, and as such additional images with close acquisition dates were used to fill in cloudy areas of poor quality. We made the following adjustments to random forest in order to account for the excess zeros in our dataset. To select training data for each classification tree, we sampled each class equally in other words we down-sampled the inflated class (no loss pixels) to match the

frequency of the rare class (loss pixels). When using the random forest algorithm, no data are lost by down-sampling because new samples are drawn for each tree; the entire dataset can still be utilized in the ensemble modeling. Also, random forest can compute the probability of a pixel's class membership. We used receiver operating characteristic (ROC) curves (Sing *et al.*, 2005), to determine the class of each pixel (e.g., canopy loss vs. no loss). For multiple cut-off values of the probability of a loss pixel's class membership, ROC curves plotted true positive rate (TPR, accurately predicting a loss pixel when a loss pixel occurred) against true negative rate (TNR, accurately predicting a no loss pixel when no loss pixel occurred). Then, we selected the cut-off value that balanced TPR and TNR. We used 80% of the data to train the random forest models and 20% of the data in the ROC analysis to define the cutoff values. Models built using data with an excess of one class often have poor prediction of the rarer class; however, tuning with an ROC curve forces the model to balance the accuracy of both classes.

We performed leave one out cross validation to create a spatially independent testing dataset. If the modeling zone had (n) orthophoto classifications, then we trained the model with n-1 orthophoto classifications, where one orthophoto classification was withheld as testing data. For the training dataset, we withheld 20% of the data within each of the n-1 orthophotos in order to perform the ROC analysis, and used the remaining 80% to build random forest models. We then repeated this analysis for each orthophoto classification (n), until each orthophoto had acted as testing data, and then

averaged the accuracy metrics across all of the n model runs. We did this to ensure that our testing data were always spatially independent of the training data, to achieve a better understanding of how our models performed out-of-sample. However, for each modeling zone's final model we used all of the orthophoto classifications as training data, again with 80% of each orthophoto used to train the random forest model and 20% used in the ROC analysis.

**Table 17: Selected Landsat scenes. Base (B) and fill (F) scenes are both provided for scenes that required filling due to clouds and cloud shadows. Digits of each image represent sensor (1:3); path/row (4:9); acquisition year (10:13) and acquisition day of year (14:16)**

#	Path/Row	Pre-drought image	Post-drought image
1	29/35	LT50290352010233EDC00	LC80290352013177LGN01
2	29/36	LT50290362010249EDC00	LC80290362013209LGN00
3	29/37	LT50290372010249EDC00	LC80290372013241LGN00
4	29/38	LT50290382010249EDC00	LC80290382013273LGN00
5	29/39	B: LT50290392010233EDC00 F: LT50290392010217EDC00	LC80290392013273LGN00
6	29/40	LT50290402010233EDC00	LC80290402014244LGN00
7	27/36	LT50270362010219EDC00	LC80270362013243LGN00
8	27/37	LT50270372009216PAC03	LC80270372013243LGN00
9	27/38	LT50270382010235EDC00	LC80270382013243LGN00
10	27/39	LT50270392010235EDC00	LC80270392013243LGN00
11	27/40	LT50270402010235EDC00	LC80270402013243LGN00
12	27/41	LT50270412010235EDC00	LC80270412014182LGN00
13	27/42	LT50270422010235EDC00	LC80270422013211LGN01
14	25/37	LT50250372010221PAC01	B: LC80250372013133LGN01 F: LC80250372013181LGN01
15	25/38	LT50250382009138EDC00	LC80250382013133LGN01
16	25/39	LT50250392009138EDC00	B:LC80250392013133LGN01 F: LC80250392013229LGN00
17	25/40	LT50250402009138EDC00	LC80250402014136LGN00
18	32/38	LT50320382010174EDC00	LC80320382013166LGN00
19	32/39	LT50320392010222EDC00	LC80320392013214LGN00
20	30/35	LT50300352010224PAC01	LC80300352013232LGN00
21	30/36	LT50300362010224PAC01	LC80300362013248LGN00
22	30/37	LT50300372010224PAC01	LC80300372013264LGN00
23	30/38	LT50300382009221PAC01	LC80300382013216LGN00
24	30/39	LT50300392009221EDC00	LC80300392013216LGN00
25	30/40	LT50300402010272EDC00	LC80300402013216LGN00
26	28/36	LT50280362010226EDC00	LC80280362013218LGN00

#	Path/Row	Pre-drought image	Post-drought image
27	28/37	LT50280372009191PAC01	LC80280372013218LGN00
28	28/38	LT50280382009191PAC01	LC80280382013218LGN00
29	28/39	LT50280392009191EDC00	LC80280392013218LGN00
30	28/40	B: LT50280402009239CHM01 F: LT50280402009191EDC00	LC80280402013218LGN00
31	28/41	LT50280412009239CHM01	LC80280412013218LGN00
32	26/36	LT50260362010228PAC01	LC80260362013268LGN00
33	26/37	LT50260372010228PAC01	LC80260372013268LGN00
34	26/38	B: LT50260382010212EDC00 F: LT50260382010228EDC00	LC80260382013220LGN00
35	26/39	LT50260392010212EDC00	LC80260392013220LGN00
36	26/40	LT50260402010212EDC00	LC80260402013268LGN00
37	26/41	B: LT50260412010228EDC00 F: LT50260412010148EDC00	LC80260412013220LGN00
38	26/42	LT50260422009257CHM01	LC80260422013220LGN00
39	33/38	LT50330382010165EDC00	LC80330382013157LGN00
40	24/38	LT50240382010214EDC00	LC80240382014225LGN00
41	24/39	LT50240392010214EDC00	LC80240392014225LGN00
42	31/35	LT50310352010215EDC00	LC80310352013271LGN00
43	31/36	LT50310362010215EDC00	LC80310362013271LGN00
44	31/38	LT50310382010215EDC00	LC80310382013271LGN00
45	31/39	LT50310392010167EDC00	LC80310392013159LGN00
46	31/40	LT50310402010215EDC00	LC80310402013207LGN00

**Table 18: Final covariates selected for each model and variable importance measures (mean decrease in accuracy). L5 (Landsat 5) pre-drought 2009 or 2010 images and L8 (Landsat 8) post-drought 2013 or 2014 images.**

Modeling zone	Pineywoods	Oakwoods & Blackland Prairies	Rolling Plains	Trans Pecos	Edwards Plateau	South Texas & Gulf Coast
Vegetation Indices (Mean decrease in accuracy)	L8 NBR (0.053)	L5 NDVI (0.037)	L5 TCW (0.045)	L5 TCW (0.053)	L5 TCB (0.06)	L8 RGI (0.089)
	L8 TCB (0.032)	L5 TCB (0.029)	L5 (SWIR/NIR) (0.04)	L5 TCB (0.047)	L5 TCW (0.052)	L8 NBR2 (0.08)
	% tree (0.03)	% tree (0.028)	L5 TCW (0.037)	L8 DVI (0.044)	L8 DVI (0.047)	L5 GNDVI (0.072)
	L5 GNDVI (0.025)		L8 DVI (0.036)	L8 RGI (0.04)	L8 TCB (0.044)	L5 DVI (0.062)
	L5 TCB (0.022)	L5 TCG (0.028)	L5 NDVI (0.034)	L8 NBR2 (0.039)	L8 NBR2 (0.044)	L8 GNDVI (0.058)
	L5 NBR (0.021)	L5 NBR2 (0.028)	L5 DVI (0.032)	L8 SAVI (0.031)	L5 GNDVI (0.043)	L5 NBR2 (0.053)
	L8 DVI (0.018)	L8 NBR2 (0.026)	L8 (SWIR/NIR) (0.031)	L5 NBR2 (0.029)	L8 (SWIR/NIR) (0.043)	L5 TCW (0.048)
	L5 DVI (0.016)	L8 TCB (0.02)	% tree (0.029)	L8 TCB (0.023)	% tree (0.038)	L5 TCW (0.045)
	L5 RGI (0.011)	L8 RGI (0.018)	L8 RGI (0.028)	L8 NBR (0.023)	L5 DVI (0.036)	L8 DVI (0.045)
	L8 RGI (0.01)	L5 NBR (0.014)	L8 TCB (0.028)	% tree (0.022)	L8 TCW (0.034)	L5 NBR2 (0.044)
	L8 GNDVI (0.002)	L5 NBR2 (0.013)	L8 NDVI (0.026)	L8 TCW (0.022)	L8 RGI (0.031)	L5 TCW (0.045)
		L8 NDVI (0.008)	L8 NBR2 (0.022)	L8 (SWIR/NIR) (0.022)	L5 (SWIR/NIR) (0.031)	L5 TCW (0.045)
		L8 NDVI (0.008)	L8 NBR2 (0.022)	L5 (SWIR/NIR) (0.021)	L8 GNDVI (0.031)	L8 DVI (0.045)
		L8 TCG (0.004)	L8 NDVI (0.008)	L8 TCW (0.021)	L5 (SWIR/NIR) (0.021)	L8 DVI (0.045)
		L8 NBR (0.002)	L5_NBR2 (0.017)	L5_NBR2 (0.017)	L5 DVI (0.02)	L5 NDMI (0.044)
			L8 TCG (0.004)	L8 GNDVI (0.017)	L8 GNDVI (0.017)	L8 NDMI (0.044)
			L8 NBR (0.002)	L5 RGI (0.009)	L5 GNDVI (0.015)	L8 TCW (0.043)
					L5 SAVI (0.015)	% tree (0.042)
					L5 RGI (0.015)	L8 TCB (0.036)
						L5 RGI (0.035)

**Table 19: Probability thresholds (T) used to distinguish areas of canopy loss (>25%) from areas of no (0%) canopy loss. The group of Landsat scenes (Path/Row) used to select each threshold is also provided in parentheses**

<b>Modeling zones</b>	<b>Thresholds (Landsat scenes – path/row)</b>
Piney woods	T1: 0.308 (25/37,25/38,25/39,24/38,24/39,26/38) T2: 0.754 (26/39) T3: 0.430 (27/36,27/37,26/36,26/37)
Oak woods & Blackland Prairies	T1: 0.418 (26/37,26/38,26/39,26/40,27/36,27/37,27/38,27/39,27/40,28/39,28/40)
Rolling Plains	T1: 0.414 (27/36,27/37,27/38,27/39) T2: 0.416 (29/35,29/36,29/37,29/38) T3: 0.471 (31/35,31/36,30/35,30/36,30/37,30/38) T4: 0.365 (28/36,28/37,28/38)
Trans Pecos	T1: 0.397 (30/38,30/39,30/40,29/39,29/40,31/39,31/40,32/38,32/39,33/38) T2: 0.681 (31/38)
Edwards Plateau	T1: 0.397 (29/37,29/38,29/39,30/38,30/39,28/38,28/40) T2: 0.324 (28/39) T3: 0.318 (27/39,27/40)
South Texas & Gulf Coast	T1: 0.362 (25/39,25/40,26/39,26/40,26/42,28/39,28/40,28/41,27/41,27/42,27/40,24/39) T2: 0.674 (26/41) T3: 0.374 (29/39,29/40)

***B.2. Identifying climatic thresholds that control spatial patterns of canopy loss and determining whether these thresholds are likely to be surpassed in the future and identifying impacted ecological systems***

For precipitation, we computed percent deviation from normal (EQ1), as we were examining patterns across a 5-fold precipitation gradient. For temperature and

VPD we calculated anomalies from historical climate (EQ2). For precipitation minus potential evapotranspiration (P-PET) we used 2011 values.

$$\frac{2011 \text{ value} - \text{historical value}}{\text{historical value}} * 100 = \% \text{ deviation from normal} \quad \text{Equation B1}$$

$$2011 \text{ value} - \text{historical value} = \text{anomaly} \quad \text{Equation B2}$$

**Table 20: Drought impact on all tree-dominated ecological systems in Texas**

<b>Common name</b>	<b>Area (km<sup>2</sup>)</b>	<b>Percent of community impacted</b>
Chenier Plain: Salt and Brackish Low Tidal Shrub Wetland	0	0.0%
Coastal: Mangrove Shrubland	15.5	0.7%
Columbia Bottomlands: Mixed Evergreen - Hardwood Forest and Woodland	135	4.1%
Columbia Bottomlands: Baldcypress Swamp	0.9	4.2%
Chenier Plain: Mixed Live Oak - Deciduous Hardwood Fringe Forest	131.4	4.3%
Edwards Plateau: Deciduous Semi-arid Slope Shrubland	813	4.6%
Chenier Plain: Hardwood Fringe Forest	2.2	5.0%
Columbia Bottomlands: Live Oak Forest and Woodland	183.9	5.1%
Non-Native Invasive: Chinese Tallow Forest, Woodland, or Shrubland	999.7	5.2%
Crosstimbers: Live Oak Forest and Woodland	26.7	5.4%
Pineywoods: Bottomland Temporarily Flooded Live Oak Forest	0.3	5.4%
Pineywoods: Southern Mesic Pine - Hardwood Forest	112.7	5.9%
Columbia Bottomlands: Hardwood Forest and Woodland	1703.8	6.0%
Pineywoods: Bottomland Evergreen Successional Shrubland	1.8	6.4%
Pineywoods: Bottomland Temporarily Flooded Mixed Pine - Hardwood Forest	68.2	6.7%
Pineywoods: Small Stream and Riparian Live Oak Temporarily Flooded Forest	0.1	7.1%
Pineywoods: Small Stream and Riparian Temporarily Flooded Mixed Forest	364.2	7.5%
Columbia Bottomlands: Evergreen Shrubland	123.2	7.6%
Edwards Plateau: Deciduous Semi-arid Shrubland	4339.7	7.8%
Pineywoods: Seepage Swamp and Baygall	7.9	7.8%
Coastal Bend: Floodplain Hardwood Forest	372.1	7.9%
Pineywoods: Southern Mesic Hardwood Forest	269.8	8.0%
Central Texas: Floodplain Baldcypress Swamp	2.8	8.0%
Pineywoods: Weches Shrub Glade	0.4	8.4%

Pineywoods: Small Stream and Riparian Seasonally Flooded Hardwood Forest	894.2	8.4%
Pineywoods: Longleaf or Loblolly Pine - Hardwood Flatwoods or Plantation	310.5	8.5%
Columbia Bottomlands: Riparian Mixed Evergreen - Hardwood Forest and Woodland	2	9.2%
Pineywoods: Wet Hardwood Flatwoods	149.2	9.3%
Gulf Coast: Near-Coast Baldcypress Swamp	36	9.4%
High Plains: Depressional Wet Shrubland	28.9	9.8%
Edwards Plateau: Shin Oak Shrubland	2465.3	10.2%
South Texas: Shallow Live Oak Motte and Woodland	0.3	10.9%
Edwards Plateau: Riparian Deciduous Shrubland	1094.6	11.4%
Coastal Bend: Riparian Live Oak Forest	24	11.4%
Native Invasive: Mesquite - Creosotebush Shrubland	6365.6	11.5%
Pineywoods: Hardwood Flatwoods	1484	11.5%
Pine Plantation > 3 meters tall	2536.3	11.7%
Coastal Bend: Riparian Hardwood Forest	44.9	11.9%
Pineywoods: Bottomland Seasonally Flooded Hardwood Forest	1604	12.0%
South Texas: Clayey Mesquite Mixed Shrubland	16165.1	12.2%
Crosstimbers: Sandyland Oak Woodland	271.9	12.3%
Columbia Bottomlands: Riparian Hardwood Forest and Woodland	38.8	12.6%
Pineywoods: Northern Mesic Pine - Hardwood Forest	157.6	12.7%
Edwards Plateau: Floodplain Deciduous Shrubland	1491.7	12.7%
South Texas: Clayey Live Oak Motte and Woodland	81.3	13.0%
Non-native Invasive: Elm - Olive Woodland	31.1	13.0%
Inland: Salty Prairie Shrubland	8.6	13.1%
Pineywoods: Bottomland Temporarily Flooded Hardwood Forest	950.8	13.2%
Central Texas: Floodplain Live Oak Forest	75.9	13.3%
Coastal Bend: Riparian Live Oak - Hardwood Forest	6.4	13.5%
Pineywoods: Small Stream and Riparian Baldcypress Swamp	86.3	14.0%
Post Oak Savanna: Live Oak Shrubland	95.8	14.1%
Pineywoods: Longleaf or Loblolly Pine Flatwoods or Plantation	1821.7	14.2%

Columbia Bottomlands: Riparian Live Oak Forest and Woodland	2.9	14.4%
Central Texas: Floodplain Seasonally Flooded Hardwood Forest	87	14.5%
Edwards Plateau: Floodplain Live Oak Forest	516.1	14.8%
Pine Plantation 1 to 3 meters tall	1574.4	14.8%
Pineywoods: Small Stream and Riparian Evergreen Successional Shrubland	2.2	15.0%
South Texas: Ramadero Shrubland	1514.5	15.0%
South Texas: Salty Thornscrub	1128.7	15.1%
Coastal Bend: Floodplain Live Oak Forest	76.2	15.2%
Edwards Plateau: Riparian Hardwood - Ashe Juniper Forest	164.9	15.2%
Columbia Bottomlands: Deciduous Shrubland	124.9	15.5%
Edwards Plateau: Riparian Hardwood Forest	320.6	15.6%
Pineywoods: Bottomland Baldcypress Swamp	373.8	15.9%
Coastal Bend: Riparian Evergreen Shrubland	5.5	16.0%
Post Oak Savanna: Live Oak Slope Forest	1.2	16.0%
Red River: Floodplain Seasonally Flooded Hardwood Forest	14.1	16.1%
Pineywoods: Small Stream and Riparian Temporarily Flooded Hardwood Forest	3767.2	16.1%
Native Invasive: Mesquite Shrubland	33748.7	16.4%
South Texas: Sandy Live Oak Motte and Woodland	160.3	16.4%
Pineywoods: Dry Pine - Hardwood Forest or Plantation	64.3	16.4%
Red River: Floodplain Hardwood Forest	503.7	16.5%
Coastal Bend: Floodplain Live Oak - Hardwood Forest	51	16.5%
Red River: Floodplain Evergreen Shrubland	0.4	16.7%
Pineywoods: Small Stream and Riparian Deciduous Successional Shrubland	51.6	17.0%
Pineywoods: Pine - Hardwood Forest or Plantation	2477.4	17.1%
Edwards Plateau: Shin Oak Slope Shrubland	163.2	17.1%
Edwards Plateau: Post Oak Motte and Woodland	354.2	17.1%
Edwards Plateau: Floodplain Ashe Juniper Shrubland	533.4	17.2%
Central Texas: Riparian Deciduous Shrubland	278.4	17.6%
Edwards Plateau: Live Oak Motte and Woodland	7554	18.0%
Central Texas: Riparian Live Oak Forest	50	18.2%

Edwards Plateau: Riparian Live Oak Forest	524.3	18.4%
Columbia Bottomlands: Riparian Evergreen Shrubland	1.9	18.9%
Edwards Plateau: Oak - Hardwood Slope Forest	669.9	19.2%
Pineywoods: Sandhill Oak - Pine Woodland	17.1	19.2%
Coastal Bend: Riparian Deciduous Shrubland	16.7	19.5%
Post Oak Savanna: Live Oak Motte and Woodland	1464.1	19.5%
South Texas: Floodplain Deciduous Shrubland	1080.4	19.6%
Edwards Plateau: Floodplain Hardwood - Ashe Juniper Forest	111.9	19.7%
Red River: Floodplain Hardwood - Evergreen Forest	5.2	19.7%
South Texas: Floodplain Live Oak Forest and Woodland	58.9	19.9%
Pineywoods: Northern Mesic Hardwood Forest	868.8	20.3%
Columbia Bottomlands: Riparian Deciduous Shrubland	4.9	20.9%
Post Oak Savanna: Post Oak - Redcedar Motte and Woodland	164.8	21.0%
Rolling Plains: Breaks Deciduous Shrubland	4237.9	21.0%
Central Texas: Floodplain Deciduous Shrubland	829.4	21.1%
Pineywoods: Pine Forest or Plantation	16067.5	21.2%
High Plains: Mixed Hardwood - Juniper Wooded Ravine	31.9	21.3%
South Texas: Floodplain Evergreen Shrubland	192.8	21.4%
Coastal and Sandsheet: Deep Sand Shrubland	24.5	21.4%
Edwards Plateau: Oak - Hardwood Motte and Woodland	4146.4	21.6%
Invasive: Evergreen Shrubland	295.9	21.7%
Pineywoods: Longleaf Pine Woodland	16.4	21.7%
Pineywoods: Dry Pine Forest or Plantation	222.6	22.2%
Edwards Plateau: Floodplain Hardwood Forest	1238.7	22.4%
South Texas: Shallow Shrubland	6438	22.8%
Edwards Plateau: Riparian Ashe Juniper Shrubland	1357.3	23.3%
Post Oak Savanna: Post Oak - Live Oak Motte and Woodland	333	23.5%
Trans-Pecos: Desert Wash Shrubland	3482	23.7%
Central Texas: Floodplain Hardwood Forest	6000.5	23.9%
Pineywoods: Upland Hardwood Forest	11133.3	24.1%
South Texas: Ramadero Dense Shrubland	296.4	24.2%

South Texas: Clayey Blackbrush Mixed Shrubland	3051.6	24.5%
Edwards Plateau: Wooded Cliff/Bluff	3.8	24.5%
High Plains: Sandhill Shinnery Duneland	418.3	24.5%
Edwards Plateau: Juniper Semi-arid Shrubland	6289.8	24.7%
South Texas: Palm Grove	0.7	24.8%
Pineywoods: Sandhill Pine Woodland	101.9	24.9%
Pineywoods: Dry Upland Hardwood Forest	199.9	25.3%
Pineywoods: Bottomland Deciduous Successional Shrubland	32.8	25.4%
Orchard	81.1	25.5%
Native Invasive: Deciduous Woodland	5762.7	25.7%
Non-native Invasive: Saltcedar Shrubland	30	25.8%
Edwards Plateau: Floodplain Ashe Juniper Forest	51.7	25.9%
Edwards Plateau: Live Oak Slope Forest	353.9	26.6%
High Plains: Riparian Hardwood - Juniper Forest	5.4	26.6%
Post Oak Savanna: Sandyland Woodland and Shrubland	56.2	26.6%
Coastal Bend: Floodplain Deciduous Shrubland	48	26.6%
Bastrop Lost Pines: Loblolly Pine Slope Forest	0.5	26.7%
Edwards Plateau: Juniper Semi-arid Slope Shrubland	1463.4	27.1%
Post Oak Savanna: Oak - Hardwood Slope Forest	21.7	27.1%
Native Invasive: Huisache Woodland or Shrubland	638.4	27.4%
Edwards Plateau: Riparian Ashe Juniper Forest	228.6	27.4%
Central Texas: Riparian Hardwood Forest	1028	27.6%
Edwards Plateau: Oak - Ashe Juniper Slope Forest	1047.7	27.7%
Central Texas: Wooded Cliff/Bluff	0.1	27.7%
Red River: Floodplain Deciduous Shrubland	14.3	28.1%
South Texas: Shallow Dense Shrubland	1756.8	28.1%
Edwards Plateau: Ashe Juniper-Live Oak Shrubland	12331.2	28.4%
Edwards Plateau: Ashe Juniper-Live Oak Slope Shrubland	1403.1	29.0%
Post Oak Savanna: Post Oak - Live Oak Slope Forest	0.2	29.5%
Central Texas: Floodplain Evergreen Shrubland	44.5	29.6%
Coastal Bend: Floodplain Evergreen Shrubland	39.9	29.8%
Gulf Coast: Salty Prairie Shrubland	138.7	29.8%
Crosstimbers: Post Oak Woodland	6106.1	29.9%
High Plains: Floodplain Hardwood - Juniper Forest	13.9	29.9%
High Plains: Mesquite Shrubland	4478.4	30.1%

South Texas: Floodplain Evergreen Forest and Woodland	148.6	30.7%
South Texas: Loma Evergreen Shrubland	70.2	30.8%
Coastal and Sandsheet: Deep Sand Live Oak Shrubland	333.1	32.1%
South Texas: Pond and Laguna Shrubland	21.1	32.4%
Central Texas: Floodplain Hardwood - Evergreen Forest	177.9	32.4%
Edwards Plateau: Deciduous Oak - Evergreen Motte and Woodland	2883.7	32.5%
Crosstimbers: Hardwood - Juniper Slope Forest	22.9	32.7%
Pineywoods: Sandhill Oak Woodland	63.9	33.3%
Post Oak Savanna: Post Oak Motte and Woodland	12300.9	34.2%
South Texas: Floodplain Hardwood Forest and Woodland	718.2	34.2%
South Texas: Ramadero Woodland	529.8	34.3%
South Texas: Floodplain Mixed Deciduous - Evergreen Forest and Woodland	58.2	34.6%
Central Texas: Floodplain Evergreen Forest	19.1	35.4%
South Texas: Sandy Mesquite Dense Shrubland	1113	35.7%
Trans-Pecos: Juniper Savanna and Woodland	137.7	36.0%
Coastal and Sandsheet: Deep Sand Live Oak - Mesquite Woodland	10.8	36.3%
Bastrop Lost Pines: Hardwood Slope Forest	0.1	36.7%
Native Invasive: Deciduous - Juniper Woodland	33.2	36.8%
Central Texas: Riparian Hardwood - Evergreen Forest	151.7	37.8%
High Plains: Riparian Hardwood Forest	141.7	38.1%
Crosstimbers: Post Oak - Juniper Woodland	363.9	38.2%
South Texas: Ramadero Evergreen Woodland	109.1	39.1%
Bastrop Lost Pines: Loblolly Pine Forest	27	39.3%
High Plains: Floodplain Live Oak Forest	2.4	39.4%
Crosstimbers: Oak - Hardwood Slope Forest	365.2	39.5%
Pineywoods: Catahoula Woodland or Shrubland Barrens	0.2	39.6%
High Plains: Mesquite Woodland	9.6	40.1%
Native Invasive: Juniper Shrubland	2727.6	40.1%
Rio Grande Delta: Deciduous Thorn Woodland and Shrubland	1.2	40.3%
High Plains: Hardwood Wooded Ravine	5.8	40.4%

Llano Uplift: Mesquite - Whitebrush Shrubland	552.7	41.4%
Native Invasive: Catclaw Shrubland	473.8	41.7%
South Texas: Sandy Mesquite Woodland and Shrubland	8668	42.1%
Rio Grande Delta: Evergreen Thorn Woodland and Shrubland	22.3	42.1%
Edwards Plateau: Ashe Juniper Slope Forest	1498	42.3%
Trans-Pecos: Lower Montane Riparian Woodland	16.8	42.4%
High Plains: Floodplain Hardwood Forest	775.7	42.7%
Llano Uplift: Live Oak Woodland	161.6	42.9%
Central Texas: Riparian Evergreen Forest	31.8	43.3%
Rolling Plains: Breaks Evergreen Shrubland	2532.5	43.5%
High Plains: Floodplain Juniper Shrubland	33.3	44.1%
Coastal and Sandsheet: Deep Sand Live Oak Forest and Woodland	1152.6	44.5%
High Plains: Riparian Live Oak Forest	1	44.6%
Native Invasive: Juniper Woodland	549.7	44.7%
Post Oak Savanna: Oak - Redcedar Slope Forest	4.5	44.8%
High Plains: Floodplain Juniper Forest	1.1	44.9%
Bastrop Lost Pines: Loblolly Pine - Oak Slope Forest	0.4	45.6%
Edwards Plateau: Ashe Juniper Motte and Woodland	4552.3	45.7%
Trans-Pecos: Pinyon - Juniper Woodland	160.1	45.9%
Trans-Pecos: Montane Mesic and Canyon Pine - Juniper Forest	12.2	46.0%
Trans-Pecos: High Mountain Conifer Forest and Woodland	28.9	46.1%
High Plains: Riparian Juniper Forest	1.9	46.7%
Trans-Pecos: Deciduous Chaparral	252.7	47.3%
Trans-Pecos: Pinyon - Juniper Shrubland	545.2	47.5%
Trans-Pecos: Evergreen Chaparral	16.3	47.6%
Central Texas: Riparian Evergreen Shrubland	62.9	47.9%
Trans-Pecos: Gray Oak Savanna and Woodland	248.9	48.2%
Trans-Pecos: High Mountain Evergreen Shrubland	2.6	49.5%
High Plains: Riparian Juniper Shrubland	44.9	50.4%
High Plains: Sandy Shinnery Shrubland	1055.1	51.1%
Llano Uplift: Post Oak Woodland	798.6	52.8%
Post Oak Savanna: Redcedar Slope Forest	0.8	52.8%
Trans-Pecos: Riparian Woodland	32.4	53.5%

Post Oak Savanna: Post Oak - Yaupon Motte and Woodland	1348	54.9%
Trans-Pecos: Montane Mesic and Canyon Hardwood Forest	12.5	55.9%
Trans-Pecos: High Mountain Mixed Conifer - Oak Forest and Woodland	1.5	56.8%
Trans-Pecos: Montane Mesic and Canyon Shrubland	76.1	56.8%
Trans-Pecos: Rocky Mountain Gambel Oak - Mixed Shrubland	6.2	57.3%
Trans-Pecos: Ponderosa/Arizona Pine Woodland	34.2	57.7%
South Texas: Sandy Mesquite - Evergreen Woodland	203.9	58.0%
Trans-Pecos: Montane Mesic and Canyon Evergreen Shrubland	13.5	58.4%
Trans-Pecos: Montane Mesic and Canyon Hardwood - Pine - Juniper Forest	26.6	59.4%
Trans-Pecos: Mountain Evergreen Oak - Pine Shrubland	15.2	60.8%
Bastrop Lost Pines: Loblolly Pine - Oak Forest	40.2	61.4%
Crosstimbers: Juniper Slope Forest	15.4	61.9%
Trans-Pecos: Desert Wash Evergreen Shrubland	4.7	62.7%
Trans-Pecos: Mixed Oak Savanna and Woodland	312.9	62.8%
Trans-Pecos: Ponderosa/Arizona Pine - Oak Woodland	0.4	63.3%
Rio Grande Delta: Dense Shrubland	0.1	64.2%
Trans-Pecos: Pinyon - Juniper - Oak Woodland	112.9	66.0%
South Texas: Pond and Laguna Woodland	36.3	66.7%

---

## Appendix C

**Table 21: Comparison of general circulation models in predicting annual rainfall (mm) from 1980 to 2005, ranked from lowest to highest mean absolute error (MAE). Root mean square error (RMSE) and the ratio of standard deviation of the model to the observed value (NSD), are also presented**

Ranking	GCM	MAE	RMSE	NSD
1	MIROC5	150	188	0.996
2	NorESM1-M	156	189	0.990
3	IPSL-CM5B-LR	176	213	1.21
4	GFDL-ESM2G	180	225	1.25
5	BNU-ESM	182	237	1.00
6	bcc-csm1-1-m	194	233	0.943
7	CNRM-CM5	195	230	1.21
8	bcc-csm1-1	195	254	1.25
9	CSIRO-Mk3-6-0	198	247	1.18
10	MIROC-ESM-CHEM	200	226	1.17
11	CCSM4	217	275	1.53
12	CanESM2	229	285	1.43
13	MRI-CGCM3	229	281	1.33
14	MIROC-ESM	233	277	1.21
15	HadGEM2-CC365	240	303	1.61
16	inmcm4	242	284	1.54
17	GFDL-ESM2M	245	295	1.43
18	HadGEM2-ES365	274	329	1.40
19	IPSL-CM5A-MR	287	358	2.15
20	IPSL-CM5A-LR	308	363	1.71

## C.1 Analytical solutions for static water stress and crossing properties

### C.1.1 Soil moisture probability distribution under steady state conditions

We can derive the probability density function of soil moisture,  $p(s)$ , from the steady-state solution of the corresponding Chapman-Kolmogorov forward equation. We provide the solution, Eq. C1; however, the full derivation can be found in Laio *et al.* (2001) and Rodriguez-Iturbe *et al.* (1999). The constant of integration,  $C$ , can be computed by the normalization condition, Eq. C2.

$$\eta_w = \frac{E_w}{nZ_r} \quad \eta = \frac{E_{max}}{nZ_r} \quad m = \frac{K_s}{nZ_r(e^{\beta(1-s_{fc})} - 1)} \quad \lambda' = \lambda e^{-\Delta/\alpha} \quad \gamma = \frac{nZ_r}{\alpha'}$$

$$p(s) = \begin{cases} \frac{C}{\eta_w} \left( \frac{s-s_h}{s_w-s_h} \right)^{\frac{\lambda'(s_w-s_h)}{\eta_w}-1} e^{-\gamma s}, & s_h < s \leq s_w, \\ \frac{C}{\eta_w} \left[ 1 + \left( \frac{\eta}{\eta_w} - 1 \right) \left( \frac{s-s_w}{s^*-s_w} \right) \right]^{\frac{\lambda'(s^*-s_w)}{\eta-\eta_w}-1} e^{-\gamma s}, & s_w < s \leq s^*, \\ \frac{C}{\eta} e^{-\gamma s + \frac{\lambda'}{\eta}(s-s^*)} \left( \frac{\eta}{\eta_w} \right)^{\frac{\lambda'(s^*-s_w)}{\eta-n_w}}, & s^* < s \leq s_{fc}, \\ \frac{C}{\eta} e^{-(\beta+\gamma)s + \beta s_{fc}} \left( \frac{\eta e^{\beta s}}{(\eta-m)e^{\beta s_{fc}} + m e^{\beta s}} \right)^{\frac{\lambda'}{\beta(\eta-m)}+1} \left( \frac{\eta}{\eta_w} \right)^{\frac{\lambda'(s^*-s_w)}{\eta-n_w}} e^{\frac{\lambda'}{\eta}(s_{fc}-s^*)}, & s_{fc} < s \leq 1, \end{cases} \quad Eq. C1$$

$$\int_{s_h}^1 p(s) ds = 1 \quad Equation C2$$

### C.1.2 Analytical solution for static water stress

Following Porporato *et al.* (2001), we can compute the probability distribution for the static water stress,  $\zeta$ , Eq. C3, as a derived distribution of the soil moisture distribution function,  $p(s)$ , over the range,  $s_h < s \leq s_m$ , and where  $q = 1$ ,

$$p_z(\zeta) = \frac{C_\zeta}{\eta_w} \left( \frac{s_m - s_h}{s_w - s_h} - \frac{\zeta(t)(s_m - s_h)}{s_w - s_h} \right)^{\frac{\lambda'(s_w - s_h) - 1}{n_w}} e^{-\gamma s_m + \zeta(t)\gamma(s_m - s_h)} \quad \text{Equation C3}$$

There is an atom of probability only at  $\zeta = 0$ , because as  $\zeta$  approaches 1, the soil moisture approaches the hygroscopic point, Eq C4.

$$P_z(0) = 1 - P(s_m) \quad \text{Equation C4}$$

The integration constant can thus be determined by imposing the following normalization condition,

$$\int_0^1 p_z(\zeta) d\zeta = P(s_m) \quad \text{Equation C5}$$

The mean water stress,  $\bar{\zeta}$ , Eq. C6, and the mean water stress if a stress occurs,  $\bar{\zeta}'$ , Eq. C7, can be derived as follows,

$$\bar{\zeta} = \int_0^1 \zeta p_z(\zeta) d\zeta \quad \text{Equation C6}$$

$$\bar{\zeta}' = \frac{\bar{\zeta}}{P(s_m)} \quad \text{Equation C7}$$

### C.1.3 Analytical solution for $\bar{T}_{sm}$ and $\bar{n}_{sm}$

The mean and probability distribution functions of the static water stress,  $\zeta$ , do not incorporate any information on the timing or duration of the soil moisture crossings below  $s_m$ . The average duration of time spent,  $\bar{T}_{sm}$ , below  $s_m$ , Eq. C8, as well as the average number of times  $s_m$  was crossed,  $\bar{n}_{sm}$ , Eq. C9 are also considered in developing an index of tree water stress, relevant to tree mortality, following the framework proposed by Porporato *et al.* (2001).

$$\bar{T}_{sm} = \left( \frac{1}{\eta_w \left( \frac{s_m - s_h}{s_w - s_h} \right)^{\frac{\lambda'(s_w - s_h)}{\eta_w}}} \right) \times \left\{ e^{\gamma(s_m - s_h)} (s_w - s_h) [\gamma(s_w - s_h)]^{\frac{\lambda'(s_w - s_h)}{\eta_w}} \right\} \times \left\{ \Gamma \left[ \frac{\lambda'(s_w - s_h)}{\eta_w} \right] - \Gamma \left[ \frac{\lambda'(s_w - s_h)}{\eta_w}, \gamma(s_m - s_h) \right] \right\} \quad \text{Equation C8}$$

$$\bar{n}_{sm} = C e^{-\gamma s_m T_{seas}} \left( \frac{s_m - s_h}{s_w - s_h} \right)^{\frac{\lambda'(s_w - s_h)}{\eta_w}} \quad \text{Equation C9}$$

Where  $\Gamma[.]$ , and  $\Gamma[.,.]$  are respectively the complete and incomplete Gamma functions, as defined in 6.1.1 and 6.5.3 in Abramowitz & Stegun (1964).

## Appendix D

Species-specific beta coefficients for the following covariates: percent clay, percent sand, elevation, heat load, topographic compound index, and historical climatic water deficit, for Model C, fitting the model to both live and dead basal area.

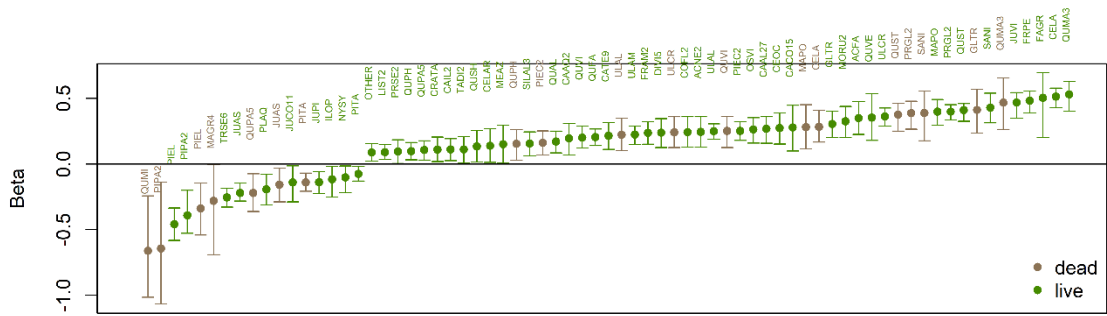


Figure 26: Species-specific beta coefficients for the covariate percent clay

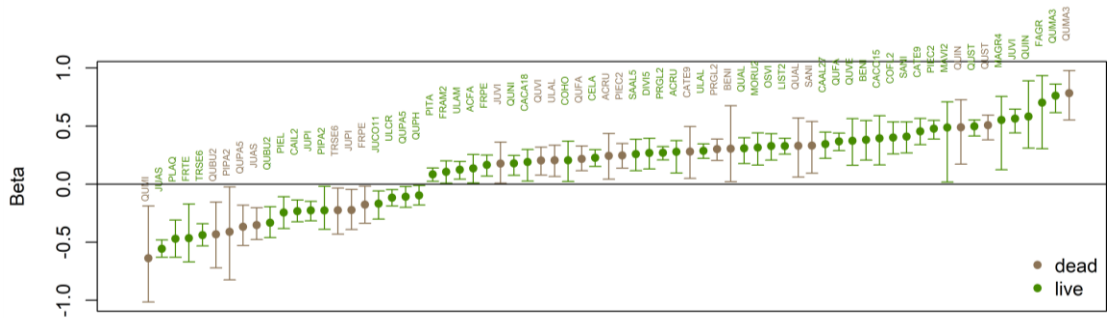


Figure 27: Species-specific beta coefficients for the covariate percent sand



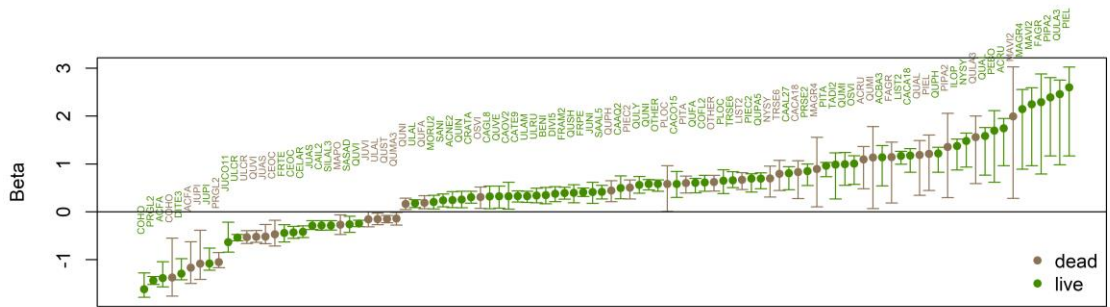


Figure 31: Species-specific beta coefficients for the covariate historical climatic water deficit

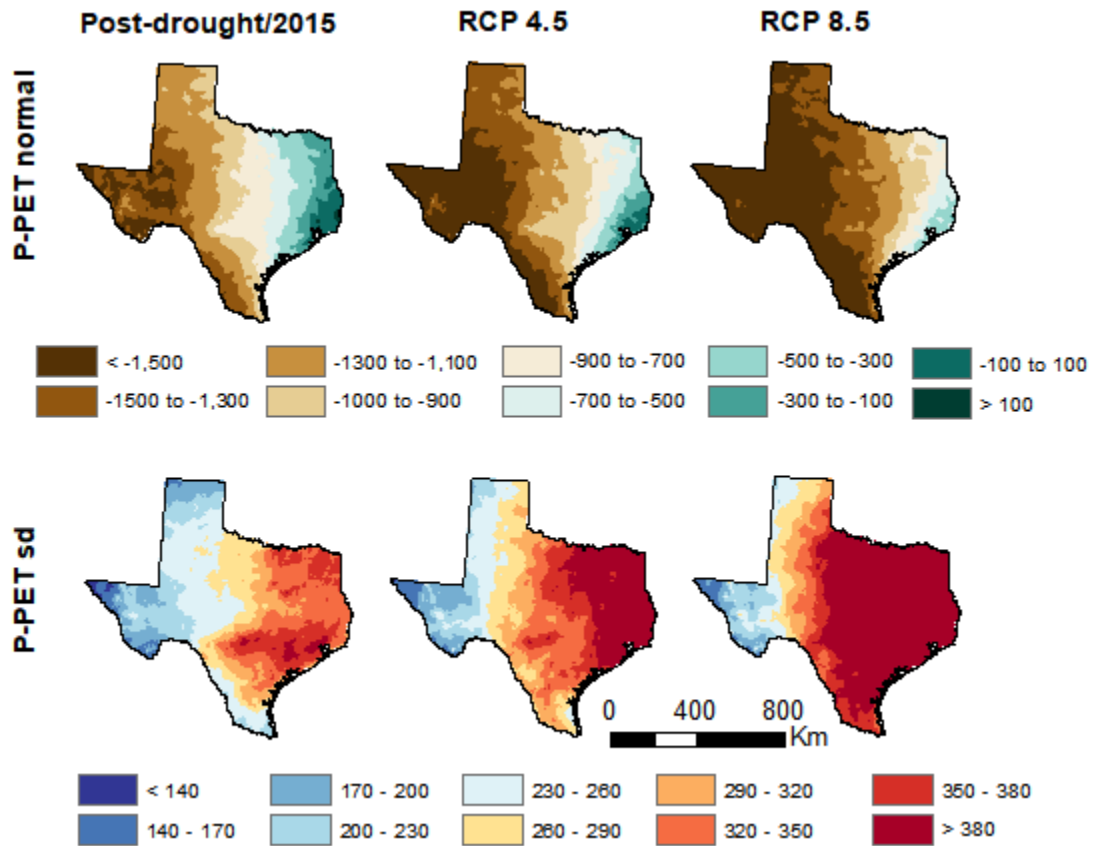


Figure 32: Climatic water deficit (Precipitation minus potential evapotranspiration (P-PET)) normal and standard deviation (sd), projected by general circulation model: MIROC5, under representative concentration pathway (RCP) 4.5 and 8.5 scenarios.

**Table 22: Common name, genus, species, symbol, and predominate location where the species can be found, East (E) of West(W) or both for the 76 species considered in the model.**

Common name	Genus	Species	symbol	East	West
bluejack oak	<i>Quercus</i>	<i>incana</i>	QUIN	E	
Bluewood	<i>Condalia</i>	<i>hookeri</i>	COHO	E	
western soapberry	<i>Sapindus</i>	<i>saponaria</i>	SASAD	E	W
black willow	<i>Salix</i>	<i>nigra</i>	SANI	E	W
sassafras	<i>Sassafras</i>	<i>albidum</i>	SAAL5	E	
winged elm	<i>Ulmus</i>	<i>alata</i>	ULAL	E	
American elm	<i>Ulmus</i>	<i>americana</i>	ULAM	E	
cedar elm	<i>Ulmus</i>	<i>crassifolia</i>	ULCR	E	
slippery elm	<i>Ulmus</i>	<i>rubra</i>	ULRU	E	
chinaberry	<i>Melia</i>	<i>azedarach</i>	MEAZ	E	
Chinese tallowtree	<i>Triadica</i>	<i>sebifera</i>	TRSE6	E	
Buckley oak	<i>Quercus</i>	<i>buckleyi</i>	QUBU2	E	
Pinchot juniper	<i>Juniperus</i>	<i>pinchotii</i>	JUPI		W
redberry juniper	<i>Juniperus</i>	<i>coahuilensis</i>	JUCO11		W
Ashe juniper	<i>Juniperus</i>	<i>ashei</i>	JUAS	E	
eastern redcedar	<i>Juniperus</i>	<i>virginiana</i>	JUVI	E	
shortleaf pine	<i>Pinus</i>	<i>echinata</i>	PIEC2	E	
slash pine	<i>Pinus</i>	<i>elliottii</i>	PIEL	E	
longleaf pine	<i>Pinus</i>	<i>palustris</i>	PIPA2	E	
loblolly pine	<i>Pinus</i>	<i>taeda</i>	PITA	E	
baldcypress	<i>Taxodium</i>	<i>distichum</i>	TADI2	E	
sweet acacia	<i>Acacia</i>	<i>farnesiana</i>	ACFA	E	W
Florida maple	<i>Acer</i>	<i>barbatum</i>	ACBA3	E	
boxelder	<i>Acer</i>	<i>negundo</i>	ACNE2	E	W
red maple	<i>Acer</i>	<i>rubrum</i>	ACRU	E	
river birch	<i>Betula</i>	<i>nigra</i>	BENI	E	
chittamwood, gum bumelia	<i>Sideroxylon</i>	<i>lanuginosum</i>	SILAL3	E	
American hornbeam, musclewood	<i>Carpinus</i>	<i>caroliniana</i>	CACA18	E	
water hickory	<i>Carya</i>	<i>aquatica</i>	CAAQ2	E	
bitternut hickory	<i>Carya</i>	<i>cordiformis</i>	CACO15	E	
pignut hickory	<i>Carya</i>	<i>glabra</i>	CAGL8	E	
pecan	<i>Carya</i>	<i>illinoensis</i>	CAIL2	E	
shagbark hickory	<i>Carya</i>	<i>ovata</i>	CAOV2	E	

black hickory	<i>Carya</i>	<i>texana</i>	CATE9	E	
mockernut hickory	<i>Carya</i>	<i>alba</i>	CAAL27	E	
sugarberry	<i>Celtis</i>	<i>laevigata</i>	CELA	E	W
hackberry	<i>Celtis</i>	<i>occidentalis</i>	CEOC	E	W
netleaf hackberry	<i>Celtis</i>	<i>laevigata</i>	CELAR	E	W
eastern redbud	<i>Cercis</i>	<i>canadensis</i>	CECA4	E	
flowering dogwood	<i>Cornus</i>	<i>florida</i>	COFL2	E	
hawthorn spp.	<i>Crataegus</i>	<i>spp.</i>	CRATA	E	
common persimmon	<i>Diospyros</i>	<i>virginiana</i>	DIVI5	E	
Texas persimmon	<i>Diospyros</i>	<i>texana</i>	DITE3	E	
American beech	<i>Fagus</i>	<i>grandifolia</i>	FAGR	E	
white ash	<i>Fraxinus</i>	<i>americana</i>	FRAM2	E	
green ash	<i>Fraxinus</i>	<i>pennsylvanica</i>	FRPE	E	
Texas ash	<i>Fraxinus</i>	<i>texensis</i>	FRTE	E	
honeylocust	<i>Gleditsia</i>	<i>triacanthos</i>	GLTR	E	
American holly	<i>Ilex</i>	<i>opaca</i>	ILOP	E	
black walnut	<i>Juglans</i>	<i>nigra</i>	JUNI	E	W
sweetgum	<i>Liquidambar</i>	<i>styraciflua</i>	LIST2	E	W
Osage-orange	<i>Maclura</i>	<i>pomifera</i>	MAPO	E	
southern magnolia	<i>Magnolia</i>	<i>grandiflora</i>	MAGR4	E	
sweetbay	<i>Magnolia</i>	<i>virginiana</i>	MAVI2	E	
red mulberry	<i>Morus</i>	<i>rubra</i>	MORU2	E	
laurel oak	<i>Quercus</i>	<i>laurifolia</i>	QULA3	E	
overcup oak	<i>Quercus</i>	<i>lyrata</i>	QULY	E	
blackjack oak	<i>Quercus</i>	<i>marilandica</i>	QUMA3	E	
swamp chestnut oak	<i>Quercus</i>	<i>michauxii</i>	QUMI	E	
water oak	<i>Quercus</i>	<i>nigra</i>	QUNI	E	
willow oak	<i>Quercus</i>	<i>phellos</i>	QUPH	E	
Shumard oak	<i>Quercus</i>	<i>shumardii</i>	QUSH	E	
post oak	<i>Quercus</i>	<i>stellata</i>	QUST	E	
black oak	<i>Quercus</i>	<i>velutina</i>	QUVE	E	
live oak	<i>Quercus</i>	<i>virginiana</i>	QUVI	E	
blackgum	<i>Nyssa</i>	<i>sylvatica</i>	NYSY	E	
eastern hophornbeam	<i>Ostrya</i>	<i>virginiana</i>	OSVI	E	
redbay	<i>Persea</i>	<i>borbonia</i>	PEBO	E	
water-elm, planertree	<i>Planera</i>	<i>aquatica</i>	PLAQ	E	
American sycamore	<i>Platanus</i>	<i>occidentalis</i>	PLOC	E	
honey mesquite	<i>Prosopis</i>	<i>glandulosa</i>	PRGL2	E	W
black cherry	<i>Prunus</i>	<i>serotina</i>	PRSE2	E	
white oak	<i>Quercus</i>	<i>alba</i>	QUAL	E	

southern red oak	<i>Quercus</i>	<i>falcata</i>	QUFA	E
cherrybark oak	<i>Quercus</i>	<i>pagoda</i>	QUPA5	E

---

## References

- Abatzoglou, J. T. (2013). Development of gridded surface meteorological data for ecological applications and modelling. *International Journal of Climatology*, 33, 121–131. <http://doi.org/10.1002/joc.3413>
- Abatzoglou, J. T., & Brown, T. J. (2012). A comparison of statistical downscaling methods suited for wildfire applications. *International Journal of Climatology*, 32, 772–780. <http://doi.org/10.1002/joc.2312>
- Abramowitz, M., & Stegun, I. A. (1964). *Handbook of mathematical functions*. New York: Dover.
- Adams, H. D., Luce, C. H., Breshears, D. D., Allen, C. D., Weiler, M., Hale, V. C., ... Huxman, T. E. (2012). Ecohydrological consequences of drought- and infestation-triggered tree die-off: insights and hypotheses. *Ecohydrology*, 5, 145–159. <http://doi.org/10.1002/eco>
- Adams, H. D., Williams, A. P., Xu, C., Rauscher, S. A., Jiang, X., & McDowell, N. G. (2013). Empirical and process-based approaches to climate-induced forest mortality models. *Frontiers in Plant Science*, 4, 1–5. <http://doi.org/10.3389/fpls.2013.00438>
- Adams, H. D., Zeppel, M. J. B., Anderegg, W. R. L., Hartmann, H., Landhäusser, S. M., Tissue, D. T., ... McDowell, N. G. (2017). A multi-species synthesis of physiological mechanisms in drought-induced tree mortality. *Nature Ecology & Evolution*, 1, 1285–1291. <http://doi.org/10.1038/s41559-017-0248-x>
- Adams, H. R., Barnard, H. R., & Loomis, A. K. (2014). Topography alters tree growth – climate relationships in a semi-arid forested catchment. *Ecosphere*, 5(11), 1–16.
- AghaKouchak, A., Cheng, L., Mazdidasni, O., & Farahmand, A. (2014). Global warming and changes in risk of concurrent climate extremes: Insights from the 2014 California drought. *Geophysical Research Letters*, 41, 8847–8852. <http://doi.org/10.1002/2014GL062308>
- Allen, C. D., & Breshears, D. D. (1998). Drought-induced shift of a forest–woodland ecotone: rapid landscape response to climatic variation. *Proceedings of the National Academy of Sciences*, 95, 14839–14842.
- Allen, C. D., Breshears, D. D., & McDowell, N. G. (2015). On underestimation of global vulnerability to tree mortality and forest die-off from hotter drought in the

- Anthropocene. *Ecosphere*, 6(8), 1–55.
- Allen, C. D., Macalady, A. K., Chenchouni, H., Bachelet, D., McDowell, N., Vennetier, M., ... Cobb, N. (2010). A global overview of drought and heat-induced tree mortality reveals emerging climate change risks for forests. *Forest Ecology and Management*, 259(4), 660–684. <http://doi.org/10.1016/j.foreco.2009.09.001>
- Allen, R. G., Pereira, L. S., Raes, D., & Smith, M. (1998). *Crop evapotranspiration: guidelines for computing crop water requirements - FAO Irrigation and drainage paper 56*. Rome, Italy: Food and Agriculture Organization of the United Nations. Retrieved from <http://www.fao.org/docrep/x0490e/x0490e00.htm#Contents>
- Anderegg, W. R. L., Flint, A., Huang, C., Flint, L., Berry, J. A., Davis, F. W., ... Field, C. B. (2015). Tree mortality predicted from drought-induced vascular damage. *Nature Geoscience*, 8, 367–371. <http://doi.org/10.1038/NGEO2400>
- Anderson, D. B. (1936). Relative humidity or vapor pressure deficit. *Ecology*, 17, 277–282.
- Andruk, C. M., Schwope, C., & Fowler, N. L. (2014). The joint effects of fire and herbivory on hardwood regeneration in central Texas woodlands. *Forest Ecology and Management*, 334, 193–200. <http://doi.org/10.1016/j.foreco.2014.08.037>
- Bachelet, D., Neilson, R. P., Lenihan, J. M., & Drapek, R. J. (2001). Climate Change Effects on Vegetation Distribution and Carbon Budget in the United States. *Ecosystems*, 4(3), 164–185. <http://doi.org/10.1007/s10021>
- Bahn, M., Reichstein, M., Dukes, J. S., Smith, M. D., & McDowell, N. G. (2014). Climate-biosphere interactions in a more extreme world. *New Phytologist*, 202(2), 356–359. <http://doi.org/10.1111/nph.12662>
- Baig, M. H. A., Zhang, L., Shuai, T., & Tong, Q. (2014). Derivation of a tasseled cap transformation based on Landsat 8 at-satellite reflectance. *Remote Sensing Letters*, 5(5), 423–431. <http://doi.org/10.1080/2150704X.2014.915434>
- Barger, N. N., Archer, S. R., Campbell, J. L., Huang, C. Y., Morton, J. A., & Knapp, A. K. (2011). Woody plant proliferation in North American drylands: A synthesis of impacts on ecosystem carbon balance. *Journal of Geophysical Research*, 116(3), 1–17. <http://doi.org/10.1029/2010JG001506>
- Bassett, E. N., & Fenn, P. (1984). Latent colonization and pathogenicity of *Hypoxyylon atropunctatum* on oaks. *Plant Disease*, 68, 317–319.

- Beven, K. (1995). Linking parameters across scales: subgrid parameterizations and scale dependent hydrological models. *Hydrological Processes*, 9, 507–525.
- Beven, K. (1997). TOPMODEL: A critique. *Hydrol. Process*, 11, 1069–1085.
- Beven, K. J., & Kirkby, M. J. (1979). A physically based, variable contributing area model of basin hydrology. *Hydrological Sciences*, 24(1), 43–69.  
<http://doi.org/10.1080/02626667909491834>
- Bigler, C., Gavin, D. G., Gunning, C., & Veblen, T. T. (2007). Drought induces lagged tree mortality in a subalpine forest in the Rocky Mountains. *Oikos*, 116(12), 1983–1994.  
<http://doi.org/10.1111/j.2007.0030-1299.16034.x>
- Bond, W. J., & Midgley, J. J. (2001). Ecology of sprouting in woody plants: the persistence niche. *Trends in Ecology and Evolution*, 16(1), 45–51.
- Bowker, M. A., Muñoz, A., Martinez, T., & Lau, M. K. (2012). Rare drought-induced mortality of juniper is enhanced by edaphic stressors and influenced by stand density. *Journal of Arid Environments*, 76(1), 9–16.  
<http://doi.org/10.1016/j.jaridenv.2011.08.012>
- Bréda, N., Huc, R., Granier, A., & Dreyer, E. (2006). Temperate forest trees and stands under severe drought : a review of ecophysiological responses , adaptation processes and long-term consequences. *Annals of Forest Science*, 63, 625–644.  
<http://doi.org/10.1051/forest>
- Breiman, L. (2001). Random Forests. *Machine Learning*, 45(1), 5–32.  
<http://doi.org/10.1023/A:1010933404324>
- Breshears, D. D., Adams, H. D., Eamus, D., McDowell, N. G., Law, D. J., Will, R. E., ... Zou, C. B. (2013). The critical amplifying role of increasing atmospheric moisture demand on tree mortality and associated regional die-off. *Frontiers in Plant Science*, 4, 1–4. <http://doi.org/10.3389/fpls.2013.00266>
- Breshears, D. D., Cobb, N. S., Rich, P. M., Price, K. P., Allen, C. D., Balice, R. G., ... Meyer, C. W. (2005). Regional vegetation die-off in response to global-change-type drought. *Proceedings of the National Academy of Sciences of the United States of America*, 102(42), 15144–15148. <http://doi.org/10.1073/pnas.0505734102>
- Burke, E. J., Brown, S. J., & Christidis, N. (2006). Modeling the recent evolution of global drought and projections for the twenty-first century with the hadley centre climate model. *Journal of Hydrometeorology*, 7, 1113–1125.

- Carnicer, J., Coll, M., Ninyerola, M., Pons, X., Sánchez, G., & Peñuelas, J. (2011). Widespread crown condition decline, food web disruption, and amplified tree mortality with increased climate change-type drought. *Proceedings of the National Academy of Sciences of the United States of America*, *108*(4), 1474–1478. <http://doi.org/10.1073/pnas.1010070108>
- Ciais, P., Reichstein, M., Viovy, N., Granier, A., Ogée, J., Allard, V., ... Valentini, R. (2005). Europe-wide reduction in primary productivity caused by the heat and drought in 2003. *Nature*, *437*(7058), 529–533. <http://doi.org/10.1038/nature03972>
- Clapp, R. B., & Hornberger, G. M. (1978). Empirical equations for some soil hydraulic properties. *Water Resources Research*, *14*(4), 601–604.
- Clark, J. S., Bell, D. M., Kwit, M. C., & Zhu, K. (2014). Competition-interaction landscapes for the joint response of forests to climate change. *Global Change Biology*, *20*(6), 1979–1991. <http://doi.org/10.1111/gcb.12425>
- Clark, J. S., Gelfand, A. E., Woodall, C. W., & Zhu, K. (2014). More than the sum of the parts: Forest climate response from joint species distribution models. *Ecological Applications*, *24*(5), 990–999. <http://doi.org/10.1890/13-1015.1>
- Clark, J. S., Iverson, L., Woodall, C. W., Allen, C. D., Bell, D. M., Bragg, D. C., ... Zimmermann, N. E. (2016). The impacts of increasing drought on forest dynamics, structure, and biodiversity in the United States. *Global Change Biology*, *22*(7), 2329–2352. <http://doi.org/10.1111/gcb.13160>
- Clark, J. S., Nemergut, D., Seyednasrollah, B., Turner, P. J., & Zhang, S. (2017). Generalized joint attribute modeling for biodiversity analysis: Median-zero, multivariate, multifarious data. *Ecological Monographs*, *87*, 34–56.
- Clifford, M. J., Royer, P. D., Cobb, N. S., Breshears, D. D., & Ford, P. L. (2013). Precipitation thresholds and drought-induced tree die-off: insights from patterns of *Pinus edulis* mortality along an environmental stress gradient. *New Phytologist*, *200*, 413–421. <http://doi.org/10.1111/nph.12362>
- Cohen, W. B., Fiorella, M., Gray, J., Helmer, E., & Anderson, K. (1998). An Efficient and Accurate Method for Mapping Forest Clearcuts in the Pacific Northwest Using Landsat Imagery, *64*(4), 293–300.
- Cohen, W. B., & Goward, S. N. (2004). Landsat's Role in Ecological Applications of Remote Sensing. *BioScience*, *54*(6), 535–545. [http://doi.org/10.1641/0006-3568\(2004\)054\[0535:LRIEAO\]2.0.CO;2](http://doi.org/10.1641/0006-3568(2004)054[0535:LRIEAO]2.0.CO;2)

- Collins, B. M., Miller, J. D., Thode, A. E., Kelly, M., van Wagtenonk, J. W., & Stephens, S. L. (2009). Interactions Among Wildland Fires in a Long-Established Sierra Nevada Natural Fire Area. *Ecosystems*, 12(1), 114–128. <http://doi.org/10.1007/s10021-008-9211-7>
- Comer, P. J., Faber-Langendoen, D., Evans, R., Gawler, S., Josse, C., Kittel, G., ... Teague, J. (2003). *Ecological Systems of the United States: A working classification of U.S. terrestrial systems*. Arlington, VA, USA.
- Coops, N. C., Johnson, M., Wulder, M. A., & White, J. C. (2006). Assessment of QuickBird high spatial resolution imagery to detect red attack damage due to mountain pine beetle infestation. *Remote Sensing of Environment*, 103(1), 67–80. <http://doi.org/10.1016/j.rse.2006.03.012>
- Crist, E. P. (1985). A TM Tasseled Cap equivalent transformation for reflectance factor data. *Remote Sensing of Environment*, 17, 301–306. [http://doi.org/10.1016/0034-4257\(85\)90102-6](http://doi.org/10.1016/0034-4257(85)90102-6)
- Crouchet, S. E. (2016). *Site factors influencing tree mortality during drought in Texas*. Texas State University.
- Daly, C., Smith, J. I., & Olson, K. V. (2015). Mapping atmospheric moisture climatologies across the conterminous United States. *PLoS ONE*, 10(10), 1–33. <http://doi.org/10.1371/journal.pone.0141140>
- Daly, E., Oishi, A. C., Porporato, A., & Katul, G. G. (2008). A stochastic model for daily subsurface CO<sub>2</sub> concentration and related soil respiration. *Advances in Water Resources*, 31(7), 987–994. <http://doi.org/10.1016/j.advwatres.2008.04.001>
- Daly, E., Porporato, A., & Rodriguez-Iturbe, I. (2004). Coupled dynamics of photosynthesis, transpiration, and soil water balance. part I: upscaling from hourly to daily level. *Journal of Hydrometeorology*, 5(3), 546–558. [http://doi.org/10.1175/1525-7541\(2004\)005<0546:CDOPTA>2.0.CO;2](http://doi.org/10.1175/1525-7541(2004)005<0546:CDOPTA>2.0.CO;2)
- De'ath, G., & Fabricius, K. E. (2000). Classification and regression trees: a powerful yet simple technique for ecological data analysis. *Ecology*, 81(11), 3178–3192.
- Domec, J. C., Smith, D. D., & McCulloh, K. A. (2017). A synthesis of the effects of atmospheric carbon dioxide enrichment on plant hydraulics: implications for whole-plant water use efficiency and resistance to drought. *Plant Cell and Environment*, 40, 921–937. <http://doi.org/10.1111/pce.12843>

- Duan, H., O'Grady, A. P., Duursma, R. A., Choat, B., Huang, G., Smith, R. A., ... Tissue, D. T. (2015). Drought responses of two gymnosperm species with contrasting stomatal regulation strategies under elevated [CO<sub>2</sub>] and temperature. *Tree Physiology*, 35, 756–770. <http://doi.org/10.1093/treephys/tpv047>
- Dunne, T., Moore, T. R., & Taylor, C. H. (1975). Recognition and prediction of runoff-producing zones in humid regions. *Hydrological Sciences*, 3, 305–326.
- Eamus, D., Boulain, N., Cleverly, J., & Breshears, D. D. (2013). Global change-type drought-induced tree mortality: vapor pressure deficit is more important than temperature per se in causing decline in tree health. *Ecology and Evolution*, 3(8), 2711–2729. <http://doi.org/10.1002/ece3.664>
- Elkington, R. J., Rebel, K. T., Heilman, J. L., Litvak, M. E., Dekker, S. C., & Moore, G. W. (2014). Species-specific water use by woody plants on the Edwards Plateau, Texas. *Ecohydrology*, 7(2), 278–290. <http://doi.org/10.1002/eco.1344>
- Elliott, L. F., Diamond, D. D., True, C. D., Blodgett, C. F., Pursell, D., German, D., & Treuer-Kuehn, A. (2014). Ecological Mapping Systems of Texas: Summary Report. Austin: Texas Parks & Wildlife Department. Available at: <http://tpwd.texas.gov/gis/gallery/> [February 2014].
- Engelbrecht, B. M. J., Comita, L. S., Condit, R., Kursar, T. A., Tyree, M. T., Turner, B. L., & Hubbell, S. P. (2007). Drought sensitivity shapes species distribution patterns in tropical forests. *Nature*, 447(7140), 80–82. <http://doi.org/10.1038/nature05747>
- Evans, J. S., Oakleaf, J., Cushman, S. A., & Theobald, D. (2014). An ArcGIS Toolbox for Surface Gradient and Geomorphometric Modeling, version 2.0-0. Retrieved from <http://evansmurphy.wix.com/evansspatial>
- Fehmi, J. S. (2010). Confusion among three common plant cover definitions may result in data unsuited for comparison. *Journal of Vegetation Science*, 21(2), 273–279.
- Fellows, A. W., & Goulden, M. L. (2013). Controls on gross production by a semiarid forest growing near its warm and dry ecotonal limit. *Agricultural and Forest Meteorology*, 169, 51–60. <http://doi.org/10.1016/j.agrformet.2012.10.001>
- Feng, X., Dawson, T. E., Ackerly, D. D., Santiago, L. S., & Thompson, S. E. (2017). Reconciling seasonal hydraulic risk and plant water use through probabilistic soil–plant dynamics. *Global Change Biology*. <http://doi.org/10.1111/gcb.13640>
- Fensham, R. J., Fairfax, R. J., & Ward, D. P. (2009). Drought-induced tree death in

- savanna. *Global Change Biology*, 15(2), 380–387. <http://doi.org/10.1111/j.1365-2486.2008.01718.x>
- Fisher, R., McDowell, N., Purves, D., Moorcroft, P., Sitch, S., Cox, P., ... Ian Woodward, F. (2010). Assessing uncertainties in a second-generation dynamic vegetation model caused by ecological scale limitations. *New Phytologist*, 187(3), 666–681. <http://doi.org/10.1111/j.1469-8137.2010.03340.x>
- Floyd, M. L., Clifford, M., Cobb, N. S., Hanna, D., Delph, R., Ford, P., & Turner, D. (2009). Relationship of stand characteristics to drought-induced mortality in three Southwestern pinon–juniper woodlands. *Ecological Applications*, 19(5), 1223–1230. <http://doi.org/10.1890/08-1265.1>
- Franks, P. J., Adams, M. A., Amthor, J. S., Barbour, M. M., Berry, J. A., Ellsworth, D. S., ... Caemmerer, S. von. (2013). Sensitivity of plants to changing atmospheric CO<sub>2</sub> concentration: from the geological past to the next century. *New Phytologist*, 197, 1077–1094.
- Galiano, L., Martínez-Vilalta, J., & Lloret, F. (2011). Carbon reserves and canopy defoliation determine the recovery of Scots pine 4 yr after a drought episode. *New Phytologist*, 190(3), 750–759. <http://doi.org/10.1111/j.1469-8137.2010.03628.x>
- Gislason, P. O., Benediktsson, J. A., & Sveinsson, J. R. (2006). Random Forests for land cover classification. *Pattern Recognition Letters*, 27(4), 294–300. <http://doi.org/10.1016/j.patrec.2005.08.011>
- Gitelson, A. A., Kaufman, Y. J., & Merzlyak, M. N. (1996). Use of a green channel in remote sensing of global vegetation from EOS-MODIS. *Remote Sensing of Environment*, 58(3), 289–298. [http://doi.org/10.1016/S0034-4257\(96\)00072-7](http://doi.org/10.1016/S0034-4257(96)00072-7)
- Gitlin, A. R., Sthultz, C. M., Bowker, M. A., Stumpf, S., Paxton, K. L., Kennedy, K., ... Whitham, T. G. (2006). Mortality gradients within and among dominant plant populations as barometers of ecosystem change during extreme drought. *Conservation Biology*, 20(5), 1477–1486. <http://doi.org/10.1111/j.1523-1739.2006.00424.x>
- González-Roglich, M., & Swenson, J. J. (2016). Tree cover and carbon mapping of Argentine savannas: scaling from field to region. *Remote Sensing of Environment*, 172, 139–147. <http://doi.org/10.1016/j.rse.2015.11.021>
- Guardiola-Claramonte, M., Troch, P. A., Breshears, D. D., Huxman, T. E., Switanek, M. B., Durcik, M., & Cobb, N. S. (2011). Decreased streamflow in semi-arid basins

- following drought-induced tree die-off: a counter-intuitive and indirect climate impact on hydrology. *Journal of Hydrology*, 406(3), 225–233.  
<http://doi.org/10.1016/j.jhydrol.2011.06.017>
- Hacke, U. G., Stiller, V., Sperry, J. S., Pittermann, J., & McCulloh, K. A. (2001). Cavitation fatigue. Embolism and refilling cycles can weaken the cavitation resistance of xylem. *Plant Physiology*, 125(2), 779–86. <http://doi.org/10.1104/PP.125.2.779>
- Hawthorne, S., & Miniati, C. F. (2017). Topography may mitigate drought effects on vegetation along a hillslope gradient. *Ecohydrology*. <http://doi.org/10.1002/eco.1825>
- Heilman, J. L., Litvak, M. E., McInnes, K. J., Kjelgaard, J. F., Kamps, R. H., & Schwinning, S. (2014). Water-storage capacity controls energy partitioning and water use in karst ecosystems on the Edwards Plateau, Texas. *Ecohydrology*, 7(1), 127–138.  
<http://doi.org/10.1002/eco.1327>
- Hewitt, N., & Kellman, M. (2004). Factors influencing tree colonization in fragmented forests: an experimental study of introduced seeds and seedlings. *Forest Ecology and Management*, 191, 39–59. <http://doi.org/10.1016/j.foreco.2003.11.003>
- Hoerling, M., Kumar, A., Dole, R., Nielsen-Gammon, J. W., Eischeid, J., Perlwitz, J., ... Chen, M. (2013). Anatomy of an extreme event. *Journal of Climate*, 26(9), 2811–2832.  
<http://doi.org/10.1175/JCLI-D-12-00270.1>
- Homer, C. G., Dewitz, J. A., Yang, L., Jin, S., Danielson, P., Xian, G., ... Megown, K. (2015). Completion of the 2011 National Land Cover Database for the conterminous United States-Representing a decade of land cover change information. *Photogrammetric Engineering and Remote Sensing*, 81(5), 345–354.
- Huang, C. Y., & Anderegg, W. R. L. (2012). Large drought-induced aboveground live biomass losses in southern Rocky Mountain aspen forests. *Global Change Biology*, 18(3), 1016–1027. <http://doi.org/10.1111/j.1365-2486.2011.02592.x>
- Hudson, B. (1994). Soil organic matter and available water capacity. *Journal of Soil and Water Conservation*, 49(2), 189–194.
- Huete, A. R. (1988). A soil-adjusted vegetation index (SAVI). *Remote Sensing of Environment*, 25(3), 295–309. [http://doi.org/10.1016/0034-4257\(88\)90106-X](http://doi.org/10.1016/0034-4257(88)90106-X)
- Hylander, K., Ehrlén, J., Luoto, M., & Meineri, E. (2015). Microrefugia: Not for everyone. *Ambio*, 44, 60–68. <http://doi.org/10.1007/s13280-014-0599-3>

- Ivits, E., Horion, S., Fensholt, R., & Cherlet, M. (2014). Drought footprint on European ecosystems between 1999 and 2010 assessed by remotely sensed vegetation phenology and productivity. *Global Change Biology*, 20(2), 581–593. <http://doi.org/10.1111/gcb.12393>
- Jackson, R. B., Moore, L. A., Hoffmann, W. A., Pockman, W. T., & Linder, C. R. (1999). Ecosystem rooting depth determined with caves and DNA. *Proceedings of the National Academy of Sciences of the United States of America*, 96(20), 11387–11392. <http://doi.org/10.1073/pnas.96.20.11387>
- Jackson, R. B., Randerson, J. T., Canadell, J. G., Anderson, R. G., Avissar, R., Baldocchi, D. D., ... Pataki, D. E. (2008). Protecting climate with forests. *Environmental Research Letters*, 3(4), 44006. <http://doi.org/10.1088/1748-9326/3/4/044006>
- Jentsch, A., Kreyling, J., & Beierkuhnlein, C. (2007). A new generation of climate-change experiments: events, not trends. *Frontiers in Ecology and the Environment*, 5(7), 365–374.
- Johnson, D. M., Domec, J.-C., Berry, Z. C., Schwantes, A. M., Woodruff, D. R., McCulloh, K. A., ... Jackson, R. B. (n.d.). Co-occurring woody species have diverse hydraulic strategies and mortality rates during an extreme drought. *In Review*.
- Johnson, D. M., Wortemann, R., McCulloh, K. A., Jordan-Meille, L., Ward, E., Warren, J. M., ... Domec, J.-C. (2016). A test of the hydraulic vulnerability segmentation hypothesis in angiosperm and conifer tree species. *Tree Physiology*, 36(8), 983–993. <http://doi.org/10.1093/treephys/tpw031>
- Jump, A. S., Mátyás, C., & Peñuelas, J. (2009). The altitude-for-latitude disparity in the range retractions of woody species. *Trends in Ecology and Evolution*, 24(12), 694–701. <http://doi.org/10.1016/j.tree.2009.06.007>
- Kaiser, K. E., McGlynn, B. L., & Emanuel, R. E. (2013). Ecohydrology of an outbreak: mountain pine beetle impacts trees in drier landscape positions first. *Ecohydrology*, 6, 444–454. <http://doi.org/10.1002/eco.1286>
- Kaufeld, K. A., Heaton, M. J., & Sain, S. R. (2014). A Spatio-Temporal Model for Mountain Pine Beetle Damage. *Journal of Agricultural, Biological, and Environmental Statistics*, 19(4), 439–452. <http://doi.org/10.1007/s13253-014-0182-1>
- Kennedy, R. E., Yang, Z., & Cohen, W. B. (2010). Detecting trends in forest disturbance and recovery using yearly Landsat time series: 1. LandTrendr - Temporal segmentation algorithms. *Remote Sensing of Environment*, 114(12), 2897–2910.

<http://doi.org/10.1016/j.rse.2010.07.008>

- Kieschnick, R., & McCullough, B. D. (2003). Regression analysis of variates observed on (0, 1): percentages, proportions and fractions. *Statistical Modelling*, 3(3), 193–213. <http://doi.org/http://doi.org/10.1191/1471082X03st053oa>
- Kiniry, J. R. (1998). Biomass accumulation and radiation use efficiency of honey mesquite and eastern red cedar. *Biomass and Bioenergy*, 15(6), 467–473. [http://doi.org/10.1016/S0961-9534\(98\)00057-9](http://doi.org/10.1016/S0961-9534(98)00057-9)
- Korzukhin, M. D., Ter-Mikaelian, M. T., & Wagner, R. G. (1996). Process versus empirical models: which approach for forest ecosystems management? *Canadian Journal of Forest Research*, 26, 879–887.
- Laio, F., Porporato, A., Ridolfi, L., & Rodriguez-iturbe, I. (2001). Plants in water-controlled ecosystems: active role in hydrologic processes and response to water stress II. Probabilistic soil moisture dynamics. *Advances in Water Resources*, 24, 707–723.
- Lazarus, E. D., & McGill, B. J. (2014). Pushing the Pace of Tree Species Migration. *PLoS ONE*, 9(8), e105380. <http://doi.org/10.1371/journal.pone.0105380>
- Liaw, A., & Wiener, M. (2002). Classification and regression by randomForest. *R News*, 2(3), 18–22.
- Lloret, F., Escudero, A., Iriondo, J. M., Martínez-Vilalta, J., & Valladares, F. (2012). Extreme climatic events and vegetation: The role of stabilizing processes. *Global Change Biology*, 18(3), 797–805. <http://doi.org/10.1111/j.1365-2486.2011.02624.x>
- Loehle, C., & LeBlanc, D. (1996). Model-based assessments of climate change effects on forests: a critical review. *Ecological Modelling*, 90, 1–31.
- Mackay, D. S., Roberts, D. E., Ewers, B. E., Sperry, J. S., McDowell, N. G., & Pockman, W. T. (2015). Interdependence of chronic hydraulic dysfunction and canopy processes can improve integrated models of tree response to drought. *Water Resources Research*, 51, 6156–6176. <http://doi.org/10.1002/2015WR017244>. Received
- Masek, J. G., Vermote, E. F., Saleous, N. E., Wolfe, R., Hall, F. G., Huemmrich, K. F., ... Lim, T.-K. (2006). A Landsat Surface Reflectance Dataset for North America, 1990–2000. *IEEE Geoscience and Remote Sensing Letters*, 3(1), 68–72. <http://doi.org/10.1109/LGRS.2005.857030>

- Mathys, A. S., Coops, N. C., & Waring, R. H. (2016). An ecoregion assessment of projected tree species vulnerabilities in western North America through the 21<sup>st</sup> century. *Global Change Biology*, 1–13. <http://doi.org/10.1111/gcb.13440>
- McCune, B., & Keon, D. (2002). Equations for potential annual direct incident radiation and heat load. *Journal of Vegetation Science*, 13(4), 603–606. <http://doi.org/10.1111/j.1654-1103.2002.tb02087.x>
- McDowell, N. G., Beerling, D. J., Breshears, D. D., Fisher, R. A., Raffa, K. F., & Stitt, M. (2011). The interdependence of mechanisms underlying climate-driven vegetation mortality. *Trends in Ecology and Evolution*, 26(10), 523–532. <http://doi.org/10.1016/j.tree.2011.06.003>
- McDowell, N. G., Coops, N. C., Beck, P. S. A., Chambers, J. Q., Gangodagamage, C., Hicke, J. a., ... Allen, C. D. (2015). Global satellite monitoring of climate-induced vegetation disturbances. *Trends in Plant Science*, 20(2), 114–123. <http://doi.org/10.1016/j.tplants.2014.10.008>
- McDowell, N. G., Fisher, R. A., Xu, C., Domec, J. C., Hölttä, T., Mackay, D. S., ... Pockman, W. T. (2013). Evaluating theories of drought-induced vegetation mortality using a multimodel-experiment framework. *New Phytologist*, 200(2), 304–321. <http://doi.org/10.1111/nph.12465>
- McDowell, N. G., Williams, A. P., Xu, C., Pockman, W. T., Dickman, L. T., Sevanto, S., ... Koven, C. (2016). Multi-scale predictions of massive conifer mortality due to chronic temperature rise. *Nature Climate Change*, 6, 295–300. <http://doi.org/10.1038/nclimate2873>
- McLaughlin, B. C., Ackerly, D. D., Klos, P. Z., Natali, J., Dawson, T. E., & Thompson, S. E. (2017). Hydrologic refugia, plants, and climate change. *Global Change Biology*, 23, 2941–2961. <http://doi.org/10.1111/gcb.13629>
- Meddens, A. J. H., & Hicke, J. A. (2014). Spatial and temporal patterns of Landsat-based detection of tree mortality caused by a mountain pine beetle outbreak in Colorado, USA. *Forest Ecology and Management*, 322, 78–88. <http://doi.org/10.1016/j.foreco.2014.02.037>
- Meddens, A. J. H., Hicke, J. A., Vierling, L. A., & Hudak, A. T. (2013). Evaluating methods to detect bark beetle-caused tree mortality using single-date and multi-date Landsat imagery. *Remote Sensing of Environment*, 132, 49–58. <http://doi.org/10.1016/j.rse.2013.01.002>

- Meigs, G. W., Kennedy, R. E., & Cohen, W. B. (2011). A Landsat time series approach to characterize bark beetle and defoliator impacts on tree mortality and surface fuels in conifer forests. *Remote Sensing of Environment*, 115(12), 3707–3718.  
<http://doi.org/10.1016/j.rse.2011.09.009>
- Meinzer, F. C., & McCulloh, K. A. (2013). Xylem recovery from drought-induced embolism: where is the hydraulic point of no return? *Tree Physiology*, 33(4), 331–334.  
<http://doi.org/10.1093/treephys/tpt022>
- Miao, S., Zou, C. B., & Breshears, D. D. (2009). Vegetation responses to extreme hydrological events: sequence matters. *The American Naturalist*, 173(1), 113–118.  
<http://doi.org/10.1086/593307>
- Michaelian, M., Hogg, E. H., Hall, R. J., & Arsenault, E. (2011). Massive mortality of aspen following severe drought along the southern edge of the Canadian boreal forest. *Global Change Biology*, 17(6), 2084–2094. <http://doi.org/10.1111/j.1365-2486.2010.02357.x>
- Mildrexler, D. J., Zhao, M., & Running, S. W. (2009). Testing a MODIS Global Disturbance Index across North America. *Remote Sensing of Environment*, 113(10), 2103–2117. <http://doi.org/10.1016/j.rse.2009.05.016>
- Mitchell, P. J., O’Grady, A. P., Hayes, K. R., & Pinkard, E. A. (2014). Exposure of trees to drought-induced die-off is defined by a common climatic threshold across different vegetation types. *Ecology and Evolution*, 4(7), 1088–1101.  
<http://doi.org/10.1002/ece3.1008>
- Moir, W. H. (1982). A Fire History of the High Chisos, Big Bend National Park, Texas. *Southwestern Association of Naturalists*, 27(1), 87–98.
- Moorcroft, P. R. (2006). How close are we to a predictive science of the biosphere? *Trends in Ecology and Evolution*, 21(7), 400–407. <http://doi.org/10.1016/j.tree.2006.04.009>
- Moore, G. W., Edgar, C. B., Vogel, J. G., Washington-Allen, R. A., March, R. G., & Zehnder, R. (2016). Tree mortality from an exceptional drought spanning mesic to -semiarid ecoregions. *Ecological Applications*, 26(2), 602–611.
- Moore, I. D., Burch, G. J., & Mackenzie, D. H. (1988). Topographic effects on the distribution of surface soil water and the location of ephemeral gullies. *Transactions of the ASAE*, 31(4), 1098–1107.
- Moore, I. D., Grayson, R. B., & Ladson, A. R. (1991). Digital Terrain Modeling: A Review

- of Hydrological Geomorphological and Biological Applications. *Hydrological Processes*, 5(1), 3–30. <http://doi.org/DOI: 10.1002/hyp.3360050103>
- Mueller, R. C., Scudder, C. M., Porter, M. E., Trotter, R. T., Gehring, C. A., & Whitham, T. G. (2005). Differential tree mortality in response to severe drought: evidence for long-term vegetation shifts. *Journal of Ecology*, 93(6), 1085–1093. <http://doi.org/10.1111/j.1365-2745.2005.01042.x>
- Niu, S., Luo, Y., Li, D., Cao, S., Xia, J., Li, J., & Smith, M. D. (2014). Plant growth and mortality under climatic extremes: An overview. *Environmental and Experimental Botany*, 98, 13–19. <http://doi.org/10.1016/j.envexpbot.2013.10.004>
- Norman, S. P., Koch, F. H., & Hargrove, W. W. (2016). Review of broad-scale drought monitoring of forests: Toward an integrated data mining approach. *Forest Ecology and Management*. <http://doi.org/10.1016/j.foreco.2016.06.027>
- Orsenigo, S., Mondoni, A., Rossi, G., & Abeli, T. (2014). Some like it hot and some like it cold, but not too much: Plant responses to climate extremes. *Plant Ecology*, 215(7), 677–688. <http://doi.org/10.1007/s11258-014-0363-6>
- Ospina, R., & Ferrari, S. L. P. (2010). Inflated beta distributions. *Statistical Papers*, 51(1), 111–126. <http://doi.org/10.1007/s00362-008-0125-4>
- Ospina, R., & Ferrari, S. L. P. (2012). A general class of zero-or-one inflated beta regression models. *Computational Statistics & Data Analysis*, 56(6), 1609–1623. <http://doi.org/10.1016/j.csda.2011.10.005>
- Owens, M. K. (1996). The Role of Leaf and Canopy-Level Gas Exchange in the Replacement of *Quercus virginiana* (Fagaceae) by *Juniperus ashei* (Cupressaceae) in Semiarid Savannas. *American Journal of Botany*, 83(5), 617–623.
- Owens, M. K., Lyons, R. K., & Alejandro, C. L. (2006). Rainfall partitioning within semiarid juniper communities: effects of event size and canopy cover. *Hydrological Processes*, 20, 3179–3189. <http://doi.org/10.1002/hyp>
- Parolari, A. J., Katul, G. G., & Porporato, A. (2014). An ecohydrological perspective on drought-induced forest mortality. *Journal of Geophysical Research: Biogeosciences*, 119(5), 965–981. <http://doi.org/10.1002/2013JG002592>
- Pellenq, J., Kalma, J., Boulet, G., Saulnier, G. M., Wooldridge, S., Kerr, Y., & Chehbouni, A. (2003). A disaggregation scheme for soil moisture based on topography and soil depth. *Journal of Hydrology*, 276(1–4), 112–127. <http://doi.org/10.1016/S0022->

1694(03)00066-0

- Peterman, W., & Waring, R. H. (2014). Does overshoot in leaf development of ponderosa pine in wet years leads to bark beetle outbreaks on fine-textured soils in drier years? *Forest Ecosystems*, 1:24.
- Phillips, O. L., Heijden, G. van der, Lewis, S. L., Lopez-Gonzalez, G., Aragao, L. E. O. C., Lloyd, J., ... Vilanova, E. (2010). Drought – mortality relationships for tropical forests. *New Phytologist*, 187, 631–646.
- Piramuthu, S. (2008). Input data for decision trees. *Expert Systems with Applications*, 34(2), 1220–1226. <http://doi.org/10.1016/j.eswa.2006.12.030>
- Pollock, L. J., Tingley, R., Morris, W. K., Golding, N., O'Hara, R. B., Parris, K. M., ... Mccarthy, M. A. (2014). Understanding co-occurrence by modelling species simultaneously with a Joint Species Distribution Model (JSDM). *Methods in Ecology and Evolution*, 5(5), 397–406. <http://doi.org/10.1111/2041-210X.12180>
- Porporato, A., Laio, F., Ridolfi, L., & Rodriguez-Iturbe, I. (2001). Plants in water-controlled ecosystems: active role in hydrologic processes and response to water stress: III. Vegetation water stress. *Advances in Water Resources*, 24(7), 725–744. [http://doi.org/10.1016/S0309-1708\(01\)00006-9](http://doi.org/10.1016/S0309-1708(01)00006-9)
- Poulos, H. M. (2014). Tree mortality from a short-duration freezing event and global-change-type drought in a Southwestern piñon-juniper woodland, USA. *PeerJ*, 2, 1–14. <http://doi.org/10.7717/peerj.404>
- PRISM Climate Group. (2015). Oregon State University. Retrieved from <http://prism.oregonstate.edu>
- Qi, J., Chehbouni, A., Huete, A. R., Kerr, Y. H., & Sorooshian, S. (1994). A modified soil adjusted vegetation index. *Remote Sensing of Environment*, 48(2), 119–126. [http://doi.org/10.1016/0034-4257\(94\)90134-1](http://doi.org/10.1016/0034-4257(94)90134-1)
- Quinn, P., Beven, K., & Culf, A. (1995). The introduction of macroscale hydrological complexity into land surface-atmosphere transfer models and the effect on planetary boundary layer development. *Journal of Hydrology*, 166, 421–444.
- R Core Team. (2015). R: A language and environment for statistical computing. R Foundation for Statistical Computing, Vienna, Austria. <http://www.r-project.org/>.
- Reyer, C. P. O., Brouwers, N., Rammig, A., Brook, B. W., Epila, J., Grant, R. F., ... Villela,

- D. M. (2015). Forest resilience and tipping points at different spatio-temporal scales: Approaches and challenges. *Journal of Ecology*, *103*(1), 5–15. <http://doi.org/10.1111/1365-2745.12337>
- Rigby, R. A., & Stasinopoulos, D. M. (2005). Generalized additive models for location, scale and shape. *Journal of the Royal Statistical Society: Series C (Applied Statistics)*, *54*(3), 507–554. <http://doi.org/10.1111/j.1467-9876.2005.00510.x>
- Rind, D., Goldberg, R., Hansen, J., Rosenzweig, C., & Ruedy, R. (1990). Potential evapotranspiration and the likelihood of future drought. *Journal of Geophysical Research*, *95*(D7), 9983–10004. <http://doi.org/10.1029/JD095iD07p09983>
- Rodriguez-iturbe, I., & Porporato, A. (2004). *Ecohydrology of water-controlled Ecosystems*. Cambridge, UK: Cambridge University Press.
- Rodriguez-Iturbe, I., Porporato, A., Ridolfi, L., Isham, V., & Cox, D. R. (1999). Probabilistic modelling of water balance at a point: the role of climate soil and vegetation. *Proceedings of the Royal Society of London Series A-Mathematical Physical and Engineering Sciences*, *455*, 3789–3805.
- Rogan, J., Franklin, J., & Roberts, D. A. (2002). A comparison of methods for monitoring multitemporal vegetation change using Thematic Mapper imagery. *Remote Sensing of Environment*, *80*(1), 143–156. [http://doi.org/10.1016/S0034-4257\(01\)00296-6](http://doi.org/10.1016/S0034-4257(01)00296-6)
- Rotenberg, E., & Yakir, D. (2010). Contribution of semi-arid forests to the climate system. *Science*, *327*, 451–454. <http://doi.org/10.1126/science.1179998>
- Rupp, D. E., Li, S., Massey, N., Sparrow, S. N., Mote, P. W., & Allen, M. (2015). Anthropogenic influence on the changing likelihood of an exceptionally warm summer in Texas, 2011. *Geophysical Research Letters*, *42*(7), 2392–2400. <http://doi.org/10.1002/2014GL062683>
- Savage, S. L., Lawrence, R. L., & Squires, J. R. (2015). Predicting relative species composition within mixed conifer forest pixels using zero-inflated models and Landsat imagery. *Remote Sensing of Environment*, *171*, 326–336. <http://doi.org/10.1016/j.rse.2015.10.013>
- Schwantes, A. M., Swenson, J. J., González-Roglich, M., Johnson, D. M., Domec, J.-C., & Jackson, R. B. (2017). Measuring canopy loss and climatic thresholds from an extreme drought along a fivefold precipitation gradient across Texas. *Global Change Biology*, 1–16. <http://doi.org/10.1111/gcb.13775>

- Schwantes, A. M., Swenson, J. J., & Jackson, R. B. (2016). Quantifying drought-induced tree mortality in the open canopy woodlands of central Texas. *Remote Sensing of Environment*, 181, 54–64. <http://doi.org/10.1016/j.rse.2016.03.027>
- Seager, R., Naik, N., & Vecchi, G. A. (2010). Thermodynamic and dynamic mechanisms for large-scale changes in the hydrological cycle in response to global warming. *Journal of Climate*, 23(17), 4651–4668. <http://doi.org/10.1175/2010JCLI3655.1>
- Sing, T., Sander, O., Beerenwinkel, N., & Lengauer, T. (2005). ROCr: visualizing classifier performance in R. *Bioinformatics*, 21(20), 3940–3941. <http://doi.org/10.1093/bioinformatics/bti623>
- Sperry, J. S., & Love, D. M. (2015). What plant hydraulics can tell us about responses to climate-change droughts. *New Phytologist*, 207, 14–27. <http://doi.org/10.1111/nph.13354>
- Tague, C. L., McDowell, N. G., & Allen, C. D. (2013). An integrated model of environmental effects on growth, carbohydrate balance, and mortality of *Pinus ponderosa* forests in the southern Rocky Mountains. *PLoS ONE*, 8(11), e80286. <http://doi.org/10.1371/journal.pone.0080286>
- Tai, X., Mackay, D. S., Anderegg, W. R. L., Sperry, J. S., & Brooks, P. D. (2017). Plant hydraulics improves and topography mediates prediction of aspen mortality in southwestern USA. *New Phytologist*, 213(1), 113–127. <http://doi.org/10.1111/nph.14098>
- Tarboton, D. G. (2005). Terrain analysis using digital elevation models (TauDEM). Utah State University.
- Therneau, T., Atkinson, B., & Ripley, B. (2015). rpart: recursive partitioning and regression trees. *R Package Version 4.1-9*. Retrieved from <http://cran.r-project.org/package=rpart>
- Thornton, P. E., Running, S. W., & White, M. A. (1997). Generating surfaces of daily meteorological variables over large regions of complex terrain. *Journal of Hydrology*, 190, 214–251. [http://doi.org/10.1016/S0022-1694\(96\)03128-9](http://doi.org/10.1016/S0022-1694(96)03128-9)
- Thornton, P. E., Thornton, M. M., Mayer, B. W., Wilhelmi, N., Wei, Y., Devarakonda, R., & Cook, R. B. (2014). DAYMET: Daily Surface Weather on a 1 km Grid for North America, Version 2. ORNL DAAC, Oak Ridge, Tennessee, USA. Available at: <http://daymet.ornl.gov/>. [June 2015]. <http://doi.org/http://dx.doi.org/10.3334/ORNLDAAC/1219>

- Trenberth, K. E., Dai, A., van der Schrier, G., Jones, P. D., Barichivich, J., Briffa, K. R., & Sheffield, J. (2014). Global warming and changes in drought. *Nature Clim. Change*, 4(1), 17–22. <http://doi.org/10.1038/NCLIMATE2067>
- Tucker, C. J. (1979). Red and photographic infrared linear combinations for monitoring vegetation. *Remote Sensing of Environment*, 8(2), 127–150. [http://doi.org/10.1016/0034-4257\(79\)90013-0](http://doi.org/10.1016/0034-4257(79)90013-0)
- Twidwell, D., Wonkka, C. L., Taylor, C. A., Zou, C. B., Twidwell, J. J., & Rogers, W. E. (2014). Drought-induced woody plant mortality in an encroached semi-arid savanna depends on topographic factors and land management. *Applied Vegetation Science*, 17(1), 42–52. <http://doi.org/10.1111/avsc.12044>
- United States Department of Agriculture. (2014). *Soil Survey Staff, Natural Resources Conservation Service. Soil Survey Geographic (SSURGO) Database*. Retrieved from <https://sdmdataaccess.sc.egov.usda.gov>.
- US Department of Agriculture. (2014). Geospatial data gateway. Available at: <http://datagateway.nrcs.usda.gov>. [March 2014].
- USDA Forest Service/U.S. Geological Survey. (2014). MTBS Data Access: Fire Level Geospatial Data. Available at: <http://mtbs.gov/dataquery/individualfiredata.html>. [Nov 2014].
- USDA NRCS. (2015). The PLANTS Database. National Plant Data Team, Greensboro, NC, USA. Available at: <http://plants.usda.gov>.
- van Langevelde, F., Van De Vijver, C. A. D. M., Kumar, L., van de Koppel, J., de Ridder, N., van Andel, J., ... Rietkerk, M. (2003). Effects of Fire and Herbivory on the Stability of Savanna Ecosystems. *Ecology*, 84(2), 337–350.
- van Mantgem, P. J., Stephenson, N. L., Byrne, J. C., Daniels, L. D., Franklin, J. F., Fulé, P. Z., ... Veblen, T. T. (2009). Widespread increase of tree mortality rates in the western United States. *Science*, 323(5913), 521–524. <http://doi.org/10.1126/science.1165000>
- van Wageningen, J. W., Root, R. R., & Key, C. H. (2004). Comparison of AVIRIS and Landsat ETM+ detection capabilities for burn severity. *Remote Sensing of Environment*, 92(3), 397–408. <http://doi.org/10.1016/j.rse.2003.12.015>
- Venkataraman, K., Tummuri, S., Medina, A., & Perry, J. (2016). 21st century drought outlook for major climate divisions of Texas based on CMIP5 multimodel ensemble:

- implications for water resource management. *Journal of Hydrology*, 534, 300–316. <http://doi.org/10.1016/j.jhydrol.2016.01.001>
- Vicente-Serrano, S. M., Camarero, J. J., Zabalza, J., Sangüesa-Barreda, G., López-Moreno, J. I., & Tague, C. L. (2015). Evapotranspiration deficit controls net primary production and growth of silver fir: Implications for Circum-Mediterranean forests under forecasted warmer and drier conditions. *Agricultural and Forest Meteorology*, 206, 45–54. <http://doi.org/10.1016/j.agrformet.2015.02.017>
- Vicente-Serrano, S. M., Lopez-Moreno, J.-I., Beguería, S., Lorenzo-Lacruz, J., Sanchez-Lorenzo, A., García-Ruiz, J. M., ... Espejo, F. (2014). Evidence of increasing drought severity caused by temperature rise in southern Europe. *Environmental Research Letters*, 9, 44001. <http://doi.org/10.1088/1748-9326/9/4/044001>
- Viola, F., Daly, E., Vico, G., Cannarozzo, M., & Porporato, A. (2008). Transient soil-moisture dynamics and climate change in Mediterranean ecosystems. *Water Resources Research*, 44, 1–12. <http://doi.org/10.1029/2007WR006371>
- Vogelmann, J. E., & Rock, B. N. (1988). Assessing forest damage in high-elevation coniferous forests in Vermont and New Hampshire using thematic mapper data. *Remote Sensing of Environment*, 24(2), 227–246. [http://doi.org/10.1016/0034-4257\(88\)90027-2](http://doi.org/10.1016/0034-4257(88)90027-2)
- Vogelmann, J. E., Tolk, B., & Zhu, Z. (2009). Monitoring forest changes in the southwestern United States using multitemporal Landsat data. *Remote Sensing of Environment*, 113(8), 1739–1748. <http://doi.org/10.1016/j.rse.2009.04.014>
- Walton, J. T. (2008). Subpixel Urban Land Cover Estimation: Comparing Cubist, Random Forests and Support Vector Regression. *Photogrammetric Engineering & Remote Sensing*, 74(10), 1213–1222.
- Wan, Z. (2008). New refinements and validation of the MODIS Land-Surface Temperature/Emissivity products. *Remote Sensing of Environment*, 112(1), 59–74. <http://doi.org/10.1016/j.rse.2006.06.026>
- Western, A. W., Grayson, R. B., Blöschl, G., & Willgoose, G. R. (1999). Observed spatial organization of soil moisture and its relation to terrain indices. *Water Resources Research*, 35(3), 797–810.
- Williams, A. P., Allen, C. D., Macalady, A. K., Griffin, D., Woodhouse, C. A., Meko, D. M., ... McDowell, N. G. (2013). Temperature as a potent driver of regional forest drought stress and tree mortality. *Nature Climate Change*, 3(3), 292–297.

<http://doi.org/10.1038/nclimate1693>

- Williams, A. P., Seager, R., Berkelhammer, M., Macalady, A. K., Crimmins, M. A., Swetnam, T. W., ... Rahn, T. (2014). Causes and implications of extreme atmospheric moisture demand during the record-breaking 2011 wildfire season in the southwestern United States. *American Meteorological Society*, *53*, 2671–2684. <http://doi.org/10.1175/JAMC-D-14-0053.1>
- Willson, C. J., Manos, P. S., & Jackson, R. B. (2008). Hydraulic traits are influenced by phylogenetic history in the drought-resistant, invasive genus *Juniperus* (Cupressaceae). *American Journal of Botany*, *95*(3), 299–314. <http://doi.org/10.3732/ajb.95.3.299>
- Wilson, A. D. (2001). Oak wilt: a potential threat to southern and western oak forests. *Journal of Forestry*, *99*(5), 4–11. Retrieved from <http://www.ingentaconnect.com/content/saf/jof/2001/00000099/00000005/art00003>
- Wilson, E. H., & Sader, S. A. (2002). Detection of forest harvest type using multiple dates of Landsat TM imagery. *Remote Sensing of Environment*, *80*(3), 385–396. [http://doi.org/10.1016/S0034-4257\(01\)00318-2](http://doi.org/10.1016/S0034-4257(01)00318-2)
- Wolock, D. M., & Price, C. V. (1994). Effects of digital elevation model map scale and data resolution on a topography-based watershed model. *Water Resources Research*, *30*(11), 3041–3052.
- Young, V. A. (1956). The effect of the 1949-1954 drought on the ranges of Texas. *Journal of Range Management*, *9*(3), 139–142.
- Zeppel, M. J. B., Harrison, S. P., Adams, H. D., Kelley, D. I., Li, G., Tissue, D. T., ... Mcdowell, N. G. (2015). Drought and resprouting plants. *New Phytologist*, *206*(2), 583–589. <http://doi.org/10.1111/nph.13205>
- Zhu, A. X., & Mackay, D. S. (2001). Effects of spatial detail of soil information on watershed modeling. *Journal of Hydrology*, *248*, 54–77.
- Zimmermann, N. E., Yoccoz, N. G., Edwards, T. C., Meier, E. S., Thuiller, W., Guisan, A., ... Pearman, P. B. (2009). Climatic extremes improve predictions of spatial patterns of tree species. *Proceedings of the National Academy of Sciences of the United States of America*, *106*, 19723–19728. <http://doi.org/10.1073/pnas.0901643106>

## Biography

Amanda M. Schwantes was born on November 13, 1986 in New York City, New York. She attended the University of Virginia, Charlottesville and received a BS in environmental science and a BA in chemistry in May 2009. She started her PhD at Duke University in Sept. 2012. She has published two first author journal articles including 'Quantifying drought-induced tree mortality in the open canopy woodlands of central Texas' (Schwantes et al, 2016), published in *Remote sensing of the Environment* and 'Measuring canopy loss and climatic thresholds from an extreme drought along a 5-fold precipitation gradient across Texas' (Schwantes et al, 2017), published in *Global Change Biology*. She was supported during her doctoral research from a James B. Duke Fellowship, a NASA Earth and Space Science Fellowship, a Duke Graduate School Fellowship, and Nicholas School of the Environment Conservation Fellowship. She is currently a member of the American Geophysical Union and the Ecological Society of America.